MICROFLUIDICS & AC ELECTROKINETICS: DEVELOPING BIOSENSORS FOR PORTABLE DIAGNOSTICS AND AUTOLOGOUS BLOOD DOPING IN ENDURANCE ATHLETES

by

Francesca Crivellari

A dissertation submitted to Johns Hopkins University in conformity with the requirements for the degree of Doctor of Philosophy

Department of Chemical and Biomolecular Engineering
Baltimore, Maryland

February 2018

Abstract

The intensely competitive nature of endurance sports drives athletes to great lengths in order to secure victory. When conditioning isn't enough, athletes use artificial means of enhancing aerobic performance, despite being banned by anti-doping entities. As athletes develop new methods of blood doping, there invariably follow methods to detect their use. However, autologous blood transfusions (ABT), the removal and subsequent reinfusion of one's own blood, remain the most difficult methods to detect. To mitigate its use, WADA introduced the Athlete Biological Passport (ABP). The ABP tracks an athlete's long-term blood profile through numerous biomarkers; abnormal variations may be signs of doping, but are not definitive indicators, which necessitates a direct diagnostic technique.

There is evidence that red blood cells (RBCs) undergo physiological changes in storage that are not mirrored in circulating RBCs. We explore methods to exploit storage-induced changes and develop a two-pronged assay to identify and separate reinfused RBCs from fresh cells. We probe the electrophoretic mobility of aging cells over 6 weeks using dielectrophoresis; this method yields visible separation of a 5% mixed blood population within seconds without labels or fluorescent tags. We investigate a microfluidic technique for high-throughput probing of RBC viscoelasticity. Using Real Time Deformability Cytometry (RTDC), we capture 10^2–10^3 cells in seconds of high speed imaging; analysis shows a clear decline in deformability. In simulated reinfusions, we see distinction between the fresh and the 5% reinfused population. As a direct detection method, this technique identifies blood doping in minutes with little sample preparation. As complementary parts of a single assay, DEP-RTDC tests can identify and isolate reinfused cells, increasing the efficacy of the ABP.

The need for sensitive detection is not limited to the world of elite athletic competitions, and is in growing demand in personalized medicine. We present a bead-based detection method, which provides a platform for numerous assays – whole blood tests and anti-doping assessments among them. By combining electrokinetics and microfluidics, we create a sensitive biosensor for detection at miscible, liquid-liquid interfaces. Arrays of microelectrodes embedded into microfluidic T-channels deliver AC electric fields directly into co-flowing laminar streams. Interfacial motion produced is a function of electrolyte properties and binding kinetics, and a metric for biomolecular detection. Integration of colloidal suspensions creates the capability of detecting biotin-streptavidin binding at concentrations of 500 attomolar biotin.

To my father, a true engineer.

And my mother, whom I promise to call.

Acknowledgements

I’d like to thank my advisor, Professor Zachary Gagnon, for his guidance and support through these years. A true mentor who taught me how to think, helped me find my passion in the lab, and gave me the freedom to follow it. His enthusiasm for the science and seemingly endless patience are resources I’ve relied on heavily during this time, and I consider myself lucky to have been under his tutelage.

Special thanks to Nick, my sounding board and friend in the trenches, without whom I might have been lost. Nick, Mitch, and Fu – I’ve learned so much from them, and they were always willing to lend me their time and their minds – I couldn’t have asked for better lab mates.

Thank you to Mike, David, Quinton, John, and Angelo, for letting me prick their fingers and take their blood for weeks on end, and for always showing up excited about the projects. Thanks, in particular to Mike, for all the unscheduled donations, and willingness to give more.

Thank you to Quinton, whose friendship and contributions have been and continue to be invaluable, both to the research and to me, personally.

Thank you to my family, who have hung in there and stuck by me during this adventure.

And to Jim, without whom the future would look much different.

Table of Contents

Abstract ii

Acknowledgements v

Table of Contents vi

List of Tables x

List of Figures xi

Executive Summary 1

Introduction 3

- 2.1 Dielectrophoresis 3
  - 2.1.1 Classical Dielectrophoresis 3
  - 2.1.2 Fluidic Dielectrophoresis 5
- 2.2 Bead-Based Biosensors 6
  - 2.2.1 Static-Substrate Biosensors 6
  - 2.2.2 Liquid-Liquid Interfacial Biosensors 7

Detailed Methods and Protocols 10

- 3.1 Photomasks 10
- 3.2 Microelectrodes 12
  - 3.2.1 Physical vapor deposition 13
  - 3.2.2 Photolithography 14
  - 3.2.3 Wet etching 15
  - 3.2.4 Lift-off technique 16
- 3.2 Microchannel fabrication 18
  - 3.2.1 Soft lithography 18
  - 3.2.2 Alignment and bonding devices 20
  - 3.2.3 Multi-layer designs 20
- 3.3 Blood sample preparation 22
  - 3.3.1 Blood sourcing, drawing, and storage 22
  - 3.3.2 Washing 24
  - 3.3.3 Glutaraldehyde fixation 25
- 3.4 Flow sources 26
  - 3.4.1 Syringe pump 27

3.4.2 Automated flow controller 27
3.4.3 Constant pressure manual flow controller 28
3.4.3.1 A low-cost microfluidic flow controller 28
3.4.3.2 Hydraulic circuit analysis 29
3.4.3.3 Regulating flow rate 32
3.4.3.4 Flow controller assembly and testing method 33
3.4.4 Supplementary materials 36
3.4.4.1 Hydraulic resistance measurements 36
3.4.4.2 Flow rate capabilities, stability and response time 37
3.4.4.3 Flow switches prevent fluid back flow 39
Dielectrophoretic detection of autologous blood doping 44
4.1 Introduction 44
4.2 Materials and Methods 47
4.2.1 Device Fabrication 47
4.2.2 Blood Sample Preparation 49
4.2.3 Dielectrophoretic Analysis 51
4.3. Results and Discussion 54
4.3.1 Characterization of the DEP Spectrum 55
4.3.2 Volunteer Samples 56
4.3.3 *In Vitro* Autologous Reinfusion 59
4.3.4 *In vivo* Autologous Transfusion 60
4.4 Conclusions 64
Real-time deformability cytometry (RTDC) for detection of autologous blood doping 66
5.1 Introduction 66
5.2 Materials and Methods 69
5.2.1 Device Fabrication 69
5.2.2 Blood Sample Preparation 70
5.2.3 Real-Time Deformability Cytometry 71
5.3 Results and Discussions 74
5.3.1 Buffer Optimization and Device Calibration 74
5.3.2 RBC Deformability with Increasing Storage Time 77
5.3.3 *In Vitro* Autologous Transfusion 81

5.4 Conclusions 82

Microfluidic bubbler facilitates near complete mass transfer for sustainable multiphase and microbial processing 84

6.1 Introduction 85

6.2 Methods 92

6.2.1 Microfluidic Fabrication 92

6.2.2 K_La determination 93

6.2.3 Fraction of Oxygen Transferred 94

6.2.4 Additional Bubbling Equipment 95

6.2.5 Gases and Liquids 96

6.2.6 Equipment 96

6.2.7 Algae Cultures 97

6.3 Results 97

6.3.1 Bubble Size 97

6.3.2 Volumetric Mass Transfer Coefficient (K_La) 101

6.3.3 Fraction Oxygen Transferred 102

6.3.4 Microbubbler in an Algae Culture 107

6.3.5 Estimate of Gas Feed Costs for Large Scale Algal Bioreactors 109

6.4 Discussion 110

6.5 Supplementary Materials and Figures 118

Label-free biomolecular detection at electrically displaced liquid interfaces using interfacial electrokinetic transduction (IET) 122

7.1 Introduction 123

7.2 Materials and methods 128

7.2.1 Microfluidic device fabrication 128

7.2.2 Sensor measurement 129

7.2.3 Protein solutions 131

7.2.4 The electrical interface 131

7.2.5 Measuring interfacial frequency response 132

7.2.6 Electrokinetics of an electrical interface-fluidic dielectrophoresis 135

7.2.7 Using interfacial crossover frequency to detect specific binding 138

7.3 Results and discussion 138

7.3.1 The IET biosensor sensorgram 138

7.3.2 Avidin–biotin binding influences interfacial conductivity 141

7.3.3 Selective and specific biosensing in a BSA background 144
7.3.4 Label-free femtomolar detection in BSA.. 147
7.4 Conclusions.. 149
Nanoparticle-based biosensing using interfacial electrokinetic transduction..... 151
8.1 Introduction.. 152
8.2. Material and Methods 156
8.2.1 Device Fabrication.. 156
8.2.2 Creating the Electrical Liquid Interface.. 158
8.2.3 Fluidic Dielectrophoresis.. 161
8.3 Results and Discussion 163
8.3.1 Maxwell-Wagner Polarization... 163
8.3.2 Biotin-Streptavidin Binding.. 165
8.3.3 Limit of Detection... 168
8.3.4 Background Protein 170
8.3.5 Human IgG-Protein A... 171
8.4 Conclusions.. 174
Conclusions... 177
References.. 179
Curriculum Vitae 193

List of Tables

Table 5.1. Average cell size and deformation from non-human mammalian sources.......... 76

Table 6.1 Performance of the microbubbler in an algae bioreactor.......... 109

Table 6.2 Economic analysis of microbubbler operation compared to other bubbling methods.......... 110

List of Figures

Figure 3.1. Low-cost microfluidic flow controller for controlling flows through four fluidic inlets. 29

Figure 3.2. Pressure versus flow rate for three channel lengths without a capillary tube. 38

Figure 3.3. Time response comparison of the presented flow controller and a commercial syringe pump. 39

Figure 3.4. Low-cost fluidic switch for fluid routing. 41

Figure 4.1. Micrographs of red blood cell DEP on a quadrupole electrode array. 53

Figure 4.2. Isolated DEP microfluidic testing chamber. 53

Figure 4.3. Effects of fixation and storage time on RBC crossover. 55

Figure 4.4. DEP of grad volunteer samples 57

Figure 4.5. Effects of exercise on athlete COF 58

Figure 4.6. Individual effects of exercise on athlete COF. 59

Figure 4.7. Visualization of a simulated reinfusion and fluorescent confirmation of detection. 60

Figure 4.8. Effects of autologous blood transfusion on COF 62

Figure 4.9. Complex breakdown of the effects of autologous blood transfusion on COF 63

Figure 4.10. Illustration of decreased COF in subject AT1 63

Figure 4.11. Illustration of decreased COF in subject AT3 64

Figure 5.1. Brightfield view of RTDC microfluidic device. 72

Figure 5.2. Optimization of the viscous cell medium 75

Figure 5.3. Deformability analysis of non-human mammalian RBCs. 77

Figure 5.4. Deformability analysis of human RBC over storage time. 78

Figure 5.5. Overall change in deformability of vendor-sourced human RBCs 80

Figure 5.6. Overall change in deformability of grad volunteer human RBCs 80

Figure 5.7. Deformability analysis of grad volunteer in vitro transfusion. 82

Figure 6.1 Design and size specifications of the Y-junction of the microfluidic device used to make micro-scale bubbles 90

Figure 6.2 Bubble images. 99

Figure 6.3 Bubble diameter distribution. 99

Figure 6.4 Bubble size dependence on flow rate for all devices 100
Figure 6.5 K_La of the microbubbler compared to other methods 102
Figure 6.6 Fraction of oxygen transferred dependence on flow rate. 104
Figure 6.7 Oxygen concentration in headspace. 106
Supplementary Figure S6.1 Microfluidic bubbler channel and mask design 118
Supplementary Figure S6.2 Dissolved oxygen concentration over time for the calculation of K_La 119
Supplementary Figure S6.3 Plot of the natural log of the saturation dissolved oxygen concentration minus the dissolved oxygen levels for the area of interest 119
Supplementary Figure S6.4 Histogram of bubble distributions for other sparging methods 120
Supplementary Figure S6.5 Bubble frequency dependence on height of liquid for a range of flow rates 121
Figure 7.1 Biosensing T-channel schematic. 125
Figure 7.2. Confocal displacement micrographs 130
Figure 7.3 Electrical and reaction influence on displacement and dimensionless frequency 134
Figure 7.4 Effects of biotin-avidin binding on interfacial displacement 142
Figure 7.5 IET sensorgram illustrating selective sensor response to both BSA/anti-BSA and avidin/biotin binding. 143
Figure 7.6 IET sensorgrams and binding curves 147
Figure 8.1. Microfluidic T-channel 158
Figure 8.2. fDEP crossover frequency 160
Figure 8.3. IET bead-based biosensing assay 167
Figure 8.4. Streptavidin limited detection by varying particle wt% 169
Figure 8.5. Biotin detection in BSA background 171
Figure 8.6. Detection of human IgG-Protein A binding 172
Figure 8.6. Influence of binding reaction on electrical properties measured by interface displacement 174

Chapter 1

Executive Summary

Microfluidics and AC electrokinetics are used in this work in an attempt to satisfy a number of biosensing needs – namely sensitive, inexpensive, portable diagnostics for personal health, and the detection of autologous blood doping in endurance athletes.

As athletes uncover and develop new methods of blood doping, there invariably follows a diagnostic method to detect its use. However, autologous blood transfusions (ABT), the removal and subsequent reinfusion of one's own blood, remain one of the most difficult banned methods to detect. Current methods of detection, such as the multi-factor approach of the Athlete Biological Passport (ABP) are indirect and ultimately subjective; for this reason, we desire more direct, robust diagnostic techniques. We explore methods to investigate and exploit storage-induced changes and develop a two-pronged assay to identify reinfused red blood cells (RBCs) and separate this subpopulation from fresh cells. With a combination of microfluidic and electrokinetic techniques, we are not only able to observe the deterioration of RBC electrical and mechanical properties over time, but we also show the detection of stored RBCs in an *in vitro* reinfusion as well as positive results for detection of blood doping in a round of *in vivo* ABT studies with competitive cyclists.

Advances in portable biosensors are often bottlenecked at the transducing element, which thus far remains either expensive or bulky, deterring the ability to make the diagnostics truly portable or affordable for end-users. We describe in this work a novel biosensing platform that operates without expensive fluorescent tags and labels, with a trajectory toward being truly non-optical and portable. Utilizing microelectrodes embedded into microchannels, we combine microfluidics and electrokinetics to create a novel biosensor that operates at miscible, liquid-liquid interfaces with sensitive detection capabilities. The integration of a colloidal suspension creates a moving liquid substrate capable of detecting biotin-streptavidin binding at biotin concentrations as low as 500 attomolar. This bead-based method provides a promising platform for a multitude of biosensing assays, whole blood tests and anti-doping assessments among them.

Chapter 2

Introduction

2.1 Dielectrophoresis

The following sections describe the electrokinetic phenomena dielectrophoresis, as it applies to both spherical particles, cells, and electrical liquid interfaces. This theory is utilized in later chapters to perform sensitive biodetection assays.

2.1.1 Classical Dielectrophoresis

Classical dielectrophoresis (DEP) can be described as a phenomenon in which a non-uniform electric field induces charge on an otherwise uncharged particle and produces motion. The force exerted on an isotropic, spherical particle in a non-uniform AC electric field *(E)* can be described as[1]:

$$\langle F_{DEP} \rangle = 2\pi a^3 \varepsilon_m Re[K(\omega)] \nabla |E|^2, \tag{2.1}$$

where a is the particle radius, ε_m is the relative permittivity of the suspending medium, and $Re[K(\omega)]$ is the real part of the Claussius-Mossotti (CM) factor, which describes the relative polarizability of the system as is given as[1]:

$$K(\omega) = \frac{\varepsilon_{\mathrm{p}}^{*} - \varepsilon_{\mathrm{m}}^{*}}{\varepsilon_{\mathrm{p}}^{*} + 2\varepsilon_{\mathrm{m}}^{*}}, \tag{2.2}$$

where each dielectric constant $\varepsilon^{*}$is complex and a function of frequency[1]:

$$\varepsilon^{*} = \varepsilon + \frac{\sigma}{i\omega} \tag{2.3}$$

It can be noted from Equation 2.3 that for low frequencies (ω), material conductivity (σ) dominates the complex permittivity, and thus the polarization factor, called conductive polarization. At high frequencies, the conductive term becomes negligible, and the dielectric constant dominates relative polarizability, called dielectric polarization. There exists some mid-range frequency where these charging mechanisms are balanced, and the system crosses over from one mechanism to another. This "crossover" frequency (ω_{cof}) can be determined by setting Equation 2.2 equal to zero:

$$\omega_{cof} = \frac{1}{2\pi}\left[\frac{(\sigma_m - \sigma_p)(\sigma_p + 2\sigma_m)}{(\varepsilon_p - \varepsilon_m)(\varepsilon_p + 2\varepsilon_m)}\right]^{1/2} \tag{2.4}$$

For positive values of the CM factor (Equation 2.2), particles are drawn to regions of high electric field strength, called positive dielectrophoresis (pDEP). When this factor is negative, particles will be repelled from these regions and instead be drawn to areas of low field strength, called negative dielectrophoresis (nDEP). Though systems may cross over from one charging mechanism to another, not all CM factors will change sign and exhibit a COF.

Cellular DEP poses a slightly more complex problem, due to the existence of a cellular membrane. The presence this third regime introduces another complex permittivity, and the CM factor is instead described as[1]:

$$K(\omega) = \frac{\varepsilon_{\mathrm{eff}}^{*} - \varepsilon_{\mathrm{m}}^{*}}{\varepsilon_{\mathrm{eff}}^{*} - 2\varepsilon_{\mathrm{m}}^{*}}, \tag{2.5}$$

where $\varepsilon_{\mathrm{eff}}^{*}$ is defined as the effective complex permittivity for a cell containing both cytoplasm and membrane regimes[1]

$$\varepsilon_{\mathrm{eff}}^{*} = \varepsilon_{\mathrm{mem}}^{*} \frac{\left(\frac{r_2}{r_1}\right)^3 + 2\frac{\varepsilon_{\mathrm{cyto}}^{*} - \varepsilon_{\mathrm{mem}}^{*}}{\varepsilon_{\mathrm{cyto}}^{*} - 2\varepsilon_{\mathrm{mem}}^{*}}}{\left(\frac{r_2}{r_1}\right)^3 - \frac{\varepsilon_{\mathrm{cyto}}^{*} - \varepsilon_{\mathrm{mem}}^{*}}{\varepsilon_{\mathrm{cyto}}^{*} - 2\varepsilon_{\mathrm{mem}}^{*}}} . \tag{2.6}$$

This theory is utilized experimentally in Chapter 4 for dielectrophoretic detection of storage-induced electrical changes in red blood cells.

2.1.2 Fluidic Dielectrophoresis

The theory of polarizable interfaces applied to particles can also be applied to a liquid-liquid interface. For two electrolytes co-flowing in a microfluidic channel, the DEP force can be described as[2]:

$$\langle F_{DEP} \rangle = \langle \sigma_t E \rangle = 1/2 Re[K(\omega)] \varepsilon_0 E_0^2 . \tag{2.7}$$

where the new CM factor and COF is terms of the complex permittivities of electrolyte streams 1 & 2:

$$K(\omega) = \frac{\varepsilon_2^{*} - \varepsilon_1^{*}}{\varepsilon_2^{*} + \varepsilon_1^{*}} , \tag{2.8}$$

$$\omega_{cof} = \frac{1}{2\pi}\left[\frac{(\sigma_1 - \sigma_2)(\sigma_1 + \sigma_2)}{(\varepsilon_2 - \varepsilon_1)(\varepsilon_2 + \varepsilon_1)}\right]^{1/2}, \tag{2.9}$$

This theory is experimentally validated later in Chapters 7 & 8.

2.2 Bead-Based Biosensors

The ability to detect biomolecular targets at low concentrations without labels is an important requirement in areas including clinical diagnostics, drug discovery, environmental monitoring, and biomedical research. To be successful, biosensors typically require three basic components – a substrate for specific binding to occur, a transducer to translate the binding event into a detectable signal, and a detector to measure the transduced signal.

2.2.1 Static-Substrate Biosensors

Bead-based heterogeneous biosensors use nanoparticles with surface-immobilized receptors as a biosensing substrate for detecting a wide range of biomolecular analyte targets including proteins[3], DNA, and bacteria[4,5]. In comparison to traditional substrate-based microarray technology, the high surface-area-to-volume ratio of functionalized nanoparticles can lead to increased detection sensitivity and reduced assay time. Bead-based methods, for example, have been shown to increase the limit of detection (LOD) in SPR sensing[6], fluorimetric assays[7], and electrochemical amperic detection[8] and have been used in a broad range of colorimetric[5], enzymatic[9], mechanical[10], electrochemical[11] and fluorimetric[7] assays.

Nanoparticle-based biosensing is often accomplished using a heterogeneous support, where particles are adsorbed onto a solid surface[12] or a sol-gel matrix[13]. Nanoparticles functionalized with specific receptors are then flushed with a fluid or gas containing the relevant target analyte. Because colloids must be functionalized and assembled, current bead-based methods typically require multiple rinsing/drying steps[14,15], can suffer from functional group crowding[16] and surface fouling[17], and are usually designed for single use.

2.2.2 Liquid-Liquid Interfacial Biosensors

To reduce detection time and assay complexity, and to improve portability, biosensors can be integrated with microfluidics. With microfluidics, biomolecular binding can occur in solution phase at the interface formed between laminar liquid streams using low Reynolds number fluid flow. This sensing strategy is robust and has been successfully applied to detecting DNA hybridization[18] and for protein immunoassays[19].

Laminar liquid interfaces can be created using “T-channel” or “Y-channel” microfluidic geometries[20,21]. The two fluids produce a quasi-stable liquid interface at their co-flowing contact region, where at low Reynolds number mass transport across the interface is driven strictly through diffusion[22]. Performing biosensing though diffusional mixing and biomolecular binding has several advantages over traditional heterogeneous biosensing at solid substrates. First, because biomolecular binding occurs in solution phase as opposed to a solid surface, diffusion-limited binding occurs over much shorter timescales. Second, the interfacial substrate is continually replenished and renewed at any given position in the microchannel and is therefore not subject to surface fouling and non-specific adsorption.

Despite the usefulness and advantages, current liquid interface-based microfluidic strategies require fluorescent labeling and fluorescent microscopy for signal transduction and detection[23]. By utilizing the fDEP theory outlined in Equations 2.7-2.9, we can use alternating current (AC) electric fields to polarize and electrically stress an electrolytic interface with a mismatch of electrical properties on either side. When an electric field is applied, charges accumulate and force the interface to deflect across a microfluidic channel. The magnitude and direction of this deflection is sensitive to the interfacial electrical properties[2]. Exploiting this phenomena, Mavrogiannis et al. demonstrated that interfacial biomolecular binding influences the liquid electrical conductivity and polarizability of the liquid interface, and that binding can be detected by quantifying the degree of interfacial deflection at varying positions down the microchannel[24]. In this way, binding is transduced as a change in the interfacial deflection of the fluid interface, which can be imaged and detected optically or electrically without labels; this detection method is termed interfacial electrokinetic transduction (IET)[24].

In Chapter 8, we extend the usefulness of IET to that of nanoparticle bead-based assays investigate the ability to detect biomolecular binding on the surface of functionalized colloids subjected to specific biomolecular binding events suspended in solution in the vicinity of a liquid interface.

Chapter 3

Detailed Methods and Protocols

The following sections describe, in detail, the methods and procedures used throughout the entirety of the experimental chapters. The methods in this chapter are a combination of manufacturers' recipes and insights gleaned from countless rounds of trial and error and have been adapted over the years to suit the distinct fabrication needs of this work.

3.1 Photomasks

Several types of microelectrodes and numerous different systems of microchannels are used in the body of this work. The processes to create these features are lengthy and situation-dependent, but all microfabrication methods first require a photomask. Photomasks are created with computer-aided drafting software, AutoCAD. All lines must be joined and closed to produce masks. In the event that the polylines cannot be closed, and the lines of each object to be joined are drawn in the same layer, duplicate lines and zero-width points can be made redundant with the “OVERKILL” command, and the lines can then be successfully joined and closed. The 2D wireframe drawing is saved as a 2010 “.dxf” file and converted to a Gerber “.gbr” file with licensed software, LinkCAD. This step is not required, but is recommended to avoid incurring conversion fees from photomask companies. Each layer in the .dxf file will produce a separate .gbr file; separate layers are helpful when creating positive and negative masks in the same AutoCAD drawing.

Gerber files are sent to the photomask company FineLine Imaging in Colorado Springs, Colorado. For minimum mask feature sizes smaller than 7 microns, a chrome mask is required and FineLine Imaging cannot be used. For all other sizes, transparency masks are readily printable with pricing brackets corresponding to mask minimum feature sizes. All masks should be produced as 5”x5” films; this size is well-suited for mounting on borosilicate glass or quartz used with the UV source and mask aligner.

Masks for microelectrodes are positive, or “clear field,” and are submitted to FineLine with “Image Orientation and Polarity” as “Clear Field, Right Read Down” (CFRRD). These masks are, in most cases, used with gold-covered coverglass and a positive photoresist (e.g. MICROPOSIT^{TM} S1800^{TM} series). Exceptions apply when a lift-off method, described in detail in section 3.2, is used to fabricate either gold or indium tin oxide (ITO) electrodes. In this case, a negative, or “dark field” mask is created and submitted to FineLine as “Dark Field, Right Read Down” (DFRRD). Masks may also be submitted Right Read Up (CFRRU or DFRRU) if designs are symmetrical, but is not recommended, as texts and orientation-dependent designs will print reversed.

Masks for microfluidic channels are negative, or dark field, and are submitted to FineLine as DFRRD. These masks are used with 4-inch, single side polished (SSP) silicon wafers and negative SU-8 epoxy photoresists (e.g. SU-8 3000 series, SU-8 2100 series), and produce master molds with rectangular channel profiles, and are suitable for most microfluidic uses. Exceptions apply when a rounded channel profile is needed, which is produced by positive SPR photoresists (e.g. MEGAPOSIT^{TM} SPR^{TM}220 series); this requires a positive, or clear field, mask and is submitted to FineLine as CFRRD.

3.2 Microelectrodes

Some electrodes vary only in their design, and are fabricated using the same protocol. In Chapter 4, two sets of electrodes utilize the same design, but are composed of two different metallic makeups, and require entirely separate protocols. In this work, a quadrupole electrode array is used to create distinct regions of high and low electric field strength, for the purpose of tracking electrical behavior and separating particles and cells of interest. The electrode array used in Chapters 7 & 8 is comprised of two sets of linear electrode arrays, mirrored across a long axis, such that the arrays of points face each other, for the purpose of focusing the field at the interface of two laminar streams in a microfluidic device. Though they may differ in design and composition, all electrodes in this body of work deliver an electric field to samples or buffers of interest through direct contact. Contactless electrodes require different materials and fabrication procedures, which are neither used nor described in this work.

3.2.1 Physical vapor deposition

Electrodes used in this work are created top-down; layers are first built up through physical vapor deposition (PVD), then selectively removed to create the desired structures. PVD, is an umbrella term for several different vacuum-facilitated deposition methods, including electron beam, evaporative, and sputtering PVD, which differ in how the target material is vaporized for subsequent deposition on the coverglass. In this work, we first clean glass coverslides (50x30 mm, no. 1, Fisher Scientific) in an acetone bath followed by an isopropyl alcohol (IPA) bath, followed by blow drying with dry nitrogen gas. Slides that have not been cleaned in this manner will exhibit poor adhesion to the following deposition layers, and may wipe or wash off. Using electron beam PVD, the slides are coated with a 20 nm layer of chromium, followed by a 30 nm layer of gold (Kurt J. Lesker Company). Chrome is inexpensive and bonds well to both glass and gold, but is cytotoxic to live cells – titanium or platinum can be substituted for this layer in this case. The layer thickness described can be modulated without loss of electrical performance, though etching times may vary. Layers as thin as 10 nm chrome and 20 nm gold have been used in this work with no noticeable differences between devices.

3.2.2 Photolithography

Positive photoresist (S1813, Shipley) is spin-coated onto the gold-coated slides at 2000 rpm for 60 seconds, creating a 2 μm layer of photoresist. The slides are rinsed with acetone and IPA, followed by a dehydration bake at 110-130°C for at least 10 minutes. If the slides have been stored, or if the atmosphere is humid, these cleaning steps are imperative. Dehydration temperature should not exceed 150°C – at this temperature the gold and chrome layers anneal together and do not etch well. Resist is baked for 2 minutes at 95°C before exposure to light source at 95 mJ/cm^2. Exposure to light selectively crosslinks the photoresist; washing in a bath of developer (CD-26, Shipley) removes areas exposed to light, leaving a protective mask that resists etching. The slide is rinsed in DI water and carefully blown dry with dry nitrogen. The quality and integrity of the design in the photoresist is checked under a microscope – at this point, if the quality of the lithography is poor, the resist can be washed off with acetone and IPA and respun, exposed and developed; however, once the slide is etched, the design is permanent and cannot be redone. Developed patterns that appear to be blown away by the pressure of the drying nitrogen are indications of poor resist adhesion. If resist adhesion is still poor after care has been taken to clean and dehydrate the slide, hexamethyldisilazane (HMDS), an adhesion promoter, is spun onto the slide (though vapor deposition is preferred) prior to the resist, using the same spin recipe. Caution is exercised, and the spin-coater and slide is allowed to vent in the fume hood for several minutes prior to spin-coating the photoresist, as HDMS is corrosive and toxic, and should never make contact with skin or be inhaled.

3.2.3 Wet etching

The top layer of gold is etched first with an iodine-based gold etchant (Alfa Aesar). The gold layer etches in seconds and is visually evidenced by the dissolution of gold's characteristic shine. Gold is easily over-etched and will undercut the resist layer and must be removed from the bath and immersed in a deionized (DI) water bath immediately upon completion of etching. The slide is then placed in a bath of chrome etchant (Alfa Aesar), which etches more slowly and does not as quickly undercut the gold layer. The glass slide can be removed when the background of the slide becomes transparent and be rinsed with DI water before washing with acetone and IPA. Etching steps should be performed in either Teflon dishes or some other hydrophobic fluoropolymer dish, as performing these steps in glass dishes will etch the glassware over time. Electrical leads are soldered to the electrode array with indium pellets (Sigma Aldrich); soldering on a hot plate set at its lowest temperature is recommended, as a standard lab bench top acts as a heat sink and makes soldering on thin coverglass difficult. For most work in Chapter 4, the prepared electrode array is ready to use. For select parts of Chapter 4, and for the entirety of Chapters 7 & 8, the electrodes must be paired with a microfluidic flow layer before use.

3.2.4 Lift-off technique

Most work in Chapter 4 uses gold electrodes fabricated with the methods described above. Other experiments in this chapter utilize ITO electrodes, which are an attractive option due to the transparency of thin ITO films. ITO is readily deposited using electron beam PVD but requires either harsh proprietary etchants or 1 molar hydrogen chloride (1M HCl), both of which are strong acids and regularly undercut resist and destroy the integrity of designs and are difficult to dispose of – trace amounts of ITO etchant in DI water stain the water bath and the laboratory sink and may damage baths and sinks that are not HCl compatible. Etching quality is enhanced on purchased, pre-coated ITO glass slides, but are limited to predetermined slide thicknesses which are not suited for high-objective imaging. A lift-off method is more desirable for both safety and expenses.

Lift-off is a top-down fabrication technique requiring a sacrificial layer to impede deposition of the target metal in undesired areas. Both positive and negative resists can be used to perform lift-off with the appropriate coordination of mask polarity – a positive resist used with a negative mask, and a negative resist used with a positive mask. In this work, positive resists S1813 is used with a negative photomask, and the resists is spun, baked, exposed, and developed in the same manner as the standard gold etch method. After the design is inspected, the slide undergoes electron beam PVD to deposit ITO to a thickness of 180 nm. The ITO-coated slides are washed in an acetone bath to dissolve the photoresist and remove the ITO from the masked areas. A staining jar with an acetone-resistant lid is preferable for this step; flat dish baths may dissolve the resist and allow the ITO to settle onto the glass surface, where it becomes difficult to remove without damaging the electrode design. The ITO electrodes then undergo an annealing step on a hot plate for 2 hours at 500°C – this process transforms the ITO into a transparent conductive film[25,26]. After 2 hours, the hot plate is turned off and the transparent slides are left to cool on the hot plate; premature removal of slides from the hot plate can cause thermal shock and break the thin coverglass.

The resulting ITO electrodes do not bond to indium solder, and an additional chrome deposition step is added – the slide is masked with paper and tape such that chrome deposits only on the four corners of the slide, overlapping the ITO in those areas. Electrical leads can then be readily soldered to the electrodes. Alternatively, conductive copper tape can be used to create electrical leads directly on the ITO, though soldering is a more permanent method and is preferred.

3.2 Microchannel fabrication

Microfluidic flow channels are utilized extensively in this work. The soft lithography process used to create them is not unlike the photolithography process used to create the microelectrode arrays that end up embedded in many of the channels.

3.2.1 Soft lithography

To fabricate the microchannel, we instead begin with a 4-inch SSP silicon wafer (University Wafer), washed with IPA and dehydration baked at 200°C for at least 30 minutes. The wafer is centered on the spin-coater and the alignment checked by briefly spinning the wafer and adjusting the position if necessary. For most flow channels in this work, a rectangular channel cross section is desired. The appropriate SU-8 series of epoxy-based, negative photoresist for the desired channel height is used and spin-coated onto the wafer according to the manufacturer's datasheet. Soft bake times, exposure energies to be used with a negative photomask, post exposure bake times, and development times vary for each recipe, and should be followed according to the appropriate datasheet. The wafers are hard baked at 200°C for at least 2 hours, after which the hot plate is turned off and the wafer allowed to cool on the hot plate. Premature removal of the hot wafer can cause thermal shock and crack the epoxy design.

The cooled wafer is a master mold from which as many microchannels can be cast until the design degrades or the wafer breaks. The channels are cast by pouring a silicone-based polymer, polydimethylsiloxane (PDMS), over the wafer in a round-base weigh boat. For most uses, PDMS is mixed in a 10:1 elastomer-to-curing-agent ratio, though the stiffness of the resulting polymer can be modulated by varying the ratio. In most cases, PDMS is asymmetrically mixed in a planetary mixer (Thinky USA), which effectively mixes PDMS volumes weighing up to 55g. Heavier quantities will break the bottom of the mixing cup and spill the PDMS into the mixer, and thus must be mixed thoroughly by hand with a glass stir rod. The wafer is left at room temperature for at least 15 minutes before baking at 85°C for 15-30 minutes. At least 15 minutes is required to allow microbubbles created from pouring the PDMS to absorb into the bulk, even when there appear to be no microbubbles. Premature heat-curing of the polymer immobilizes air bubbles within the polymer – these bubbles are most often over the fluid ports and typically cause leaks at the inlet and outlet of the device. Alternatively, the wafer can be left at room temperature overnight with a final curing at 85°C for 10-15 minutes. Hand-mixed PDMS must be cured overnight at room temperature to absorb and disperse the air introduced while mixing. Once cured, the PDMS is peeled from the wafer and cut to size, and fluid ports are created with 0.75 mm biopsy punch (Ted Pella, Inc.). PDMS consumption can be reduced by 50-75% by removing only the PDMS around the microchannels with a razorblade, leaving the outlining regions on the wafer; the wafer subsequently requires only 10-25g of PDMS to recast the microchannels.

3.2.2 Alignment and bonding devices

The resulting microchannels are bonded to coverglass to seal the channels and allow fluid flow. In Chapter 5, microchannels are bonded to plain coverglass by exposure to oxygen plasma (Model 42A, Jetlight) for 1 minute, and immediately bringing the two pieces into contact to seal. In Chapters 7 & 8, electrodes must be embedded symmetrically along the length a long microchannel. The electrodes and PDMS are exposed to oxygen plasma for 1 minute, and immediately aligned down the entire length of the microchannel by eye and hand under an inverted microscope, bringing the two pieces into contact to seal the channels, before baking overnight at 85°C.

3.2.3 Multi-layer designs

Select work in Chapter 4 utilizes a microfluidic push-down valve system to quickly stop and start flow within the device. This design requires a multi-layer device, where a thin channel flows below a perpendicular channel dead-end filled with water. When pressure is applied to the dead-end channel, this top layer pushes down and pinches off the bottom layer in the overlapping areas, stopping the flow. To effectively halt the main flow channel, the flow channel cross-section must be rounded, as opposed to rectangular. To achieve a rounded channel profile, positive photoresist SPR220 series is spun for a 15 μm channel height and exposed with a positive photomask according to the manufacturer's datasheet.

The upper valve layer is fabricated with the previously described methods for rectangular channel profiles. The flow layer is cast in PDMS following the hard bake step; the PDMS of this layer must be thin and flexible, such that it creates a deformable membrane in the regions overlapping with the layer above. To facilitate peeling of a thin flexible layer, the wafer is silanized in a fume hood by placing the wafer and weigh boat in a vacuum desiccator and pipetting a few drops of trimethylchlorosilane (TMCS) on the wafer surface. The desiccator is closed and vacuumed for 1 minute before closing the vacuum valve and allowing the wafer to sit under vacuum in the silane gas for 1 hour. The wafer is then spin-coated with PDMS mixed in a ratio of 20:1 to a total thickness of 30-40 μm. The top layer is cast by pouring 45g of PDMS in a 10:1 ratio. Both wafers are cured overnight at room temperature, followed by a 15-minute bake at 85°C. The top layer is peeled off – if the multi-layer design requires tight control over alignment of the layers, it is often easier to cut and align each device on its own. In both cases, inlets are punched in the valve layer with a 0.75 mm biopsy punch. The thin PDMS layer remains on the wafer for alignment – the wafer is placed under an inverted microscope, and the top valve layer is aligned by hand and placed onto the bottom layer. The wafer is baked again with both layers at 85°C overnight. The two layers can then be easily peeled from the wafer, and the flow layer inlet and outlet at created with a 0.75 mm biopsy punch. The multi-layer assembly can then be exposed to oxygen plasma, aligned and bonded onto a quadrupole electrode array and baked overnight.

3.3 Blood sample preparation

The following sections describe the methods used to draw, store, and prepare blood samples for studies in this work. Chapters 4 & 5 use blood sourced from vendors, volunteered from graduate students, and volunteered from competitive cyclists. All human blood in this body of work is of male origin. All studies were performed with the Homewood Institutional Review Board (HIRB) approval, and with proper blood borne pathogen laboratory safety training and certification. All mammalian blood is handled in a biological safety cabinet designated exclusively for use with mammalian cells, and all biological waste is bleached prior to disposal. All solutions are made with 18 MΩ deionized water.

3.3.1 Blood sourcing, drawing, and storage

Blood was purchased from both non-human mammalian (Quad Five) and human (Zen-Bio, Inc.) blood sources. Non-human mammalian (referred to in this body of work as “animal”) blood was obtained from equine (horse), caprine/hircine (goat), ovine (sheep), and bovine (cow) sources with a citrate anticoagulant additive. Human blood vendors provided anonymous datasheets of donor sex, age, blood type, ethnicity, etc. with each sample containing a citrate phosphate dextrose (CPD) anticoagulant additive. Both animal and human blood sourced from vendors were divided into 0.5-1.0 mL aliquots upon arrival.

For student volunteers, only male graduate students within the Department of Chemical and Biomolecular Engineering were considered. Modest monetary compensation was offered at $10 per blood draw session, with a $30 bonus for completing all scheduled draws. All participants were given an HIRB-approved outline of the study and informed consent form. Volunteers signed and participated of their own free will; electronic and print copies of their signed consent forms are retained for laboratory records, along with a confidential identity key – in this manner, all data identifiers remain anonymous for publications. Five students were selected based on their availabilities and willingness to complete the full schedule of blood draws.

Finger prick blood samples were drawn from volunteers with fingertip lancets (Owen Mumford) and allowed to pool on the fingertip. In most cases, optimum blood draw was facilitated by physically massaging more blood down the hand and into the finger. On cold days, two finger pricks were often necessary. Large gauge lancets can be acquired to increase the volume of a single draw; however, all volunteers readily offered multiple draws per session with no comments or complaints of discomfort. The volume of blood was quantified by drawing up the drop with a micropipette, and then stored in CPD in a ratio of 1:8 anticoagulant-to-whole-blood. Typical finger prick blood draws ranged from 50-100 μL. One sample was collected per week for a duration of 7 weeks. All blood samples and aliquots are stored at 4 °C in a blood bank refrigerator (Jewett). Blood storage time varied from 0-6 weeks, and a new aliquot was used for each experiment.

3.3.2 Washing

All blood samples require washing steps to isolate the red blood cells (RBCs) for experiments. Centrifugation of whole blood separates the blood components by weight, with red blood cells gathering as a pellet at the bottom. Three washing cycles are necessary to ensure complete removal of all other components. At the appropriate time point, the required volume is removed from a new aliquot and added to a microcentrifuge vial with 1.0 mL of isotonic phosphate buffered saline (1X PBS). The dilution is centrifuged at 2000 relative centrifugal force (rcf) for 2 minutes, the supernatant removed and replaced with fresh 1X PBS, and vortexed to mix the fresh suspension. Care is taken when handling samples and buffers; pipette tips are discarded immediately after a single use, as inattention can cause cross-contamination of samples and contamination of stock solutions.

In Chapter 5, the third removal is followed by resuspension in a solution of 1X PBS containing 0.5% (w/v) methylcellulose (mc). Methylcellulose is added to increase the viscosity of the buffer and prolong the suspension of RBCs in solution. The resuspension volume must achieve a ratio of 1:50 whole-blood-to-final-volume for the studies outlined in Chapter 5. Methylcellulose does not readily dissolve in aqueous solutions and requires agitation with a magnetic stir bar at high revolutions for several hours, preferably overnight. The solution is easily aerated upon shaking and must rest before use. Methylcellulose solutions are passed through a 0.2 μm filter before every use, which effectively prevents clogging in microchannels for the duration of the experiments. Microfluidic devices used with methylcellulose are single-use; attempting to flush and reuse a device typically leads to clogging within minutes.

3.3.3 Glutaraldehyde fixation

In Chapter 4, the third removal of the supernatant from the RBC washing steps is followed by resuspension in a solution of 1X PBS. 25% (w/v) stock glutaraldehyde (glt) is added to this suspension in appropriate volumes to yield an overall concentration of 0.15-2.5% (w/v) glt. Glutaraldehyde crosslinks the membrane-bound and interior proteins of the RBCs, and begins immediately upon addition to the suspension. The samples are placed in a vial rack, covered tightly with tape, and placed on a shaker at room temperature to fix for 1 hour under gentle agitation. The fixed samples are then washed three times with 1X at 6500 rcf for 5 minutes. During post-fixation washing steps, cells pellet densely at the bottom of the vial and may not completely resuspend by vortexing – in this case, the bottom of the vial can be gently flicked several times with a finger to dislodge the pellet, and vortexed to resuspend. Following the 1X PBS washing steps, the fixed cells are washed again with the experimental buffer, a zwitterion solution of 0.8-3M 6-aminohexanoic acid (AHA) (Sigma Aldrich). The cells are washed and resuspended one last time in the experimental buffer before use.

3.4 Flow sources

Flow is driven through microchannels by a number of methods. This work utilizes the following three methods with varying degrees of success. In each chapter containing experimental work, a different degree of fluid flow control is required to adequately and precisely control the experimental parameters, and a different flow source is found to provide the desired amount of control and user input.

3.4.1 Syringe pump

Syringe pumps are often microfluidic flow sources and are well-suited as a flow source in Chapter 5. This work requires simultaneous control of two flow rates, which must remain identical. A more sophisticated, automated flow controller can be used here, although it is not necessary. A syringe pump is not desirable for the work in Chapter 4, as halting the flow driven by a syringe pump rapidly increases the internal pressure of the microfluidic device and invariably leads to device rupture. There is use for a syringe pump in the work outlined in Chapter 5, though independent flow rate control over two streams is desired, and thus requires either two syringe pumps or a combination of flow sources. A syringe pump is insufficient for the work described in Chapters 7 & 8, where a steady, position-dependent interface must be maintained. The pulsatile nature of the syringe pump flow creates a visibly oscillatory interface, which makes data measurements difficult.

3.4.2 Automated flow controller

The automated flow controller in this work is an OB1 mk3 model purchased from ELVESYS. The costs of flow controllers of this caliber routinely exceed $20,000 USD and require proprietary accessories to facilitate sample delivery to devices. When paired with propriety flowrate sensors and software, a feedback loop allows continuous monitoring and control of the overall flow rate through automated pressure regulation; in this manner, flow can be delivered as either constant pressure or constant flow rate. This is a desirable option for experiments with long run times; if a feedback loop is not engaged, depletion of sample volumes lowers the hydrostatic head and produces a decreasing flowrate over time for a constant pressure source. This system is sophisticated, requires little user input or intervention, and meets most microfluidic needs. However, through experience and time, the work in Chapters 7 & 8 favors use of our manual flow controller described in the next section over the automated black box controller.

3.4.3 Constant pressure manual flow controller

3.4.3.1 A low-cost microfluidic flow controller

Our microfluidic flow controller drives fluid flow through microfluidic channels using a constant pressure source. Unlike commercial solutions, the entire system uses readily available plastic fittings, costs $500 USD and requires less than 1 hour to assemble. The system, illustrated in Fig 1, is capable of delivering flow to four independently addressable microfluidic channel inputs at a fraction of the cost of a single syringe pump. Pressurized house air (~50 psi) powers the flow controller. As shown in Figure 3.1, blue airline tubing exits a pressure regulator and is split into four separate lines (labeled 1, 2, 3, and 4) using an aluminum pressure manifold. A 3-way air switch controls the flow of pressured air into each line. When each switch is turned, pressurized air is sent into a precision pressure regulator, which controls the output pressure and directs this into a fluid-filled cryogenic sample vial. The pressure inside the vial increases and drives fluid flow through the tubing and the microfluidic device. We control the flow rate by adjusting this pressure using the precision pressure regulator and monitoring the air pressure on the accompanying pressure gauge.

3.4.3.2 Hydraulic circuit analysis

To regulate the fluid flow rate and render it independent to varying device geometry, we place hydraulic resistors upstream of the microfluidic device. The resistors are short lengths of capillary tubing and have a much larger hydrodynamic resistance than the downstream microfluidic device.

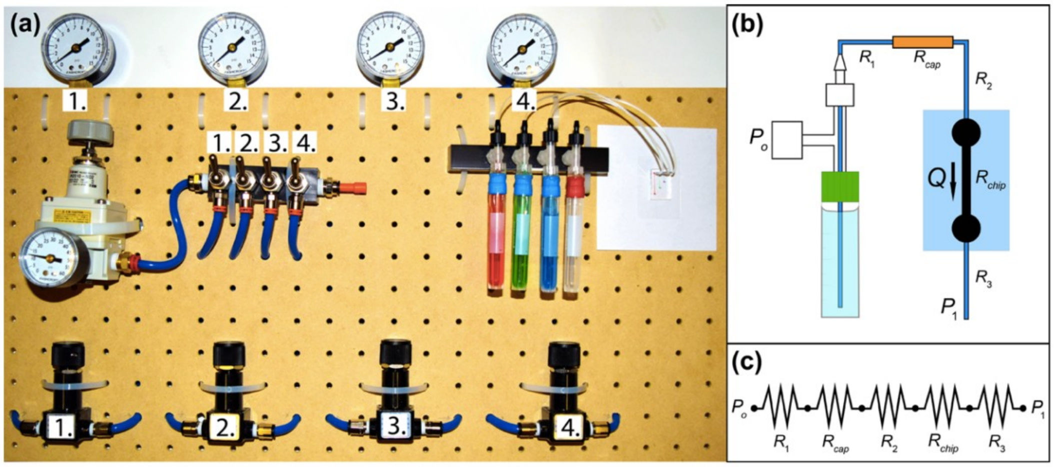

Figure 3.1. (a) Low-cost microfluidic flow controller for controlling flows through four fluidic inlets. (b) Schematic of pressurized sample vial. A pressure (P_o) is applied to a cryovial and fluid flows through a series of tubing resistors (R_1), a capillary resistor (R_{cap}), R_2, into the device (R_{chip})

and exiting through outlet tubing (R_3) at a flow rate Q. (c) Hydraulic circuit diagram of the fluidic system.

In this way, fluid flow through the micro device is dictated by the resistance of the upstream hydraulic resistor and not the microfluidic device. These hydraulic resistors are a useful feature of this system because changes in device design will not influence the pressure-flow relationship within the microfluidic chip. Therefore, the user only needs to measure the pressure-flow rate relationship once, and it will remain accurate for devices of related, but different geometry.

Constant pressure sources can be reliably engineered to produce well-controlled flows in microfluidic systems using hydraulic circuit analysis. This method treats a network of microchannels as a complex circuit of fluidic resistors. For low Reynolds number flow in microchannels, there is an approximately linear relationship between pressure and flow rate. For an infinitely long cylindrical microchannel with a uniform circular cross section area, A, channel radius R, aligned in the positive z-direction, the fluid velocity profile at any given radial point r in the channel cross-section is given by

$$u_z = -\frac{1}{4\mu}\frac{\partial P}{\partial z}(R^2 - r^2), \tag{1}$$

where μ and $\partial P/\partial z$ are the fluid viscosity and axial channel pressure gradient, respectively. To calculate the flow rate, the fluid velocity profile can be integrated over the channel cross-sectional area

$$Q = -\frac{AR^2}{8\mu}\frac{\partial P}{\partial z}. \qquad (2)$$

Assuming the channel length (L) is much larger than the channel radius (R), we can neglect entrance effects and treat each channel as an infinitely long tube. Replacing dP/dx with $\Delta P/L$, where $\Delta P = P_{IN} - P_{OUT}$, is the pressure drop across the channel (e.g., the difference between the pressure at the inlet and the outlet), we can write this relationship between pressure and flow rate as

$$Q = \frac{\Delta P \pi R^4}{8\mu L}, \qquad (3)$$

which is known as the Hagen-Poiseuille law. Based on Eq. (3), an applied pressure drop produces a flow rate Q that is proportional to the channel's hydraulic resistance (R_h): $8\,\mu L/\pi R_h$. The Hagen-Poiseuille law describes to a good approximation the relationship between applied pressure and flow rate. It is analogous to Ohm's law for electrical circuits, where the voltage (pressure) is proportional to the current (flow rate)

$$\Delta P = QR_h\,. \qquad (4)$$

This equation provides a good estimate for steady flow through long and narrow cylindrical microchannels, however, this relation can be extended to other channel shapes by replacing R with the hydraulic radius, $r_h = 2A/P$, where A and P are the channel cross-sectional area and perimeter, respectively. Using Eq. (3), we can design hydraulic resistors that serve as a bottle-neck for regulating flow rate within varying microfluidic device geometries.

3.4.3.3 Regulating flow rate

We used hydraulic circuit analysis to design fluidic resistor elements that can predictably restrict the flow rate through an arbitrary microfluidic device. To generate microfluidic flow, we apply a known air pressure (P_o) to a sealed fluid-filled vial and maintain the device outlet at 1 atm (P_1), as depicted in Figure 3.1(b). Each flow line has five fluidic circuit components that influence the flow rate in a microfluidic device (Figure 3.1(c)). When the flow controller delivers a pressure, P_o, to the sample vial, the pressure drives fluid flow into the submerged tubing and into the microfluidic device.

One way to control fluid flow to the microfluidic chip is to insert flow elements with a large hydraulic resistance such that it dominates the pressure-flow rate behavior of the entire fluidic circuit. Illustrated in Figure 3.1(c), fluid will flow through five hydraulic resistors — the submerged inlet tubing (R_1), the capillary resistor (R_{cap}), tubing at the microfluidic inlet (R_2), the microfluidic device (R_{chip}), and the outlet tubing (R_3). Modifications to any of these components directly influence the overall resistance of the entire fluidic circuit and resulting pressure-flow rate relationship. To design capillary circuit elements with sufficiently large enough hydraulic resistance to regulate flow, but not too large that flow is impeded, we measure the resistance of the microfluidic device (R_{chip}) and calculate the length of capillary tubing required such that $R_{cap} \sim 10 \times$

$(R_{chip} + R_1 + R_2 + R_3)$. If the capillary tubing has a resistance significantly larger than the remaining elements in the hydraulic circuit, it will serve as a predictable bottle-neck for regulating fluid flow rate.

3.4.3.4 Flow controller assembly and testing method

Here, we describe the assembly and operation of our microfluidic flow controller and the design of hydraulic resistors for flow rate regulation.

3.4.3.4.1 Essential components

Construction of the flow controller takes less than 1h and requires three primary assemblies: a pressure manifold, a multi-line manifold, and a sample holder. The entire system is powered by pressurized air and uses a series of pressure regulators, pneumatic air switches, and manifolds to control gas pressure inside sealed liquid-filled cryotubes and direct flow to microfluidic channels. To regulate the air pressure, we direct house gas (50 psi) through an air filter and into a primary pressure regulator (SMC Pneumatics, IR2010-NO2), where it exits at a fixed pressure (20psi). We use a pressure manifold with one inlet and four outputs (McMaster-Carr, 5469K121) to deliver this regulated air pressure to four separate fluid-filled cryovials. Each manifold output is fitted with a 3-way air switch (Pneumadyne, C030621) to control the gas flow to downstream precision pressure regulators with accompanying pressure gauges (McMaster-Carr, 3846K411). The precision regulators control the gas pressure delivered to each cryovial, and the corresponding pressure gauges provide an easy way to monitor regulator pressure. Each of the airlines then connect to a multi-line manifold, which holds fluid-filled cryotubes for sample holding and pressure-driven fluid delivery to the microfluidic device. To deliver flow, we use a precision regulator to increase the air pressure inside a desired cryovial, which then forces flow through the submerged tubing and out into the chip. We can control the flow rate in each sealed vial by increasing or decreasing the vial pressure using the appropriate precision pressure regulator.

3.4.3.4.2 Flow controller assembly

To make this system easy to setup and operate, we attached the pressure manifolds, air regulators, and gauges to an inexpensive wooden pegboard using plastic cable ties. Before assembly, all threaded fittings were wrapped with two layers of Teflon tape to ensure a proper seal and prevent gas leaks. All components were fitted with push-to-connect fittings and connected with 1/4” PTFE tubing. The pressure manifold inline/outline was fit- ted 1/4–1/8 National Pipe Thread (NPT) male fittings (McMaster-Carr, 5779K108), and each gas outlet threaded to 3-way switches (Pneumadyne, C030621) with 1/4-10-32 UNF male connectors (McMaster Carr, 5779K246). Each switch controlled the airflow on/off to a precision pressure regulator (Airtrol, R-800-10) with 1/4-1/8 NPT male connectors. Regulator outlets were attached to pressure gauges (0–15 psi, McMaster-Carr, 3846K411) threaded into 1/8” brass T’s with 1/8” NPT male fittings.

3.4.3.4.3 Sample holder assembly

We used sealed cryovials as inexpensive and readily available pressure vessels for delivering fluid flow to microfluidic channels. The cryovial assembly houses the necessary components to load the fluid samples and to pressurize and direct their flow. Tubing from the outlet of each pressure gauge was connected to the back end of a multi-line manifold with 1/8” NPT connections and we connected male luer-lock fittings (7/16” hex–1/8-27 NPT, Value Plastics) to the front of the manifold. To attach a sealed vial to each of these fittings, we modified the top cap of each cryovial by drilling a small 3 mm diameter hole in the cap of each cryotube and attaching it to a plastic male luer fitting (7/1600 hex–1/8-27 NPT, Value Plastics) using quick setting epoxy. After allowing the epoxy to cure for 15 min, we fitted the cap with the bottom of a male luer tee fitting.

3.4.3.4.4 Connecting the tubing

The final step in completing the sample assembly is to create an airtight connection that allows for the sample to flow from the pressurized cryotube, through submerged tubing and into the microfluidic device. To do this, we make use of a female luer lug tee fitting. This inexpensive fitting has two openings and a third centered and oriented perpendicular to each opening. We attached the cryovial to the bottom opening of the tee fitting. At the top opening, we pushed plastic tubing (Cole Palmer), through a fitted male lock ring (Value Plastics), leaving 4” of exposed tubing within the cryovial. Epoxy was applied to the junction of the lock ring and tubing to make an airtight seal. The other end of the tubing is connected to a specific microfluidic device inlet. When pressurized, the fluid inside the vial will be driven into the tubing and the microfluidic device.

3.4.4 Supplementary materials

3.4.4.1 Hydraulic resistance measurements

We first used the flow controller to drive fluid flow at different applied pressures through microchannels of varying length. As shown in Figure 3.2, the flow rate was measured through microchannels 0.5, 1 and 1.5 cm in length and plotted as a function of applied pressure. All flow rate measurements were performed with microfluidic flow sensors (Elveflow MFS 2 and MFS 3). As expected and depicted in Figure 3.2(a), the Q-P relationship for each channel is significantly influenced by channel length and the slope of each dataset was used to determine each channel’s experimental hydraulic resistance. Using Eq. (3), we determined the length of capillary tubing required to exceed the hydraulic resistance of the longest microchannel by a factor of 10. We then repeated these experiments with this length of capillary tubing (15.5 cm) inserted upstream the inlet of each microfluidic channel. Since the capillary tube had the largest hydraulic resistance in the system, the flow rate for the system was dictated by the capillary tube, therefore, the flow rate was seen to be largely independent of the channel length (Figure 3.2(b)).

3.4.4.2 Flow rate capabilities, stability and response time

To demonstrate our system is a feasible low-cost alternative to commercial syringe pumps, we performed real-time flow response comparisons between the flow controller and a commercial syringe pump. Using a passive in-line flow sensor, flow rates were measured for both the flow controller and syringe pump in response to a step change in pressure. A time-response and stability comparison between the syringe pump and flow controller is shown in Figure 3.3(a). As illustrated, the flow controller has a significantly faster response time than the syringe pump, requiring less than 5 s to switch from a flow rate of 3 μL/min to 6 μL/min. The syringe pump, however, took upwards of 60 s to reach steady state. The flow rate stability is approximately the same for both the syringe pump and flow controller with an approximate 0.2 μL/min variation. The syringe pump, however, becomes pulsatile and unstable at a low flow rate (1 μL/min), shown in Figure 3.3(b). Comparing the stability of both the flow controller and syringe pump, one can see the syringe pump produced a pulsatile flow, while under the same conditions the flow controller produced a constant flow. Finally, it is important to note the operating range of the flow rates produced by the flow controller. We found the flow controller can provide reliable and steady flow rates from 0.5 to 35 μL/min with a 15.5 cm long capillary resistor. However, the user can alter this range by adjusting the length of the upstream capillary tubing. A longer capillary, for example, will produce a smaller flow rate, while a shorter capillary tube will allow for increased flow rate.

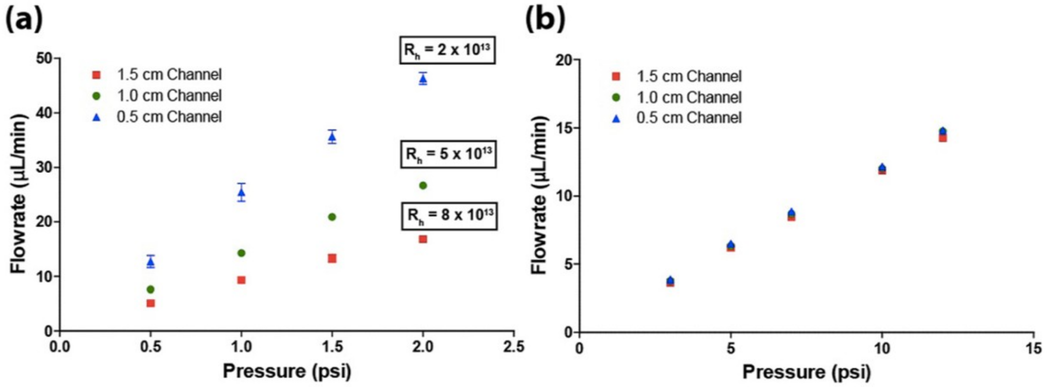

Figure 3.2. (a) Pressure versus flow rate for three channel lengths without a capillary tube. (b) Pressure versus flow rate for three channels with an upstream capillary resistor and with a capillary tube. All three datasets collapse to single curve, with minor deviation (0.5 µL/min) at larger pressures.

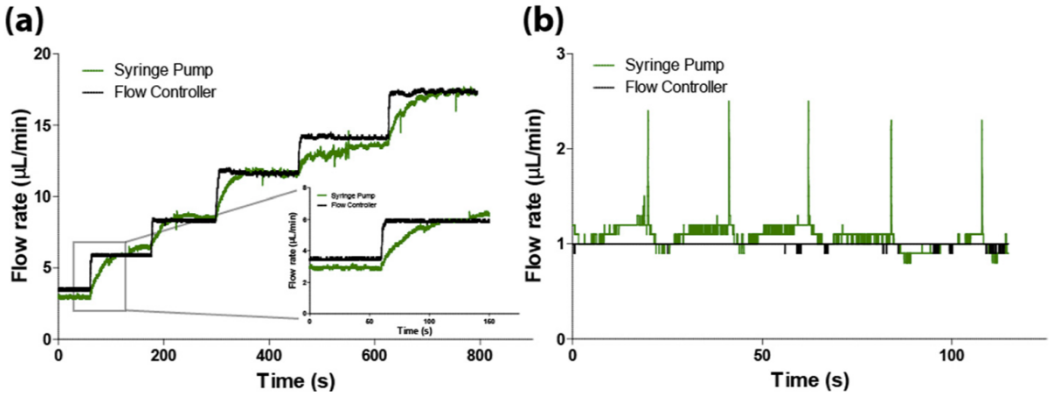

Figure 3.3. (a) Time response comparison of the presented flow controller and a commercial syringe pump. The syringe pump requires, on average, 20 s to stabilize while the flow controller requires less than five seconds. In some instances, the syringe pump requires almost 60 s, as shown in the subplot. (b) Flow rate comparison between the flow controller and syringe pump at 1 µL/min. The syringe pump exhibits pulsatile flow at low flow rates while the flow controller offers stable flow rates.

3.4.4.3 Flow switches prevent fluid back flow

For many microfluidic applications, it is not sufficient to simply control when a single flow stream is on or off. Experiments in cell biology, for example, often require the ability to vary the fluid flow rate and switch between multiple streams. To accommodate these requirements, we also developed a simple and inexpensive switching solution to make our flow system suitable for a broader range of microfluidic applications. This is an important feature because switching flows on and off using pressurized fluid vials can be initially challenging because fluid flow follows the path of least resistance in a microfluidic network. It is important to have a method to prevent fluid backflow to sample vials: when fluid from one fluid-filled vial flows into the device and then unwantedly flows back out into a neighboring vial.

Backflow occurs when a pressure difference between two microfluidic inlets exist that is large enough to drive flow from one inlet, into the device, and out into a second inlet. Backflow is typically unwanted because it can contaminate neighboring vial samples and lead to longer setup times. To alleviate this problem, we designed a novel and inexpensive flow controller switch (Figure 3.4(a)) to prevent backflow.

To test the effectiveness of the flow controller switch, we used a microfluidic T-channel device with two inlets and one single outlet, shown in Figure 3.4(b). Two fluid streams were driven into the device at equal pressures to produce co-laminar streams that flow side-by-side. To aid in flow visualization, one fluid stream was dyed with Alexa Fluor 488 (green) and the adjacent stream is dyed with Alexa Fluor 594 (red). The applied pressures for both solutions were equal, producing a fluid interface centered in the main flow channel. Each fluid line was turned on or off using the appropriate flow controller switch. When the switch connected to the red solution was turned to the "off" position no backflow occurs (Figure 3.4(c)) Instead, the red solution stops in the T-channel junction. Conversely, when the red stream is turned "on" and the green stream turned "off," the green stream stops before the junction (Figure 3.4(d)). While this is a simple application, this is an important technical ability done at a fraction of the cost of a single syringe pump. This tool is applicable to many applications including simple solution switching, chemical titrations, surface functionalization, and delivery of specific drugs, inhibitors or chemokines to downstream cells.

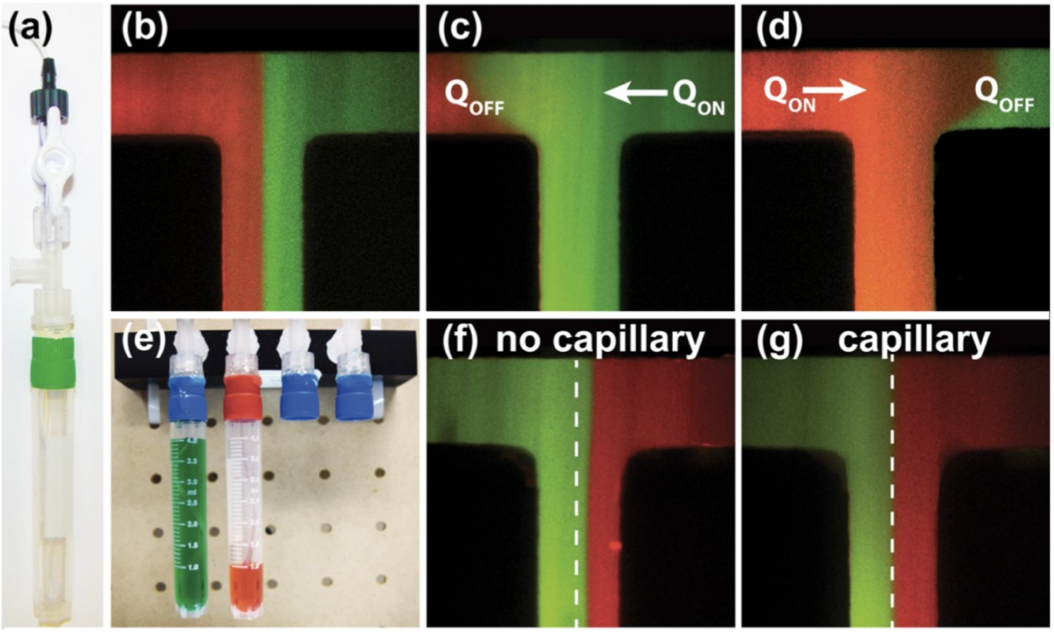

Figure 3.4. (a) Low-cost fluidic switch for fluid routing. When the switch is turned “off,” it prevents the sample from flowing backward from one cryotube and into another. (b) Two laminar liquids flow side-by-side at equal flow rates in a microfluidic T-channel. (c) The switch for the “red” stream is turned off and the “green” stream follows the path of least resistance. (d) The switching is reversed. (e) Two samples with different cryotube volumes are delivered to a microfluidic T-channel. (f) Without a capillary the hydraulic head of the “green” stream is greater than the “red,” resulting in the “green” stream having a faster flow rate and the interface is not centered. (g) When the capillary is introduced to the same system both flow rates become equal and the interface becomes centered. The effect of the hydraulic head is eliminated as the flow rate is bottlenecked at the high resistive capillary.

3.4.4.4 Flow contributions from hydrostatic pressure

In addition to backflow, it is important to note that gravitational forces can also influence the flow controller’s fluid flow behavior. During flow experiments, we observed that when cryovial fluid volumes differed, a different pressure is required to produce equal flow rates. Because the sample volume exists over a height, h, several centimeters above the microfluidic device, a hydrostatic head pressure $(\Delta P_g = \rho g h)$ exists between the top of the fluid sample and the base of the microfluidic chip. While this may appear trivial to the advanced microfluidics researcher, this feature is often overlooked by beginners and so we address how to solve this problem here. To observe this gravitational influence, we used a T-channel device with a different fluid volume loaded in each cryovial, as shown in Figure 3.4(e). Each vial was filled with a different volume of DI water, one with a volume of 4 mL dyed with Alexa Fluor 488 (green) and the other with 1 mL and dyed with Alexa Fluor 561 (red). When equal pressure was applied to both cryovials, the liquid-liquid interface is not centered in the main channel, indicating that the flow rates in each fluid inlet are not equal. This occurs because the hydrostatic pressure is greater in one cryovial, and therefore, the overall pressure driving flow is also greater. Recall Eq. (4), flow rate is dependent on both the hydrodynamic resistance and pressure. The initial pressure has two components associated with its value, the applied pressure from the flow system and gravity, leading to the following equation:

$$\frac{\Delta P}{R_h} + \frac{\rho g h}{R_h} = Q \tag{5}$$

For our flow controller with a sample volume 6 cm above the chip, $\Delta P_g =$ 0.1 psi, and is large enough to impact the fluid flow rate (Figure 3.4(f)). However, if the hydraulic circuit resistance is large relative to the chip, the gravitational contribution becomes negligible compared to the applied term ($\Delta P/R_h =$0.1 psi) and we observe no gravitational impact on fluid flow. This is illustrated in Figure 3.4(g), where a capillary was inserted upstream of each microfluidic inlet to produce perfectly centered liquid-liquid interface even when the sample volume heights were significantly different.

With the ability to regulate and control the flow rate for microfluidic devices with varying hydraulic resistance, we now demonstrate the applicability of our flow controller to regulate chemical gradients to study cell migration and to generate microfluidic water-in-oil emulsions for droplet studies.

Reprinted with permission from Biomicrofluidics[20], copyright 2016, AIP Publishing

Chapter 4

Dielectrophoretic detection of autologous blood doping

4.1 Introduction

The ability to detect forms of blood doping is crucial in the fight for clean athletic competitions. In endurance athletes, the difference between victory and defeat often hinges on superior aerobic performance; this competitive ambition often drives athletes to employ various “banned methods,” as defined by the World Anti-Doping Agency (WADA) [27]. As athletes uncover new methods of blood doping, there invariably follows a diagnostic method to detect its use[28-34]. Autologous blood transfusions (ABT), the removal and subsequent reinfusion of one’s own blood, however, remain one of the most difficult banned methods to detect.

In an effort to detect and mitigate its use, along with other banned methods, WADA introduced the Athlete Biological Passport (ABP) [35,36]. The ABP tracks an athlete's long term blood profile through a number of biomarkers; abnormal variations in this profile may be signs of blood doping, but are not definitive indicators of such[37]. Because the ABP in an indirect detection method and involves some amount of uncertainty, we desire a more direct, robust diagnostic technique.

Groups have turned to various methods to determine the presence of ABT, and to characterize the physiological changes RBCs experience in storage. There is evidence that red blood cells (RBCs) undergo physiological and biochemical changes in storage that are not mirrored in a circulating RBC population[38-43]. Removal of RBCs from nutrients in circulation begins a "starvation time," which in some studies is used interchangeably with "storage time." During starvation, plasticizers from blood bags may leach into the stored blood, and thus back into the body upon reinfusion, and is one opportunity for detection[44]. Several studies show significant changes in cell morphology, termed "lesions", the severity and irreversibility of which increase with increasing storage time[38]. Changes of this nature are responsible for a heterogeneous size distribution in the stored RBC population – more advanced storage lesions lead to vesiculation of the cell, thus decreasing its size. Decreased size of the RBCs is shown to increase the overall cell density, which has been exploited to show a spectrum of varied cell densities according to age[39]. Alterations to the cell size also inherently alters its electrophoretic behavior; Harrison et al. have shown promising results using capillary electrophoresis (CE) to separate aged RBCs based on this degradation of electrophoretic mobility[45].

Electrophoretis, and dielectrophoresis (DEP) in particular, is often used as a metric for diagnostics and separation. These spectroscopy techniques are frequently implemented for a multitude of diagnostic and quantitative assays. Many groups use this method for determining viability of yeast[46], label-free detection of bioreactions[24], and enhanced sensitivity of microfluidic biosensors[47], isolation and concentration of nucleic acids[48,49] and bacteria[50], among many other targets[51-53]. DEP theory of particles and cells is well explored; mobility and behavior is shown to be sensitive to changes in particle and cell size and structure[54-57], and is thus a potential assay to probe changes in RBC physiology induced by storage lesions, which include changes in cell interior and membrane composition.

When stored ex vivo, RBCs begin to lose a number of membrane-bound proteins[58]. This physiological change offers less surface proteins, which we aim to exploit to reveal age-based differences in dielectrophoretic spectra for stored cells compared to that of fresh RBCs. These changes to the cell structure and composition invariably lead to changes in the electrical properties and thus the crossover frequencies and DEP spectrum. Gagnon et al. have taken advantage of discrepancies in protein content of bovine red blood cells (bRBCs) by cross-linking the cells and performing dielectrophoretic (DEP) spectroscopy, which has shown significant changes in DEP behavior with increased bRBC starvation[59,60]. We use these same differences in these spectra to discern storage-related changes to human RBC morphology and composition, as a means to directly detect autologous blood doping in athletes.

Using a combination of membrane protein cross-linking and DEP spectroscopy, we demonstrate the ability to directly detect the presence of 5%, or one transfusion unit, of RBCs in fresh blood.

4.2 Materials and Methods

4.2.1 Device Fabrication

In this section we describe the methods used to prepare the blood samples and fabricate the device with which the dielectrophoretic analysis is performed. The complete electrode fabrication method has been described in detail in a previous publication[47]. Briefly, thin layers of chromium and gold are deposited onto coverglass by electron beam deposition and patterned using photolithography and wet etching techniques. The resulting electrodes are a quadrupole electrode array (Figure 4.1), which has well-defined regions of high field strength at the electrode edges, and a field minimum in the center; these distinct regions allow a greater separation of sample subpopulations. Wire connections are soldered and connected to a function generator (Agilent Technologies, Inc.) to supply the electric field. Indium tin oxide (ITO) electrodes are created using a lift-off method, in which the photoresist is applied before depositing the metal and subsequently washing with acetone to remove the photoresist and excess metal.

All experiments were performed by pipetting a small prepared droplet (~2 uL) onto the bare quadrupole. This method is adequate for characterizing the DEP spectra, but becomes less robust for the application of detecting blood reinfusions. A large majority of the droplet remains outside of the influence of the electric field, and these cells must gravity settle before they begin to feel any electrical stress. The developed testing chamber forces cells into an area within the field, where the number of cells within the testing chamber can be controlled by modifying the concentration of the prepared sample. This enables DEP quantification of the same cells across the entire spectrum. We make the quadrupole array out of ITO, which in thin films becomes transparent, allowing visual discrimination of the cell positions.

The DEP testing chamber and valve system are created using classical soft lithography techniques used to create microfluidic devices[2], and will not be discussed in depth here. Multilayer devices, such as valve systems, require additional steps[61]. The bottom flow layer is cast in a positive photoresist (SPR-

220, DOW) that produces rounded channels capable of being completely sealed off by an upper layer. The upper valve layer is cast in a negative photoresist (SU-8 3050, Microchem Corp.) at a 30 μm thickness. The flow channels are spin-coated with polydimethylsiloxane (PDMS) in a 20:1 ratio of elastomer-to-curing-agent to a thickness of 20 μm; the upper layer is poured in a 10:1 ratio. The two layers are cured at 85 °C for 15 minutes, aligned under an inverted microscope, plasma bonded, and baked for an additional 2 hours. The resulting device is plasma bonded to the electrodes and baked overnight before use.

4.2.2 Blood Sample Preparation

All solutions and buffers were prepared with 18.2 MΩ water. All studies are performed with approval from the Homewood Institutional Review Board (HIRB) after procedure overviews and informed consent forms are signed by volunteers of their own volition. After an alcohol swab, a finger stick (Owen Mumford) sample of blood is allowed to pool on the fingertip and is quantitatively collected by pipette. The sample is added to a microcentrifuge tube, and citrate phosphate dextrose (CPD) is added in a 1:8 ratio of anticoagulant-to-whole blood before storing at 4 °C in a blood bank refrigerator. For purchased blood samples: 10 mL whole blood in CPD (Zen-Bio, Inc.) are divided into aliquots upon arrival and stored at 4 °C in a blood bank refrigerator (Jewett). For all samples: 20 μL of whole blood is added to 1 mL of 1X PBS prepared from

10X PBS stock (Quality Biological). The sample is centrifuged at 2000 relative centrifugal force (rcf) to pellet the RBCs, and the supernatant is pipetted off and replaced with fresh 1X PBS. The washing procedure is repeated twice more.

After the third wash, the supernatant is again replaced with fresh 1X PBS. The appropriate volume of stock glutaraldehyde (25% w/v)(Polysciences, Inc.) is added to the fresh RBC suspension to give the desired fixative concentration, ranging from 0.15-5.0% w/v glutaraldehyde (glt). Fixation begins immediately upon addition of glutaraldehyde, and the samples are allowed to fix by gentle mixing on a shaker (ThermoFisher) for 1 hour at 22°C. Post-fixation washing steps are performed three times with 1X PBS at 6500 rcf for 5 minutes to remove residual glutaraldehyde. A final washing step is performed with a solution of 0.8-3M 6-aminohexanoic acid (AHA), a low conductivity zwitterion. AHA has been shown to reduce the range of the DEP spectrum to frequencies achievable by less sophisticated waveform generators, in addition to showing increased stability of unfixed cells compared to other low conductivity buffers[62].

RBC cell suspensions received from collaborators at San Diego State University (SDSU) arrived pre-fixed with 2.5% w/v glt according to the aforementioned protocol, and are suspended in 1X PBS. These samples are washed three times at 6500 rcf for 5 minutes before a final washing step with and resuspension in 0.8-3M AHA.

To stain the RBCs for fluorescent imaging, Vybrant, a lipophilic dye (ThermoFisher), is added to the washed cell suspension and allowed to incubate according to the vendor protocol. The cells are then washed again before performing the simulated reinfusion and fixation. Staining the RBCs before or after the fixation step results in significant loss of RBCs in subsequent washing steps. To begin staining, 5 µL of stock dye was added per 10^6 cells. The appropriate quantity of 25% glt was then added to yield the final weight percent of glt. These samples were allowed to fix for 1 hour at 22 °C. Post-fixation washing steps in this case are performed at 2000 rcf for 5 minutes.

4.2.3 Dielectrophoretic Analysis

Cells and shelled particles are shown to exhibit multiple DEP regimes[63-66]. Plotting the defined Claussius-Mossotti (CM) factor:

$$K(\omega) = \frac{\varepsilon_{\text{eff}}^{*} - \varepsilon_{\text{m}}^{*}}{\varepsilon_{\text{eff}}^{*} - 2\varepsilon_{\text{m}}^{*}}, \tag{1}$$

where $\varepsilon_{\text{eff}}^{*}$ is defined as the effective complex permittivity for a cell containing cytoplasm and membrane regimes

$$\varepsilon_{\text{eff}}^{*} = \varepsilon_{\text{mem}}^{*} \frac{\left(\frac{r_2}{r_1}\right)^3 + 2\frac{\varepsilon_{\text{cyto}}^{*} - \varepsilon_{\text{mem}}^{*}}{\varepsilon_{\text{cyto}}^{*} - 2\varepsilon_{\text{mem}}^{*}}}{\left(\frac{r_2}{r_1}\right)^3 - \frac{\varepsilon_{\text{cyto}}^{*} - \varepsilon_{\text{mem}}^{*}}{\varepsilon_{\text{cyto}}^{*} - 2\varepsilon_{\text{mem}}^{*}}} \tag{2}$$

for a model cell whose characteristic electrical properties are assumed to be: [σ_m = 32 µS/cm, ε_m = 110; σ_{mem} = <100 mS/cm, ε_{mem} = 3.8; σ_{cyto} = 4.3mS/cm, ε_{cyto} = 60]

[1], yields three distinct regions of relative polarizability that are sensitive to disturbances in the electrical properties that govern each regime. Because our suspending buffer, AHA, has a low relative conductivity and a high permittivity, an electrical mismatch is produced at the edge of the cell membrane, driving charge accumulation at this interface. At relatively low frequencies (< 200 kHz), the electrical stress produced drives the cell to regions of lowest field strength, termed negative DEP (nDEP). Because the mechanism producing this conductive polarization requires physical migration of free ions, it is inherently frequency dependent. When the frequency increases such that the ions cannot electromigrate quickly enough to accumulate, they relax at what is known as their characteristic relaxation time scale, defined as $\tau = [(\varepsilon_2+\varepsilon_1)/(\sigma_2+\sigma_1)]$ at each interface. In cells, this relaxation often results in a change of sign in relative polarization, producing a physical crossover frequency (cof) at which the cells cross over from regions of low field strength (nDEP) to regions of high field strength, or positive DEP (pDEP) (Figures 4.1(a) & 4.2(a)). As the field penetrates into the cytoplasm, the conductive charging mechanism begins anew; because we choose a buffer with a high permittivity, the relaxation timescale of the cell interior produces a second cof that drives the cells back to nDEP (Figures 4.1(b) & 4.2(b)).

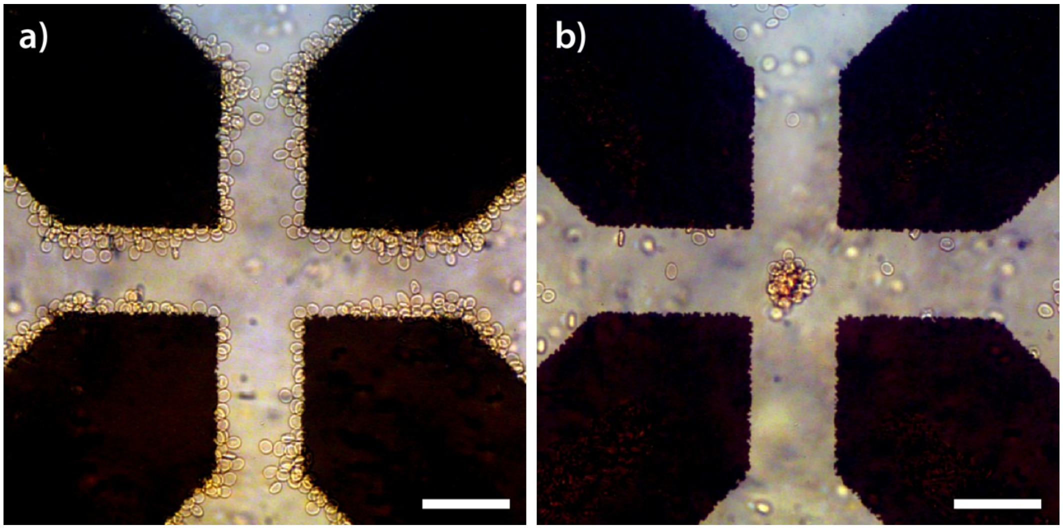

Figure 4.1. Micrographs of red blood cell DEP on a quadrupole electrode array. (a) RBCs at low frequencies are drawn to regions of high field strength (pDEP). (b) At high frequencies, RBCs cross over to regions of low field strength (nDEP). Scale bars 50 µm.

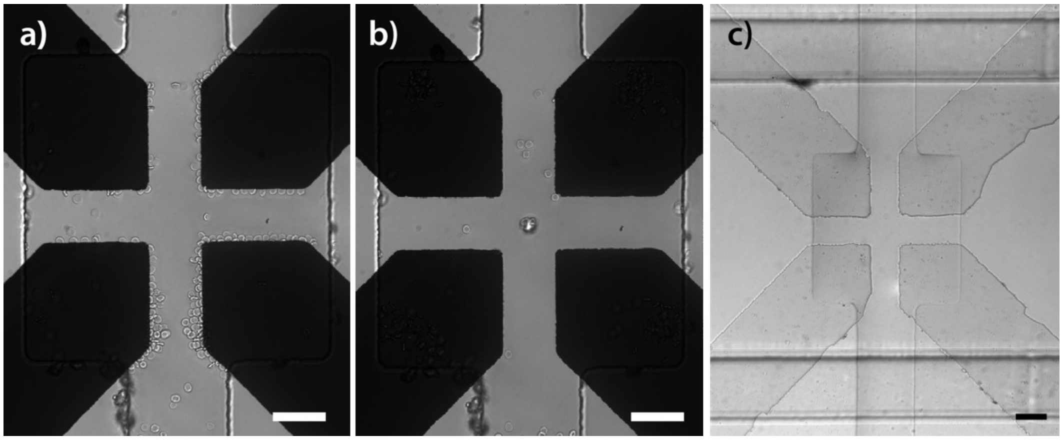

Figure 4.2. Isolated DEP microfluidic testing chamber. (a) RBCs showing pDEP inside the testing chamber at low AC field frequency. (b) RBCs showing nDEP inside the testing chamber at high AC field frequency. (c) Multi-layer microfluidic testing chamber with valves intersecting main flow channel on either side of the testing chamber. Integration of transparent ITO electrodes allows visual tracking of all cells within the confines of the chamber. Scale bars 50 µm.

Characterization of the DEP spectrum and analysis of the mixed blood samples are performed with the previously mentioned quadrupole electrode array. Approximately 2 μL of the fixed blood suspension are pipetted onto the electrode array, and an AC field is driven through the droplet by a function generator (Agilent Technologies). The frequency is slowly increased from 50 kHz to 10 MHz, and the beginning and end of the two crossover frequencies is recorded. The crossover frequency is sensitive to changes in the electrical properties, which are in turn sensitive to changes in age and storage time. These changes are tracked and used to determine the presence of stored RBCs in a fresh blood cell population.

In the valve system, a droplet of prepared blood is pipetted onto the inlet port and drawn into the testing chamber by applying vacuum to the outlet. The valve channels are dead-end filled with water and subsequently pressurized to 20-30 psi to instantaneously halt the flow of the sample and isolate the testing chamber. Once the DEP characterization is complete, the valves are released and the testing chamber is flushed with water and loaded with a new sample (Figure 4.2(c)).

4.3. Results and Discussion

4.3.1 Characterization of the DEP Spectrum

To determine the optimal degree of fixation required to maximize resolution, and thus separation between storage times, we sample stored aliquots of purchased whole blood as they age over a period of 4-6 weeks. During this time, the cells undergo a starvation process that alters the protein content of the membrane and interior, providing fewer sites for fixation. The fixation is performed over a range of 0.15-2.5% w/v glt, and the second cof, or high cof, is measured. In this work, we investigate only the high cof, as this is where we have seen the greatest measureable change with time, and the low cof is often lowered to frequencies that result in Faradaic reactions on the electrode surfaces (< 40 kHz). The beginning of the cof is marked when the first cells cross over into the field minimum in the center. The frequency is increased until all cells have been removed from the high field regions – this is the end frequency of the cof. The cof is reported as the average of these two values and plotted as functions of storage time as well as weight percentage of glt.

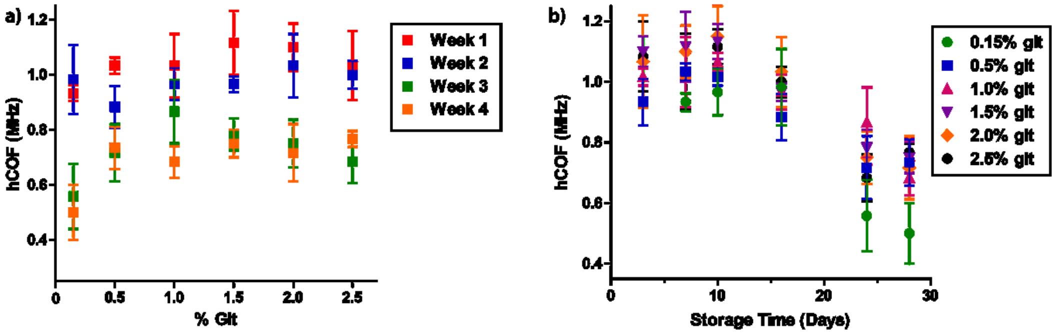

Figure 4.3. Effects of fixation and storage time on RBC crossover. (a) Increasing % glt increases the degree of fixation of proteins in the cells and increases hCOF. Increased storage time is known

to deplete RBC proteins, leaving fewer proteins available for fixation and decreasing the hCOF. (b) All percentages of glt collapse to a single dominating trend of decreased hCOF with storage time.

We observe that the cof decreases with increasing storage time for all weight percentages of glt. Increasing degree of fixation within the cell slightly increases the cof but does not appear to increase or significantly optimize the resolution between week 1 and week 4 of storage (Figure 4.3). Unless otherwise specified, all subsequent experiments are performed at 2.5% w/v glt.

4.3.2 Volunteer Samples

For volunteers, all personal data identifiers are rendered anonymous for publications., we collected fingerprick samples from graduate student volunteers once a week for 6 weeks. After the last sample collection, simulated reinfusion samples are created, and all aliquots are prepared for testing and undergo DEP spectroscopy (Figure 4.4). In this case, we see decreased resolution between storage times, compared to the DEP spectroscopy results from purchased vials of blood (Figure 4.3(b)). We hypothesize that discrepancies in the aliquot sizes may be a significant factor. Cell starvation in this decreased fingerstick sample volume is likely quite different from a 1 mL aliquot as well as a full blood bag, and thus further studies must be done with more relevant sample volumes.

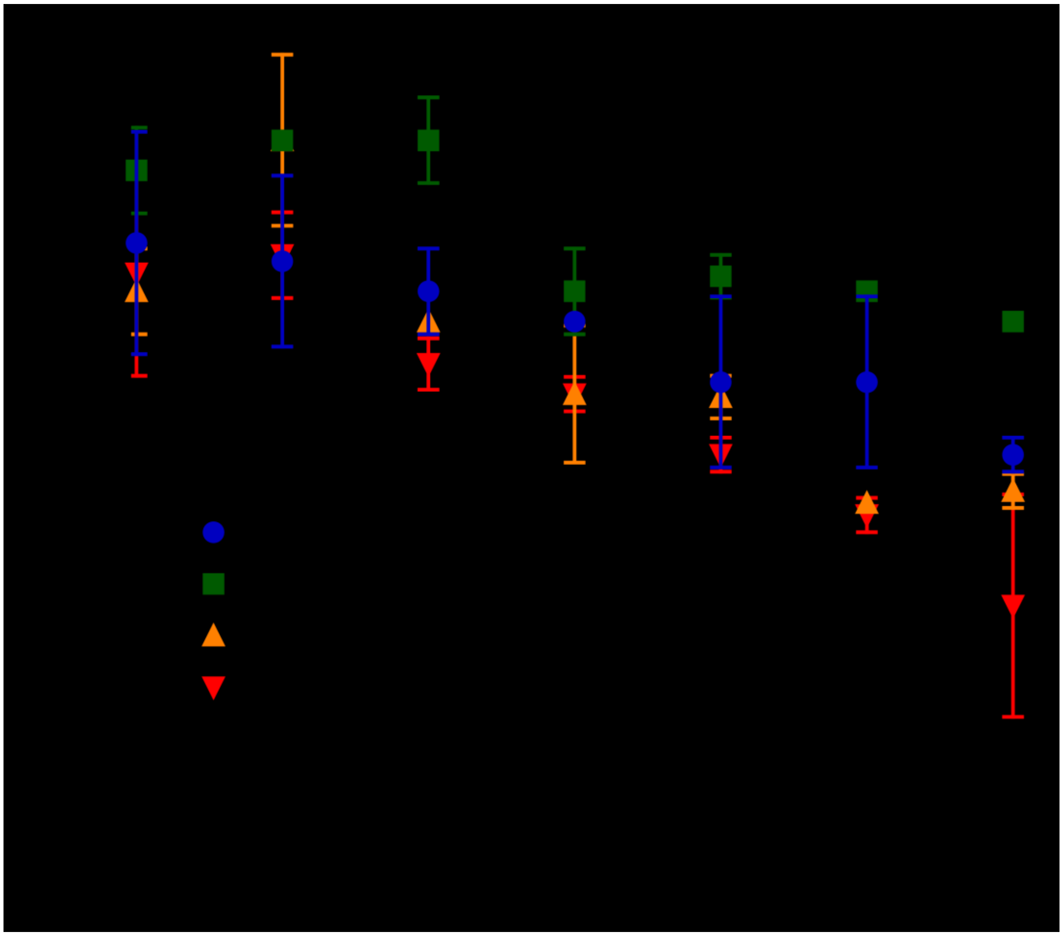

Figure 4.4. DEP of grad volunteer samples. The same trend is observed as for vendor-supplied blood. We note that the overall decrease in hCOF is dimished here compared to vendor samples, which we attribute to large discrepancies in aliquot size between these sources.

To create a robust assay for use in athletic settings, we try to eliminate or reduce the possibility of false positives, and deduce whether exercise itself alters the DEP spectrum. From SDSU collaborators, we received blood samples from cyclists before and after a 5-hour bike ride, and label the samples pre (A) and post (B) exercise. The breakdown of the group and individual cof's are shown in

Figures 4.5 & 4.6. In Figures 4.5(a) & 4.6(a), the breakdowns are shown by average overall cof. In Figures 4.5(b) & 4.6(b), the lower and upper bars represent the lowest frequency at which the cells begin to crossover, and the highest frequency at which the cells finish crossing over, respectively. The lower and upper boundaries of the box represent the average frequency at which cells begin to cross over, and the average frequency at which the cells finish crossing over, respectively. The midline of the box is the overall averaged cof. In all representations of the data, we conclude that the spectra remain significantly unchanged, and that exercise does not seem to shift the spectra, although further sampling is required to increase the reliability of the assay to 99.9%.

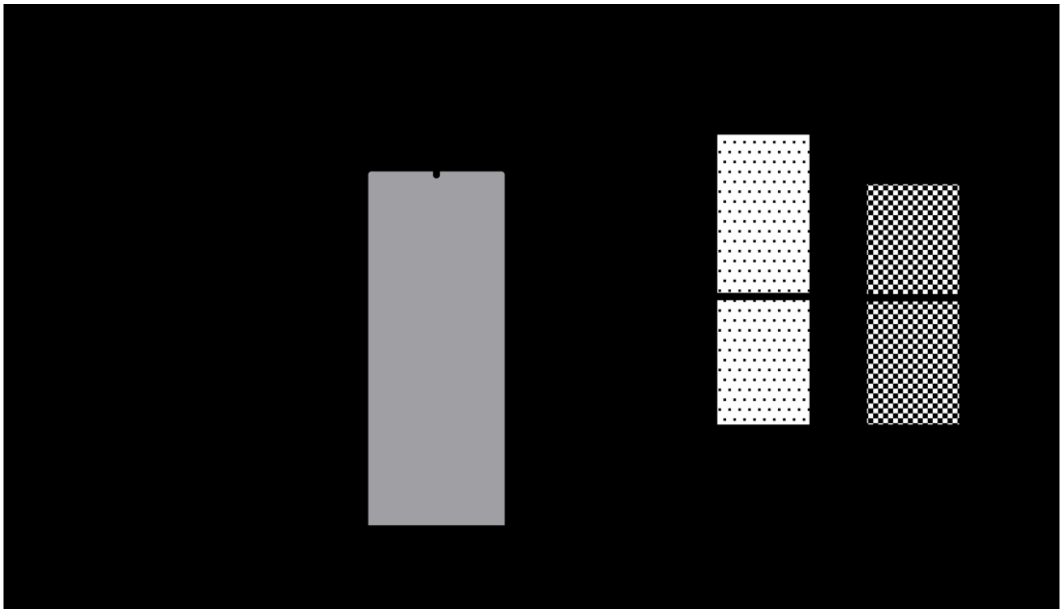

Figure 4.5. Effects of exercise on athlete COF. (a) The average COF is plotted for the whole group before ($A_{Grouped}$) a 5-hour cycling session, and after ($B_{Grouped}$). (b) A more complex breakdown of the grouped COFs. The lower bound of the box marks the beginning of the cells crossing over, and

the upper bound marks the end of the cells crossing over. The midline of the box is the average of this spectrum.

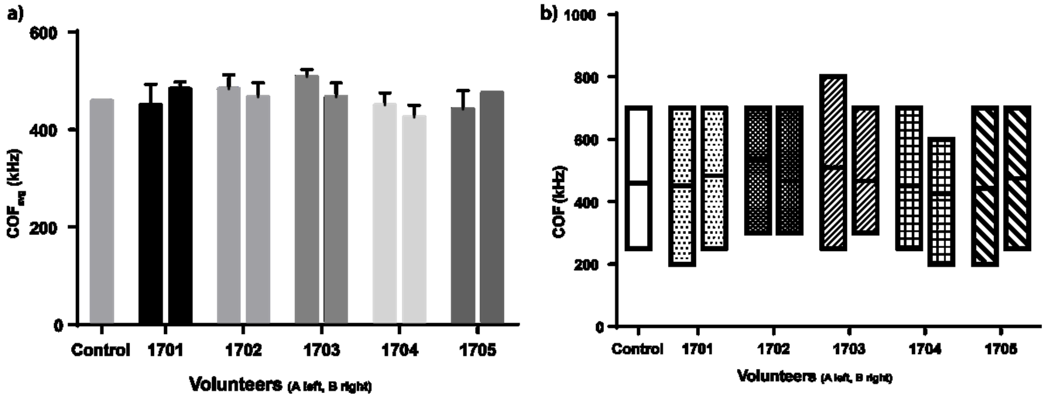

Figure 4.6. Individual effects of exercise on athlete COF. (a) Individual COF_{avg} is plotted before and after the 5-hour cycling session, displayed side-by-side for each athlete, where the control is a non-athlete. (b) Complex breakdown of individual COFs plotted side-by-side for each athlete before and after the 5-hour cycling session.

4.3.3 *In Vitro* Autologous Reinfusion

We perform a simulated reinfusion of 1 unit of stored blood, which will account for approximately 5% of the total blood volume. To separate the subpopulations, we apply a frequency between 0.7-1.0 MHz, where fresh cells still experience pDEP (Figure 4.7(a)) but the same cells at 4 weeks of storage time have already crossed over (Figure 4.7(b)). In the reinfusion, the presence of cells in the field minimum is indicative of reinfused cells whose cof has dropped with storage time and have crossed over earlier than the fresh population. We verify this by performing the same reinfusion with stained cells. Fresh cells are stained red, and stored cells are stained green prior to reinfusing and fixation (Figure

4.7(c)). While this experiment is not fully representative of the complex physiological processes undergone during an autologous transfusion, the ability to electrically detect differences in cell age and composition is a crucial step in the development of a robust detection assay.

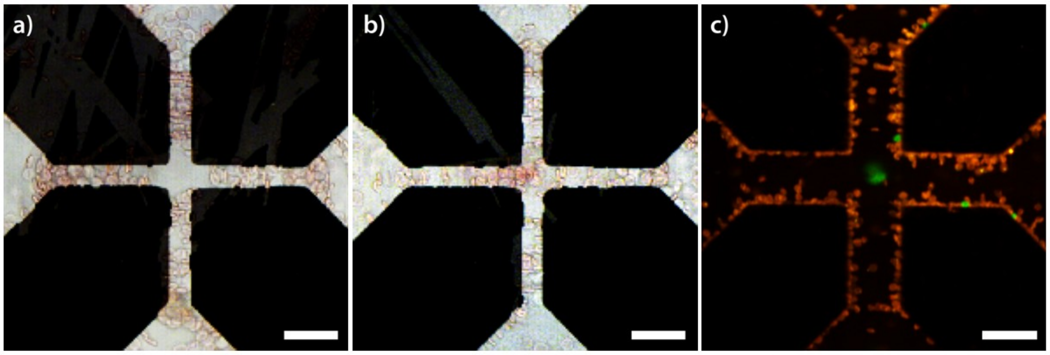

Figure 4.7. Visualization of a simulated reinfusion and fluorescent confirmation of detection. (a) A fresh (Day 1) blood sample under AC field at 800 kHz. Fresh cells exhibit pDEP exclusively. (b) Simulated reinfusion of 5% Day 28 blood in 95% Day 1 blood under AC field at 800 kHz. The presence of cells in the center (low field region) presenting nDEP is suggestive of "doping." (c) Fluorescent microscopy confirms detection. Fresh cells are stained red and show pDEP, while 4-week cells are stained green and exhibit nDEP. Scale bars 50 µm.

4.3.4 *In vivo* Autologous Transfusion

In this study, a group of 3 cyclists underwent true autologous blood transfusions of one pint of blood. Athletes are given anonymous data identifiers $AT_{1\text{-}3}$. Blood samples for testing were taken immediately prior to reinfusion (D_{PRE}), immediately after reinfusion (D_0), and intermittent days 1-6 days after reinfusion ($D_{1, 2, \ldots, 6}$). We observe an immediate drop in COF_{avg} post transfusion for all athletes, and a further decrease of COF_{avg} for samples taken at least 2 days post transfusion. It is interesting to note that individual cells from the reinfused subpopulation were not trapped at frequencies below the baseline COF, as was observed in the *in vitro* transfusions. Instead, the process of an autologous transfusion appears to affect the entire circulating blood population, lowering the COF_{avg} compared to its pre-transfusion baseline (Figure 4.8). Figure 4.9 provides a more complex breakdown of the decreasing COF for each athlete. We further illustrate this lowering of the COF_{avg} by comparing micrographs of the athletes AT_1 (Figure 4.10) and AT_3 (Figure 4.11) over the time before and after reinfusion, where all images are held at the same applied frequency. The presence of cells in the low field region, in additional to pearl-chaining RBC between the electrode gaps, is evidence of a lowered COF, and is shown as a steady decrease particularly for athlete AT_3.

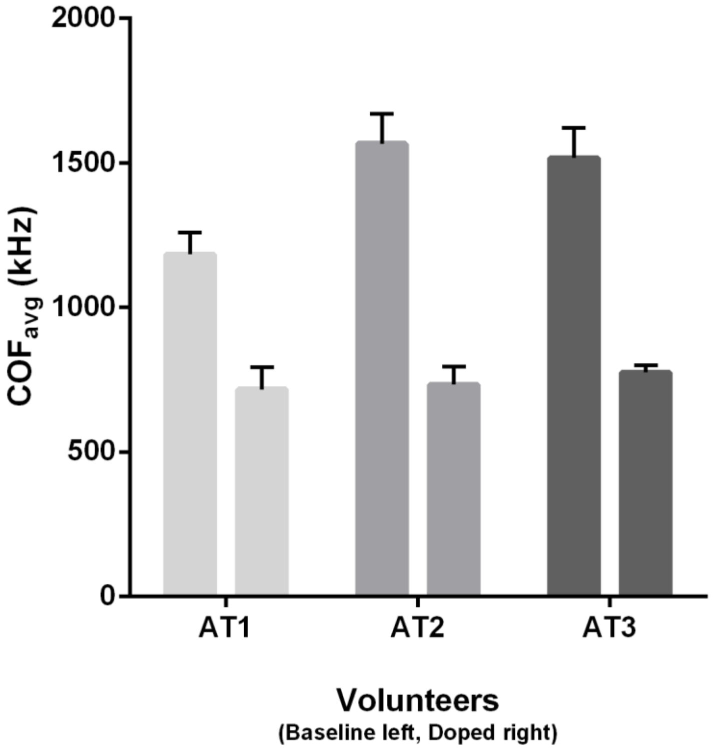

Figure 4.8. Effects of autologous blood transfusion on COF. Three athletes having undergone a one-unit autologous transfusion display a significant decrease in the COF of the whole blood population. Doped COF values here were selected from the days after transfusion that displayed the lowest measured COF for each athlete.

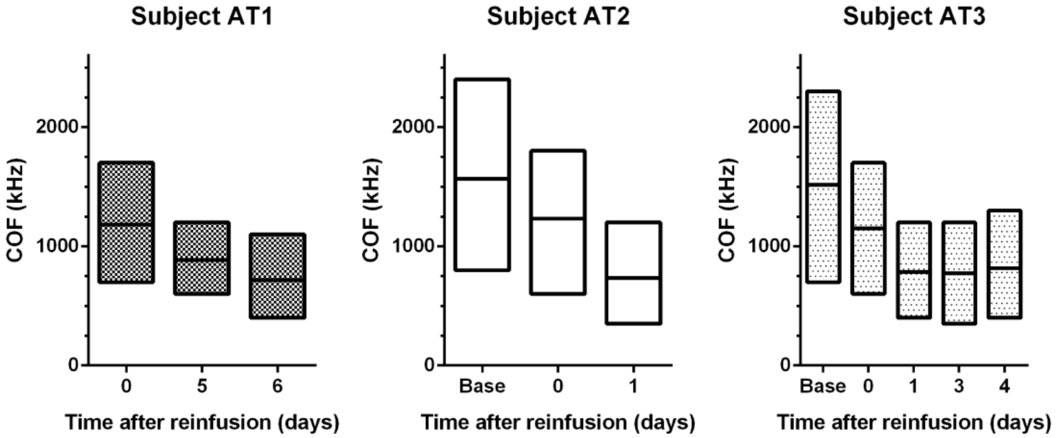

Figure 4.9. Complex breakdown of the effects of autologous blood transfusion on COF. Athlete COFs decrease slightly after reinfusion, and continue to decrease in the week following. A baseline sample was not provided for subject AT1.

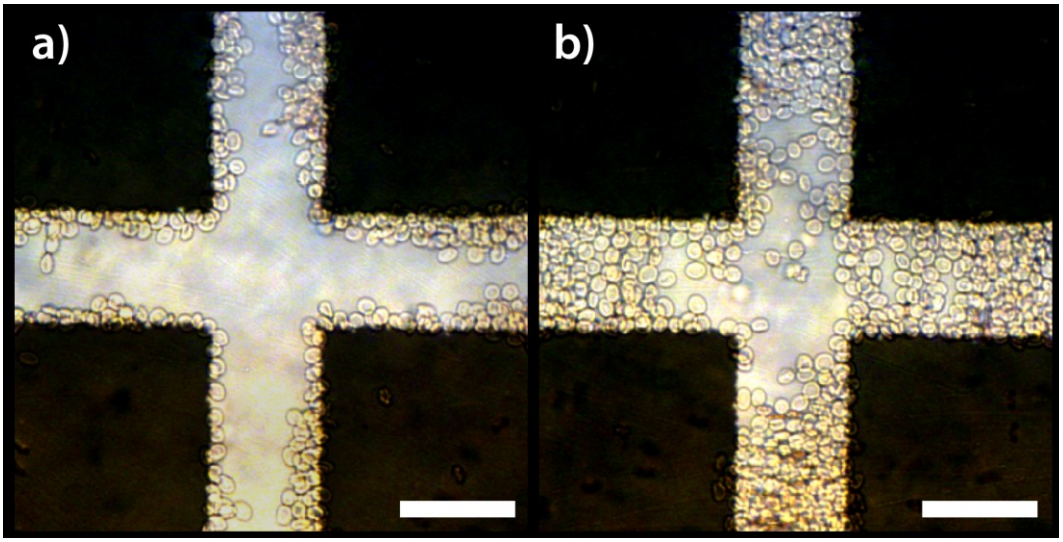

Figure 4.10. Illustration of decreased COF in subject AT1. (a) Immediately after transfusion (D_0) at 0.4 MHz. (b) 6 days after reinfusion (D_6) at 0.4 MHz. The presence of cells crossed over and pearl chaining between the electrode gaps are indication of decreased COF. Scale bars 50 µm.

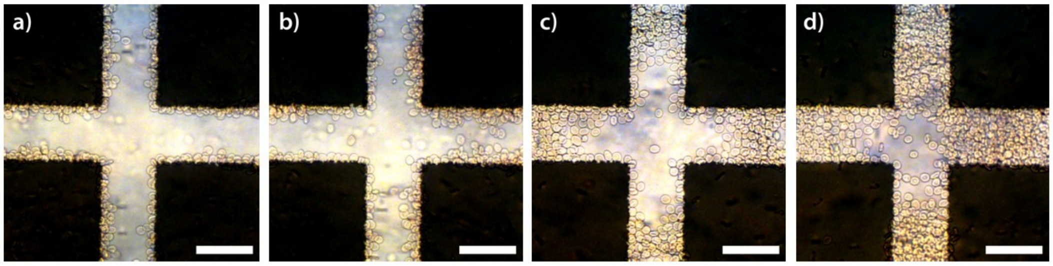

Figure 4.11. Illustration of decreased COF in subject AT3. (a) Prior to reinfusion (D_{base}) at 0.4 MHz. (b) Immediately after reinfusion (D_0) at 0.4 MHz. (c) 1 day post reinfusion (D_1) at 0.4 MHz. (d) 3 days post reinfusion (D_3) at 0.4 MHz. Scale bars 50 µm.

4.4 Conclusions

We have shown the ability to detect changes in the DEP spectra of fresh and aging blood populations, and the ability to separate these mixed populations in an *in vitro* simulated reinfusion of 1 unit of blood. Cell starvation produced storage lesions that resulted in changes to the cell composition, which we were able to detect with DEP spectroscopy. We were able to use these differences to probe a mixed blood population and visibly separate the reinfused subpopulation from the fresh sample. We have also shown the ability to detect the presence of a true *in vivo* autologous transfusion, though this assay must be tested further to increase its detection capabilities to the requisite 99.9% accuracy. This can be obtained, along with complete objectivity and confidence of measurements, by application of an automated DEP platform (3DEP, Labtech International Ltd.) [67,68]. With an automated system, this DEP assay can used either as an invaluable addition to WADA's ABP or as a standalone test for other sporting entities.

Chapter 5

Real-time deformability cytometry (RTDC) for detection of autologous blood doping

5.1 Introduction

The intensely competitive nature of endurance sports drives athletes to great lengths in order to secure victory. When conditioning isn't enough, athletes turn to artificial means of enhancing their aerobic performance, utilizing a variety of blood transfusions in an attempt to edge out their competitors. These methods are banned not only by domestic entities like the U.S. Anti-Doping Agency (USADA) [69], but by a number of international organizations, including the World Anti-Doping Agency (WADA) [27] and the International Olympic Committee (IOC) [70]. Advancing our ability to detect these methods is crucial, as they remain some of the most difficult doping methods to detect.

Autologous blood transfusions (ABT), the donation and storage of one's own blood for later reinfusion, is currently the most sophisticated method of blood doping. This method is typically practiced by hospitals and the military for patients undergoing surgery and in the event of traumatic blood loss[71-75], however, athletes have adopted ABTs in an effort to enhance their oxygen carrying capacity and remain undetected by doping agencies.

Refrigerated blood bags under proper storage conditions are shown to be viable for reinfusion up to 35 days, as approved by the FDA[76]. For blood frozen in glycerol, the viability extends past 10 years[77,78]. Given that 4-6 weeks are required to recover hemoglobin mass after a 1-unit donation[79], autologous blood must be stored at least this long for an athlete to expect full therapeutic effects. There is evidence that blood cells stored for these periods of time undergo irreversible changes to their physiology and morphology[38]. Some of these changes may be reversible upon reinfusion, but increasing storage times are linked to an increasing population of irreversibly changed cells, greatly increasing the risk of local hypoxia, stroke, and multiple organ failure[80,81]. While there seem to be little to no changes in RBC morphology and physiology by cryopreservation in glycerol, excluding possible hemolysis during freeze and thaw processes, there is a correlation of dangerous side effects associated with transfusions of this nature – improper deglycerolization of a frozen unit presents the risk for sepsis and renal failure[82].

With the risks presented, athletes continue to practice blood transfusions as a means enhance aerobic performance. The Athlete Biological Passport (ABP) [35,36], first adopted by the Union Cycliste Internationale (UCI) and subsequently by most other sports organizations, including WADA, is the current paradigm for anti-doping drug testing. This long-term tracking of hematological biomarkers is meant to preserve a record of an athlete's blood profile, and use deviations as indicators for potential doping. This multifaceted approach is evolving and largely effective but relies on a compilation of indirect markers and subjective interpretation of data and would benefit from the addition of a direct detection assay.

Microfluidics presents a real-time solution to many bioanalytical assays, and is utilized for detection of biomolecular binding[24,47], DNA hybridization[83,84], and single cells studies[85-87]. The continuous flow nature of microfluidic devices makes them ideal for biodetection applications, where fouling of solid, stationary substrates found in traditional biosensors is often an issue. Microfluidics has also been used as a platform for shear-induced RBC deformation studies[88-90]. But age-related studies using this platform remains largely uninvestigated.

Otto et al recently used microfluidics as a means of mechanically probing the viscoelasticity of polymer spheres and cells[89]. Utilizing a microfluidic constriction, the cells are subjected to shear forces that deform the cells to a degree that is dependent on their cytoskeletal structure and viscoelastic properties.

With the use of a high-speed camera and proprietary software, the cells can be imaged inside of the constriction and their deformation extracted in real time. We have applied the same mechanical principle to the deformation of red blood cells, in an attempt to determine differences in storage time by probing their deformability. The deformability of RBCs is known to decrease in external storage conditions, as shown by Berezina et al in micropore filtration experiments[38]. We anticipate that stored cells will present with less elasticity and a lower degree of deformation that can be analyzed by direct measurements of the cells as they actively squeeze through a microfluidic constriction, as opposed to their fresh, circulating counterparts.

5.2 Materials and Methods

5.2.1 Device Fabrication

Microfluidic devices are created using standard photolithography and soft lithography techniques, which are detailed elsewhere. Briefly, negative photoresist (SU-8, MicroChem Corp) is spun onto a 4-inch wafer (University Wafer) after dehydration baking and is exposed to a UV source (KLOÉ) to produce a master mold. The elastomer polydimethylsiloxane (PDMS) is mixed in a 10:1 elastomer-to-curing-agent ratio and poured over the wafer. After curing at 85 °C for 15 minutes, the PDMS is peeled and cut. Fluid ports are created with a biopsy punch (Ted Pella, Inc.), the PDMS is plasma bonded to coverglass (no 1, ThermoFisher) to create microchannels. Fluid is delivered to the device via syringe pump (KD Scientific) at a constant flow rate of 0.75 μL/min, unless otherwise specified.

5.2.2 Blood Sample Preparation

All solutions are made with 18 MΩ deionized water. With Institutional Review Board (IRB) approval and informed consent, finger prick blood samples were collected from volunteers with fingertip lancets (Owen Mumford) and stored in citrate phosphate dextrose (CPD)(Sigma Aldrich) in a ratio of 1:8 anticoagulant-to-whole-blood. All blood samples and aliquots are stored at 4 °C in a blood bank refrigerator (Jewett). Where otherwise specified, blood is sourced from a single vendor (Zen-Bio) and aliquoted in volumes of 0.5–1.0 mL before storing in the blood bank refrigerator. For non-human mammalian (herein refered to as "animal") samples, bovine (cow), ovine (sheep), caprine (goat), and equine (horse) blood was purchased from Quad Five with citrate anticoagulant and aliquoted in volumes of 0.5-1.0 mL on arrival and stored in a blood bank refrigerator.

To prepare for RTDC, a small volume of blood is removed from an aliquot and diluted in 1X PBS. The diluted blood is washed in a centrifuge (Microfuge 18, Beckman Coulter) for 2 minutes at 2000 rcf. The supernatant is removed and the pellet is resuspended in fresh 1X PBS. After the third removal, the pellet is resuspended in 1X PBS with 0.5% wt methylcellulose (mc) (M0512, Sigma Aldrich), unless otherwise specified. The final resuspension must achieve a ratio of 1:50 whole-blood-to-buffer, determined by the initial whole blood volume removed from the aliquot.

5.2.3 Real-Time Deformability Cytometry

RTDC utilizes a combination of microfluidic sheath flow and hydrodynamic shear stress to flow focus a stream of RBCs into a narrowed channel (Figure 5.1). The strong velocity gradient within the constriction produces high shear rates at cell edges nearest the walls, deforming the cells without making contact with the channel walls. This greatly reduces clogging, which is observed in approximately 10-15% of devices.

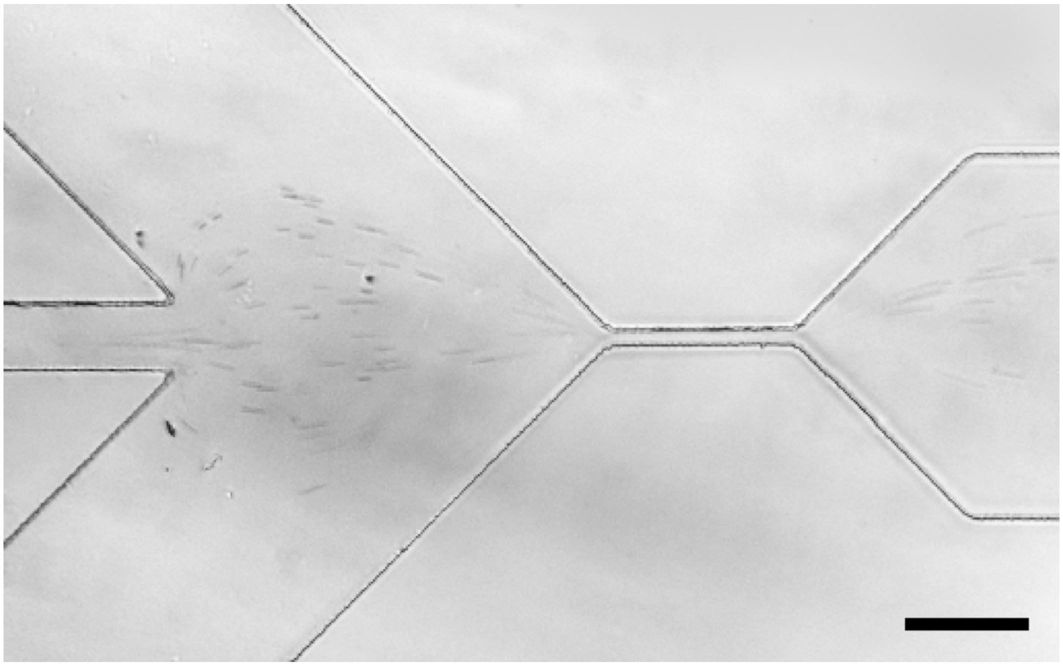

Figure 5.1. Brightfield view of RTDC microfluidic device. Cells are centered by the sheathing side streams and funneled into the constriction where they are imaged by a high-speed camera. Scale bar 200 µm.

Flow behavior in the area of interest, the microfluidic constriction, is simplified to be described using the classical fluid transport problem of flow around a sphere, the analytical solution for which is derived using stream functions and presented as[91]:

$$\Psi(r,\theta) = \sum_{n=2}^{\infty} \frac{P_{n-2}(\cos\theta) - P_n(\cos\theta)}{2n-1} \times \left(A_n r^n + B_n r^{-n+1} + C_n r^{n+2} + D_n r^{-n+3}\right) \tag{1}$$

with Legendre polynomials (P_n) and constants $(A_n - D_n)$ determined from no slip and far-field boundary conditions.

From Equation 1 we observe that hydrodynamic shear forces are maximized at $\theta = \pi/2$, or at the cells edges closest to the channel walls.

The above theory does not fully describe the demonstrated phenomena. Highly deformable cells being advected into the microfluidic channel present a complex analytical problem beyond a simple stream function. Mietke et al have developed a full analytical model for the flow field around a viscoelastic sphere advected in a microfluidic channel[91].

The constriction is designed and fabricated such that the average size of the cell is 50-90% of the channel size, providing high shear rates and deformations that are visually observable and quantifiable. Microfluidic sheathing into the constriction centers RBCs as they advect through the channel at speeds on the order of 5-10 cm/s, which beyond the imaging capability of most standard microscope mounted cameras. The use of a high-speed camera (Fastec Imaging) allows capture of 10^2–10^3 cells in a single video encompassing approximately 7 seconds at a capture rate of 5100 frames/sec (fps).

$$D = 1 - \frac{2\sqrt{\pi A}}{P} \tag{2}$$

The projected area *(A)* and cell perimeter (P) are measured and used to calculate the circularity $c = \left(2\sqrt{\pi A}\right)/P$. Deformation *(D)* is then quantified as deviation from a perfect circle.

5.3 Results and Discussions

5.3.1 Buffer Optimization and Device Calibration

The imaging challenges associated with accelerating cells through a constriction on the order of 10 cm/s necessitate the use of a high-speed camera, for now. To optimize the detection assay, we hold the flow rate constant and instead vary the viscosity of the suspending buffer, increasing the stress without impeding the ability to effectively image the cell speeding through the constriction. We vary the 1X PBS buffer from 0-1.0% mc, 0.2 um filtering the buffer before use. The degree of deformation is dependent on the hydrodynamic shear forces of the constriction acting on the cell, which can be modulated by changing the medium viscosity; optimizing this force is crucial to the resolution of the measurements. Insufficient shear will not act on the fresh cells enough to fully express their inherent deformability; excessive stress will over-shear both fresh and aged cells to the extent that they become indistinguishable.

From Figure 5.2, we see that for methylcellulose content lower than 0.75% mc, there are apparent differences in deformation, which may be differentiable but are not maximized. For content greater than 0.85% mc, the apparent differences begin to diminish, due to the increased deformation of the aged cells as a direct result of the increased viscosity and thus shear force. The shear forces are therefore optimized for a range of methylcellulose from 0.35-0.5% mc. This corresponds to a viscosity range of approximately 5-15 centipoise (cP). We run all subsequent experiments at 0.5% mc, corresponding to a buffer viscosity of 15 cP.

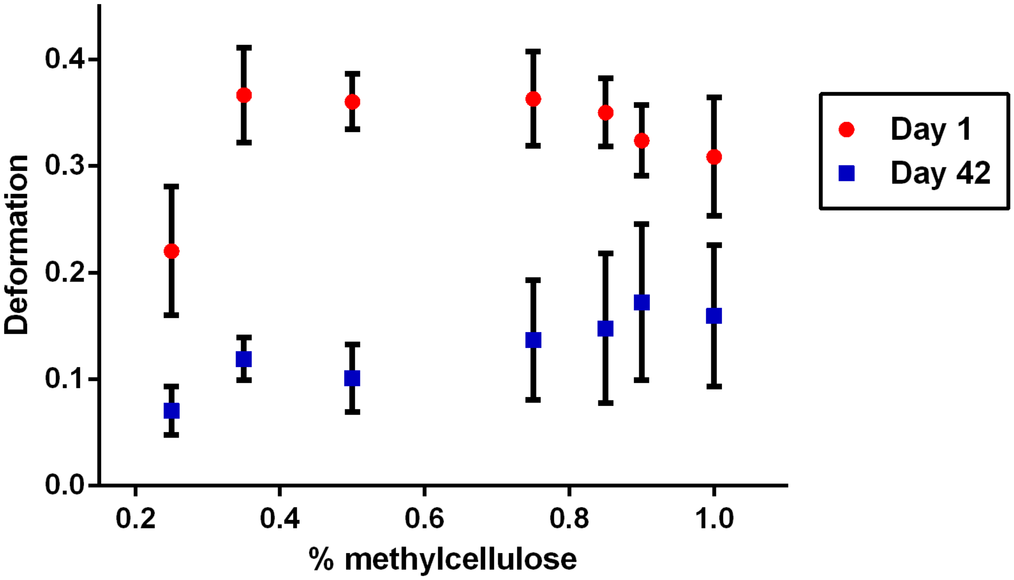

Figure 5.2. Optimization of the viscous cell medium. Increasing the viscosity of the buffer enhances differences between fresh and aged blood to an extent – increasingly viscous buffer (> 0.75% mc) begins to lose resolution between the populations.

Vesiculation under storage conditions reduces the overall size of the cell[43]; because this process is irreversible, size is a popular metric to ascertain the state of aged and reinfused cells[45]. In the interest of developing a robust assay for detecting subtle changes specifically in RBCs, we opt to calibrate our sensor with RBCs of several different non-human mammals. The distribution of cell size and deformation should differentiate into visually distinguishable populations, regardless of the inherent size distribution within each mammal. The average sizes for each mammal are given as such in Table 5.1:

Table 5.1. Average cell size and deformation from non-human mammalian sources.

Blood source:	**Average cell diameter (µm):**	**Average deformation:**
Cow	4.5 ± 1.93	0.357 ± 0.053
Goat	4.11 ± 1.87	0.290 ± 0.045
Sheep	3.90 ± 1.87	0.067 ± 0.027
Horse	4.75 ± 2.13	0.195 ± 0.039

With 400+ cells analyzed, the clustering of the species cells is observable in Figure 5.3. An ANOVA analysis confirms this separation ($P < 0.0001$, $R^2 = 0.8686$). Given that the average size deviations of these mammals from humans ranges from 1 – 5 µm, their separation is a good indicator of RTDC as a sensitive means to mechanically probe visually indiscernible differences in cell size and composition, and thus to detect reinfused RBCs.

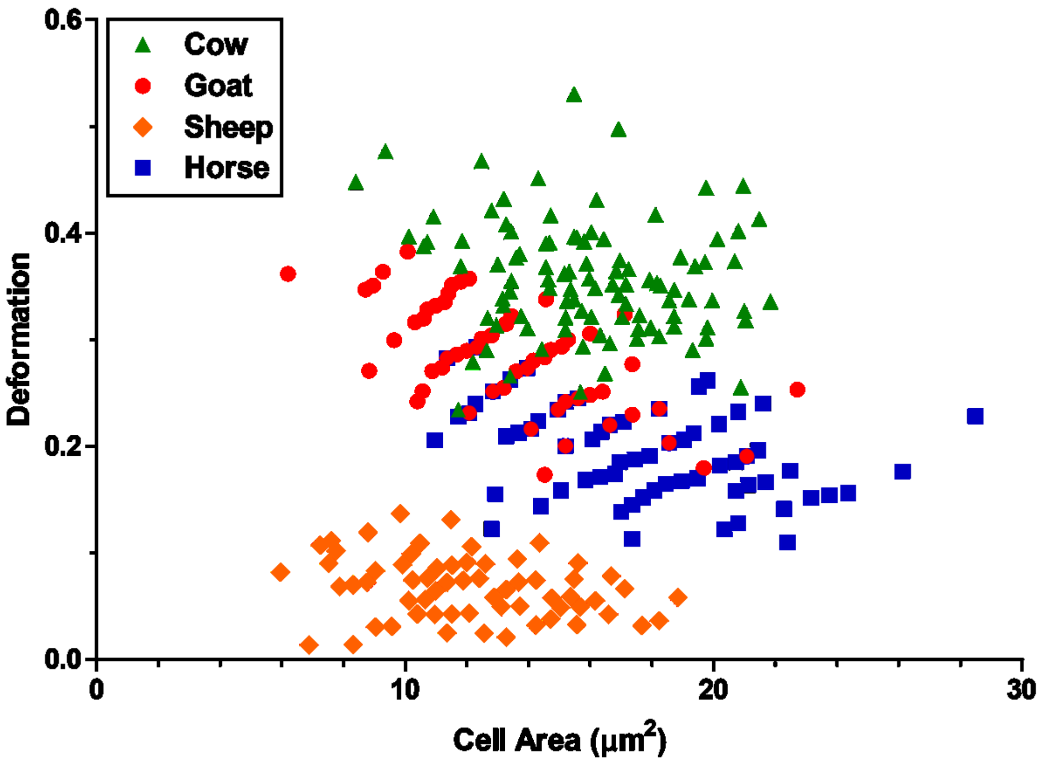

Figure 5.3. Deformability analysis of non-human mammalian RBCs. For four different species, four groupings can be seen and statistically verified.

5.3.2 RBC Deformability with Increasing Storage Time

To determine the presence of aged cells, the deformability spectrum must be characterized over the duration of the storage period. The deformability spectrum shown in Figure 5.4 is observed to decrease with age, rapidly over the first 4 weeks, and more slowly over the remaining 2 weeks. While the initial decrease is observable and distinguishable, the likelihood of recovering reinfused cells from this time period may be hindered, as the percentage of irreversibly changed cells is quite low. With increasing storage time, however, this population increases; by extension, late-stage reinfusions, with their irreversibly diminished size and cytoskeletal content, should be the easiest to detect.

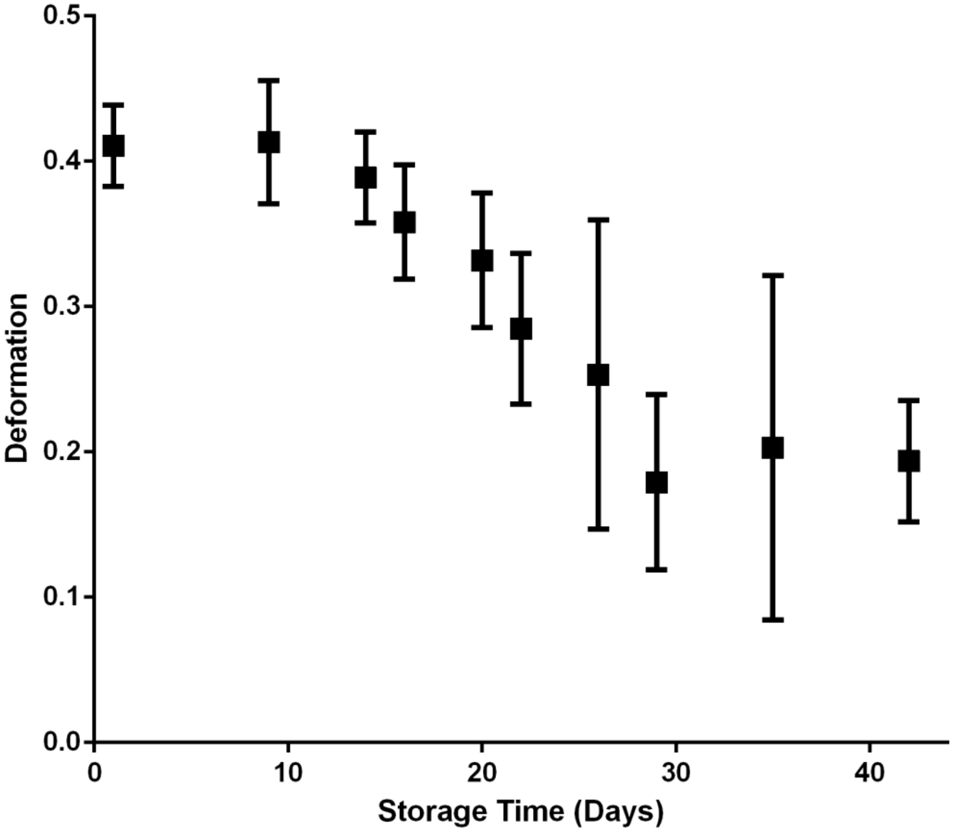

Figure 5.4. Deformability analysis of human RBC over storage time of 42 days (vendor-sourced). RBCs show an average decrease in deformability of 0.21, 50.61%. As storage time increases, the percentage of irreversibly changed and vesiculated cells increases, leading to further reductions in deformability.

Plotting only the fresh and most aged blood samples, we see an average decrease of cell size of 1.75 um^2, 7.91%, and decreased deformability of 0.21, 50.61% (Figure 5.5(a)). We can create the same plot with blood samples donated from graduate student volunteers, following IRB protocol. After 6 weeks of storage, we observe an average decrease in cell size of 7.46 um^2, 25.09%, and decreased deformability of 0.20, 50.65% (Figure 5.6(a)). Plotting the cell perimeter vs. the projected cell area in Figures 5.5(b) & 5.6(b) illustrates another means of visualizing the effects of decreased deformability, where the dotted line represents $P=A$. As the cells age in storage, storage lesions both decrease the deformability and overall size of the cells. As a result of these changes, the cell perimeter in the constriction is greatly reduced and the projected area is decreased, respectively. These changes lead the cell to a decreased ratio of P/A, placing them closer to the $P=A$ line. We observe that many cells cross this line into the region where $P/A<1$, though a large portion of the cells remain above this line, making the P/A ratio not a standalone metric for detection in itself.

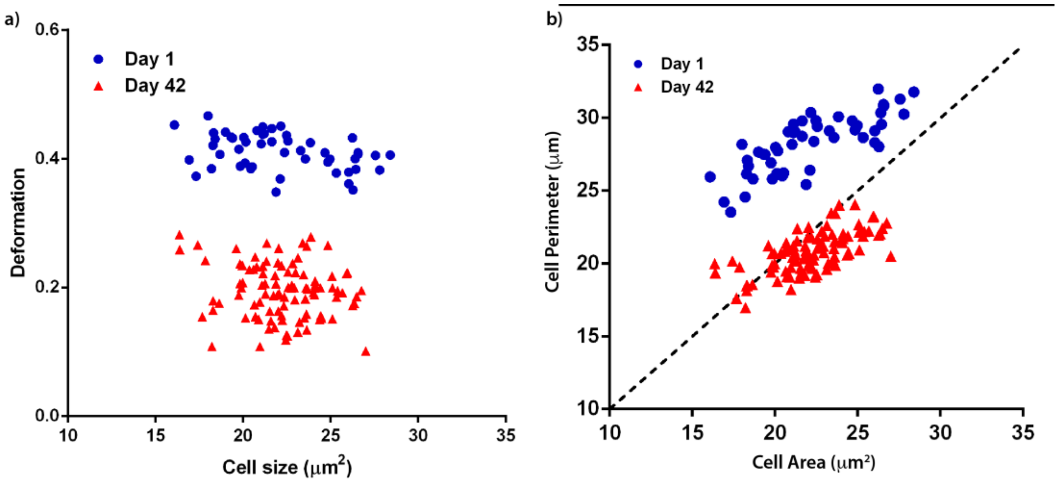

Figure 5.5. Overall change in deformability of vendor-sourced human RBCs. (a) Cells show a decreased size of 1.75 um^2, 7.91%, and decreased deformability of 0.21, 50.61%. (b) In a perimeter vs area plot, all fresh cells present well above the P = A line, indicating a ratio P/A > 1. The majority of aged cells present below this line, with an overall ratio P/A < 1.

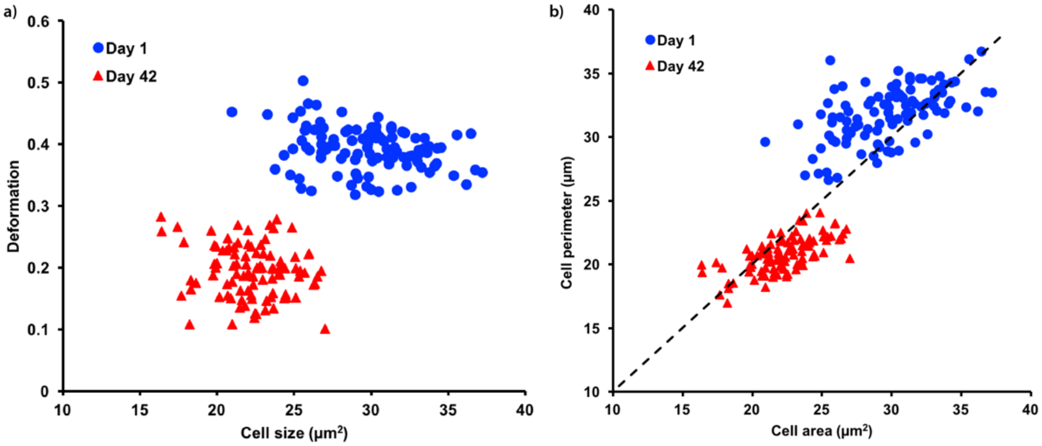

Figure 5.6. Overall change in deformability of grad volunteer human RBCs. (a) Cells show a decreased size of 7.46 um^2, 25.09%, and decreased deformability of 0.20, 50.65%. (b) In a perimeter vs area plot, the majority of fresh cells present above the P = A line, indicating a ratio P/A > 1. The majority of aged cells present below this line, with an overall ratio P/A < 1. Differences in the degree of change and P/A ratios between blood from two different sources (vendor-sourced vs. grad volunteers) may largely be due to biological variance, though variations in aliquot storage volume between the two sources is suspected be a factor.

Differences in the degree of change between the two samples sources (Figures 5.5 & 5.6) may largely be due to biological variance, though variations in aliquot storage volume are suspected to be a factor. We speculate that blood aging in small volumes (>0.2mL) differs greatly from aging in larger (0.3–1mL) or even relevant (>100mL) whole blood volumes, making studies using full blood bags imperative. Nonetheless, given the presented differences between the fresh and aged cells, real transfusion detection becomes feasible. It is likely that RBC vesiculation is accelerated in smaller volumes, accounting for the larger decrease in average cell size, though the viscoelasticity of the cells appears equally diminished in both cases.

5.3.3 *In Vitro* Autologous Transfusion

After characterizing the deformability behavior of the aging cells, we perform a simulated reinfusion of 2 units of blood; this corresponds to approximately 10% of the total blood volume. For this experiment, we again use graduate student donors. After mixing a 6-week sample into a freshly collected sample, the new "reinfused" sample is prepared and run through the RTDC device. With only 300 cells analyzed, we see a subpopulation emerge outside the spread of the main cluster; this grouping is believed to be a direct result of the presence of reinfused cells (Figure 5.7). The average of this outlying cluster shows a decreased deformability of 54% and good recovery of the reinfused cells, approximately 70% recovery of the total 10% reinfusion. We expect the recovery of these cells can be improved with increasing sample size.

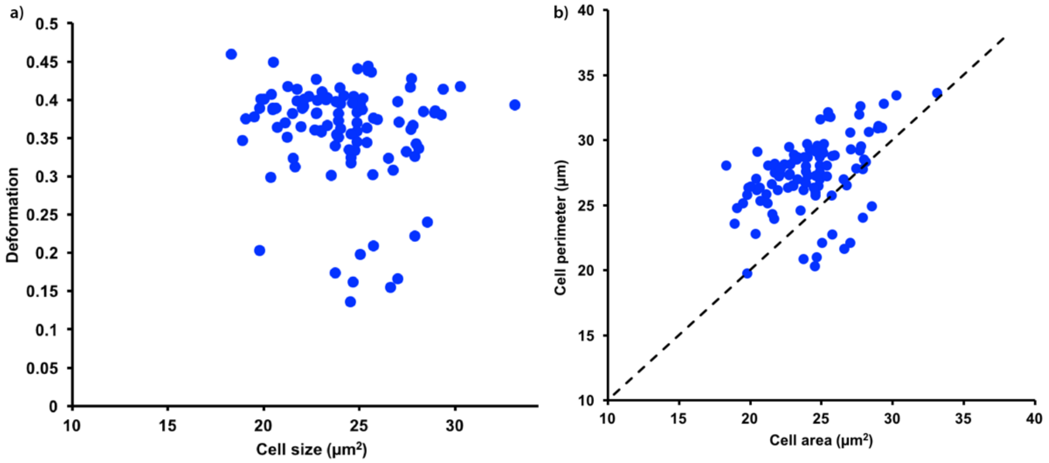

Figure 5.7. Deformability analysis of grad volunteer in vitro transfusion. A mixture of 90% fresh blood and 10% day-42 blood is analyzed and presented. (a) The clustering of a subpopulation outside the main grouping may be indicative of "doping." This outlying group represents approximately 7% of the reinfused portion, indicating 70% recovery of the reinfused cells. (b) Perimeter versus cell area. The presence of a removed, isolated group below the P = A line may be suggestive of "doping," but is not a definitive indication of such.

5.4 Conclusions

We have presented the ability to use RTDC as a means to mechanically probe differences in RBC populations, both in animals and humans. We also present the ability to determine the presence of an *in vitro* autologous transfusion from fingerprick samples of blood with good recovery of reinfused cells. While the work presented uses exclusively RBCs, this method is shown to be well suited for analysis of many different types of cells, provided the constriction size is changed to suit individual experimental needs. With minimal sample preparation required, this method becomes ideal for routine and spot testing; the absence of molecular tags and specialty reagents makes the tests themselves of negligible cost for the elite sporting entities that require them.

Funding Sources

This work was funded by the Partnership for Clean Competition (PCC) and the World Anti-Doping Agency (WADA).

Chapter 6

Microfluidic bubbler facilitates near complete mass transfer for sustainable multiphase and microbial processing

A microfluidic device (channels <70µm) was utilized to create micro-scale bubbles to significantly increase mass transfer efficiency at low flow rates. The convergence of one gas and two liquid channels at a Y-junction generates bubbles via cyclic changes in pressure. At low flow rates, the bubbles had an average diameter of 110 µm, corresponding to a volumetric mass transfer K_La of 1.43 h^{-1}. Values of K_La normalized per flow rate showed that the microbubbler had a 100-fold increased transfer efficiency compared to four other commonly used bubblers. The calculated percentage of oxygen transferred was approximately 90%, which was consistent with a separate off-gas analysis. The improved mass transfer was also tested in an algae bioreactor in which the microbubbler absorbed approximately 90% of the CO_2 feed compared to 2% in the culture with an alternative needle bubbling method. The microbubbler yielded a cell density 82% of the cell density for the alternative needle tip with an 800-fold lower flow rate (0.5 mL/min versus 400 mL/min) and a 700-fold higher ratio of biomass to fed carbon dioxide. The application of microfluidics may transform interfacial processing in order to increase mass transfer efficiencies, minimize gas feeding, and provide for more sustainable multiphase processes.

6.1 Introduction

Mass transfer from a gas to a liquid plays a critical role in many multiphase processes spanning multiple industries. Some example applications of gas to liquid transfer occur in biological processing in which carbon dioxide is transferred to liquid media for algae cell growth and oxygen is transferred to bacteria fermentation broths and mammalian cell culture bioreactors. Other applications include gas sequestration, chemical manufacturing (hydroformylation, alkylation, carboxylation, and polymerization) and hydrometallurgy[92]. In most cases, especially in industrial settings, companies and researchers desire an optimal transfer of the mass to the liquid in order to minimize the amount of gas fed to the multiphase process.

Obtaining a high mass transfer rate is ideal for processes that occur rapidly, such as microbial fermentation, because the dissolved solute has to be replenished quickly. For other processes, such as carbon sequestration or applications involving expensive gases, the goal is to achieve the highest fraction of the gas transferred to the liquid. For example, algal cells absorb carbon dioxide, which can then be converted to lipids for the production of biofuels. In addition, microbes can serve to capture carbon dioxide from the atmosphere as one potential approach to lower the carbon dioxide concentration in the atmosphere and reduce the accumulation of this greenhouse gas. Similarly, oxygen sparging is critical to aerobic respiration for bacteria producing biochemicals and mammalian cell lines generating biopharmaceuticals. However, much of the carbon dioxide to algal cultures or oxygen fed to mammalian and bacterial bioreactors is not successfully dissolved into the liquid broth and as a result, the undissolved gas passes directly through the bioreactor[93]. In these cases, the energetic output and costs associated with the gas sparging are wasted and must be repeated until sufficient solute is dissolved in the target liquid media. Alternatively, it would be highly desirable to deliver a higher fraction of the feed gas into the liquid solution as part of these multiphase processes.

The process of mass transfer from gas to a liquid occurs in three steps according to Whitman's two-film theory of gas absorption[94-96]. The first step involves the transfer of the component from the bulk of the gas, through the gas boundary layer, and to the phase boundary between the gas and liquid. Differences in partial pressures provide the driving force for this first step. The second step involves the instantaneous transfer across the phase boundary between the liquid and gas; this step is assumed to be extremely rapid and in equilibrium relative to the other steps. The third step transfers the component from the phase boundary through the liquid boundary layer to the bulk liquid. This step depends on the difference in concentration in the liquid of the component for the driving force[96]. From the bulk liquid, the dissolved component can then undergo other steps through chemical reactions or transport into cells. The overall transfer rate *(N_a)* from the bulk gas to bulk liquid depends on the volumetric mass transfer coefficient *(K_La)* and the concentration difference for poorly soluble gases (e.g., oxygen and carbon dioxide in water) as the driving force, according to Equation 6.1.

$$N_a = K_L a \cdot (C_a^* - C_a) \tag{6.1}$$

Therefore, the overall transfer rate depends on three factors: the overall mass transfer coefficient (K_L [distance/time]), the driving force in terms of concentration difference between the solubility limit in the liquid *(C_a^*)* and the dissolved solute concentration *(C_a^*)*, and the ratio of surface area to volume for the gas–liquid interface (a [distance^{-1}]). While the driving force *($C_a^* - C_a$)* can be increased by decreasing the temperature, increasing the overall pressure of the system, or by feeding pure gas instead of diluted gas, these approaches may not be feasible and can add to the overall costs.

Another option to increase mass transfer is to increase K_L by increased the mixing or turbulence, but this will also lead to increased energy inputs.

Alternatively, the interfacial area contribution may have the largest impact on mass transfer and represents a significant opportunity to improve the overall transfer rate. One approach is to take advantage of the surface area to volume ratio, *a*, which depends inversely on the characteristic bubble length. In this way, improved control and reduction in the size or distribution of the size of bubbles can increase mass transfer effectiveness.

By decreasing the bubble size, one can also lower the bubble velocity and conversely increase the bubble rise time. In this way, the overall time spent on interfacial gas exchange can be enhanced by decreasing bubbler diameter. Given the importance of bubble size to mass transfer for biological and other processes, methods dedicated to greater control of bubble size will become increasingly important in order to enhance chemical and biochemical interfacial process sustainability. Microfluidics is a useful tool for generating and controlling micron-scale gas bubbles and manipulating bubble interfacial area, rise time, and consequently the mass transfer rate and efficiency.

Previous researchers have used microfluidic devices to generate bubbles and drops for a variety of different applications. For example, T-shaped channel junctions have been used to create micro-emulsifications of monodispersed bubbles, anisotropic particles in the microchannels, and to generate and control microbubbles in oil[97]. A variety of different channel geometries have been utilized, including 2- and 3-D flow focusing devices, T-junctions, and parallel channels[97,98]. These tests have been performed for a variety of Reynolds numbers in different settings, primarily for bubble creation into liquids with high viscosities in microscopic settings[97].

To increase the mass transfer in a macroscopic setting, we utilized a microfluidic device to create micro-scale bubbles, increasing the surface area to volume ratio and, therefore, the K_La. Flow focusing microfluidic devices have previously shown the ability to produce stable micron sized bubbles with T-shaped junctions by having two liquid streams and one gas stream combine at the junction[97]. Instead of using a T-shaped junction, we utilized an angled, Y-shaped junction because we found the Y-junctions produced more uniformly shaped bubbles and reached a steady state of bubble production faster (Figure 6.1).

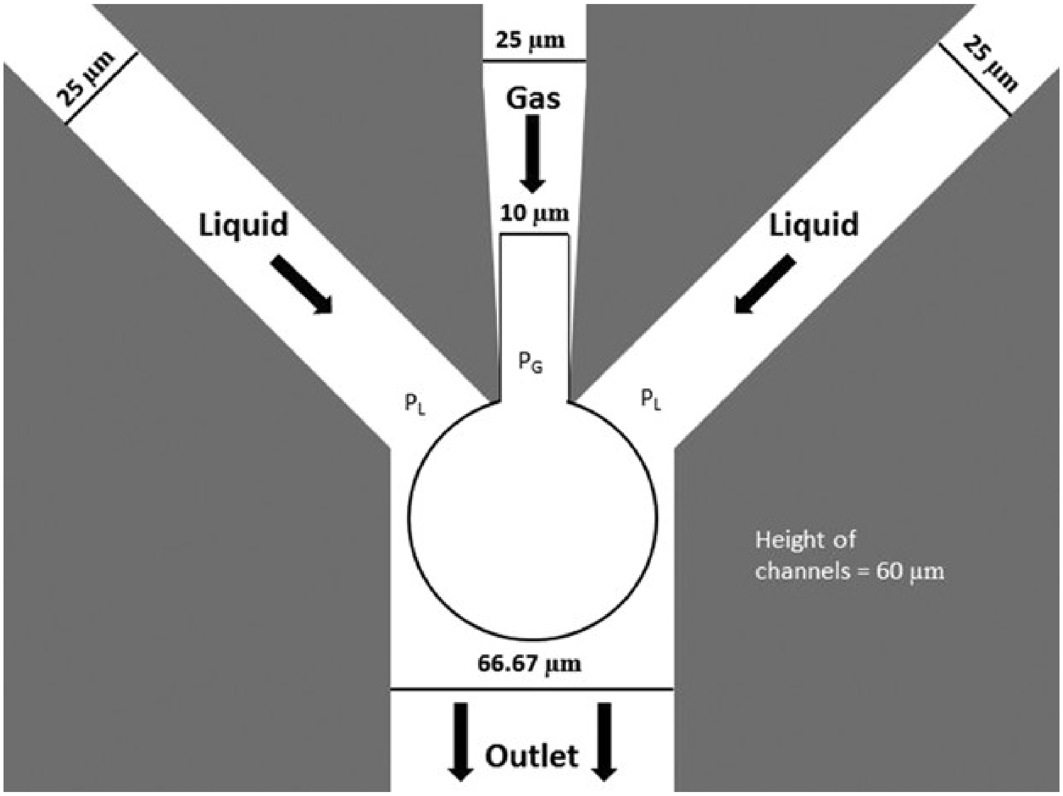

Figure 6.1 Design and size specifications of the Y-junction of the microfluidic device used to make micro-scale bubbles. The inlet channels for the liquid and the gas channels are 25 mm and the gas channel tapers to 10 µm at the junction which forms at a 40° angle. The outlet channel is 66.67 µm. Bubbles form in the junction, cutting off flow from the liquid channels except for a thin, wetting strip along the walls of the channel. The liquid pressure builds up and cuts off the bubble at the orifice. This process causes a cyclic bubble generation.

In the microfluidic device, both liquid and gas are driven into the channels using an externally applied pressure gradient at near identical pressures. The liquid enters through the top inlet port and splits into two symmetric side channels (Supplementary Figure S6.1). These two liquid channels combine, at a 40° angle, with a central gas channel (Supplementary Figure S6.1). Bubbles are generated using hydrodynamic flow focusing; the gas stream is focused into an orifice using two side channel fluid flows. Upon entry, the gas stream is hydrodynamically pinched to create a steady stream of monodisperse gas bubbles. We experimentally optimized the dimensions of our device so each individual bubble displaces the two liquid streams at the junction, temporarily cutting off fluid flow except for a thin wetting stream along the walls of the outlet channel. The wetting stream prevents the bubble from sticking to the sides of the channel and disrupting flow. As the bubble size and surface area increase, the influence of viscous drag from the two liquid streams eventually becomes larger than the interfacial forces holding the bubble at the nozzle, and the bubble detaches. When a continuous flow of liquid and gas are supplied, this process is repeated producing nearly identical bubbles at a constant frequency.

The channel width affects the size of the produced bubbles and the rate of delivery of gas to the system. Under the conditions used in this work, the bubble diameter is approximately equal to the width of the channel. Because bubbles are generated using an external hydrodynamic shear stress, which serves to pinch off the bubble during formation, we can increase the bubble diameter by increasing the channel width. However, increasing the channel width also decreases the flow rate of delivery of the gas to the system as an equivalent pressure will provide lower flow rates to a device with a larger cross-sectional area perpendicular to the flow direction. Conversely, one could produce, in theory, nanoscale drops with a nanoscale fluidic geometry. However, this would require much more complicated fabrication protocols and the device would suffer from clogging if there were any micron-scale particulate impurities in the streams. The devices utilized in this work were near the minimum channel size for feasibility and was based on a balance of these two factors.

In this study, we found that we could significantly increase the K_La and the efficiency of gas transfer to a liquid culture through the application of such a microfluidic device. This device enabled the generation of micro-scale bubbles at low flow rates, significantly improving the K_La per flow and the fraction of the gas transferred to the liquid. Ultimately, the applicability of the device was validated by supplying carbon dioxide to a fermentation system growing the green microalgae Chlorella vulgaris.

6.2 Methods

6.2.1 Microfluidic Fabrication

For the fabrication of the microfluidic flow-focusing devices, we used well-developed soft lithography techniques. Negative photoresist (SU-8 3050, Microchem Corp., Westborough, MA) was spin-coated onto a silicon wafer (Silicon Inc., Boise, ID) and exposed to a UV light source (KLOÉ) through a negative mask printed on a transparency. The result, after developing, was a silicon wafer with raised structures 60 μm high that act as the master mold with the specifications of Figure 6.1 with the distance from the junction where bubbles form to the outlet port being 2 mm. A 10:1 ratio of the elastomer and curing agent, PDMS, is poured over the wafer, cured, and peeled off. Biopsy punches (Ted Pella, Inc., Redding, CA) are used to create inlet ports for the fluid flow. The surface of both the PDMS and a cleaned microscope slide are treated with oxygen plasma and placed in contact to form a bond; the bonded devices are baked at 85°C overnight to enhance this bond. Fluid and gas streams are delivered via pressurized vials to deliver a constant flow rate. The outlet stream, consisting of media and microbubbles, exited the outlet port through tubing with an inner diameter of 0.02 inches and into the bottom of the liquid vessel.

6.2.2 K_La determination

Values for K_La are difficult to calculate and usually are determined experimentally. To determine the K_La values for different systems, we placed 500 mL of water at 25°C in a beaker with a diameter of 10 cm, giving a liquid height of 6.36 cm. We placed a dissolved oxygen (DO) probe (Vernier) in the liquid and stirred the liquid with a magnetic stirrer at a constant agitation rate of 175 rpm. The computer captured and recorded DO readings every second. Initially, we fed air to the bottom of the liquid until the DO was constant at the saturation point. Then, we fed nitrogen gas into the culture to drop the DO. Once the DO dropped significantly, we switched the gas feed back to air and monitored the DO (Supplementary Figure S6.2). To calculate the K_La, we plotted the

$\ln(C_a^* - C_a)$ for the segment of interest after the switch back to air[99]. In this case, C_a^* is the highest concentration of the DO, achieved at the beginning of the trial, and C_a is the DO for the rest of the trial. For the segment of interest, the resulting graph of the $\ln(C_a^* - C_a)$ over time produces a straight line with a negative slope (Supplementary Figure S6.3). The K_La is the slope multiplied by negative one and has units of inverse time.

6.2.3 Fraction of Oxygen Transferred

The fraction of oxygen transferred calculation were verified utilizing an oxygen gas sensor (Vernier) with the K_La testing. The oxygen gas sensor was sealed to the top of the off-gas above the liquid the K_La testing was done on and recorded the oxygen gas concentration every second. As nitrogen gas was fed to the liquid, the DO and the oxygen gas concentration decreased. When we bubbled air into the system to test the K_La, the oxygen gas sensor recorded the change in oxygen concentration, which allowed for the calculation of oxygen gas concentration in the bubbles. The trend line used to determine the oxygen gas concentration in Figure 6.7 was calculated using the LINEST linear regression least square method on Microsoft Excel. This method also provides an estimate of the coefficient of determination (R^2) and errors for both the slope and intercept for generating the significant figures of the trend line equation.

Closed containers were used and the dissolved oxygen and oxygen gas concentrations were measured. After switching from the nitrogen feed to air fed through the microfluidic bubbler, the dissolved oxygen concentration increased while the oxygen gas levels in the headspace declined due to the oxygen transfer from the bubbles to the liquid. As a result, the bubbles leaving the liquid had been stripped of much of the oxygen and thus contained primarily nitrogen and the other components of air, without oxygen. The oxygen deprived bubbles emerging into the head space caused the oxygen gas concentration in the head space to decline gradually as these oxygen-deprived bubbles replaced the off-gas headspace previously containing a mixture of air and nitrogen.

6.2.4 Additional Bubbling Equipment

Four common additional methods of supplying gas to liquids for mass transfer were tested against the microfluidic bubbler and included an open-tube, needle tips, a common aquatic stone sparger, and an industrial sparger used for bioreactors. The open-tube was a Bellco Glass straight sample metal pipe with an inner diameter of 0.5 cm and an outer diameter of 0.625 cm. The needles used to supply gas were stainless steel, 19 gauge, 4″ long, blunt end luer needles. The common aquatic sparger was the small air stone cylinder from Active Aqua with a diameter of 1.7″ and a height of 2.0″. The industrial sparger was a Bioengineering aeration tube with sinter-metal microsparger for 5 L vessel.

6.2.5 Gases and Liquids

The liquid used to perform all of the experiments was a salt media commonly used for algae culture, Bold's Basal Media (BBM) [100]. BBM media contains 250 mg/L sodium nitrate, 175 mg/L potassium phosphate monobasic, 75 mg/L magnesium sulfate heptahydrate and potassium phosphate dibasic, 50 mg/L EGTA, 31 mg/L potassium hydroxide, 25 mg/L calcium chloride dihyrdate and sodium chloride, 11.42 mg/L boric acid, 8.82 mg/L zinc sulfate heptahydrate, 4.98 mg/L iron sulfate heptahydrate, 1.57 mg/L copper sulfate pentahydrate, 1.44 mg/L manganese chloride tetrahydrate, 0.71 mg/L molybdenum trioxide, 0.49 mg/L cobalt nitrate hexahydrate, and 1 µL sulfuric acid with the pH adjusted to 6.8. This media was also supplemented with 0.5% pluronic F-68 as a surfactant to stabilize bubble formation. The addition of pluronic F-68 has shown no negative effects on algal cell growth and has been used in many other cell cultures, including insect and mammalian cultures[101,102].

6.2.6 Equipment

The bubbles in the microfluidic channels were analyzed with a Nikon TI-E confocal microscope. The probes measuring dissolved oxygen, oxygen gas, and carbon dioxide gas were from Vernier and were recorded every second during trials by LoggerPro software. To take pictures and videos of the bubbles in the liquid, a Sony Cybershot DSC-H20 camera was used and ImageJ was used to analyze bubble size.

6.2.7 Algae Cultures

The strain *C. vulgaris* (UTEX 395) was grown in 500 mL of BBM media in a bioreactor with a total volume of 1.25 L. Gas was fed as 5% CO_2 in air at a flow rate of 400 mL/min for the needle tip culture and 0.5 mL/min for the microbubbler. The bioreactors operated at room temperature (~23°C) with an agitation rate of 200 rpm and a constant light intensity of 10,000 lux (~300 $\mu E/m^2/s$). Growth was recorded by measured optical density at 600 nm using a Promega Glomax multidetection spectrophotometer. Carbon dioxide concentration was measured using a Vernier carbon dioxide gas sensor.

6.3 Results

6.3.1 Bubble Size

The purpose of using the microfluidic bubbler is to create micro-scale bubbles to increase the mass transfer from gases to the bulk liquid. As a representative case study, we bubbled air through the liquid algae growth medium, Bold's Basal Medium (BBM), using the microchannel set-up illustrated in Figure 6.1. For bubble flow, the pressure of the liquid and gas streams were set at similar pressures and then adjusted to facilitate bubble formation in the channels. Next, the size and distribution of bubble sizes produced in the liquid were evaluated. Shown in Figure 6.2(a) is an image of the bubbles produced in the liquid while Figure 6.2(b) shows the bubbles produced from a typical industrial sparger. Shown in Figure 6.3 is the size distribution of the bubbles produced using the microbubbler following multiple trials. The distribution shows that the bubbles from the microfluidic device averaged 110 microns in diameter. This normal distribution provides more precise bubble production, compared to the other systems considered (Supplementary Figure S6.4).

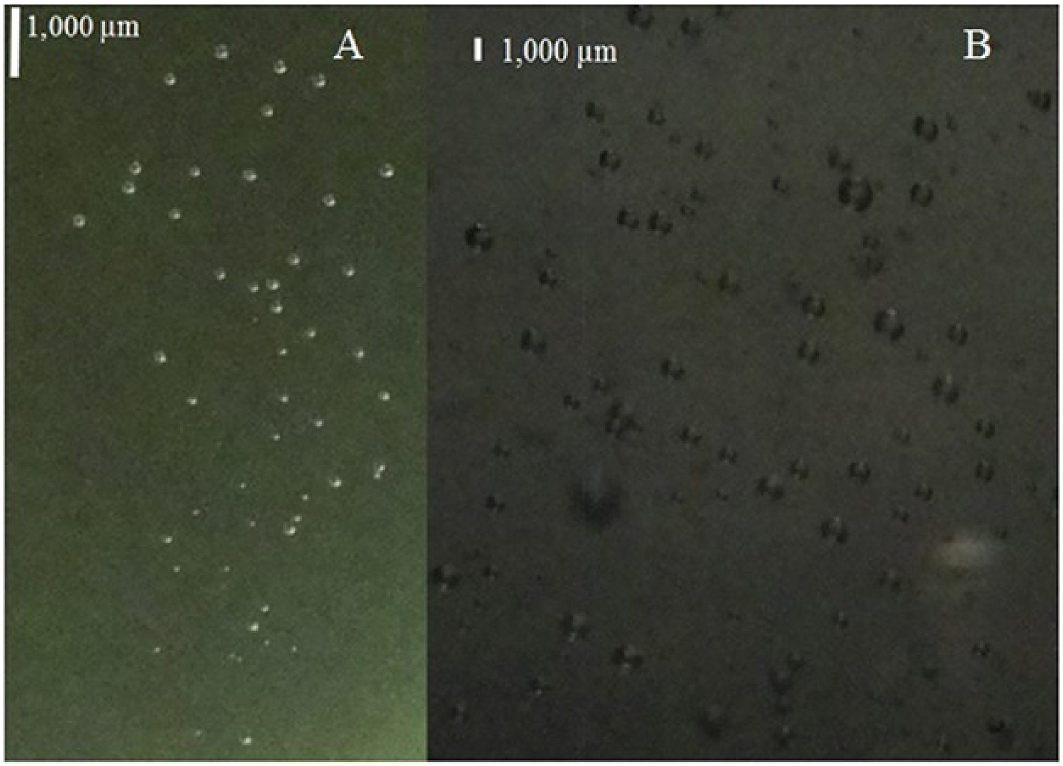

Figure 6.2 Bubble images. (a) Bubbles in liquid created by microfluidic bubbler at a flow rate of 0.50 mL/min and (b) bubbles in liquid created by the next smallest alternative, the industrial sparger at 500 mL/min.

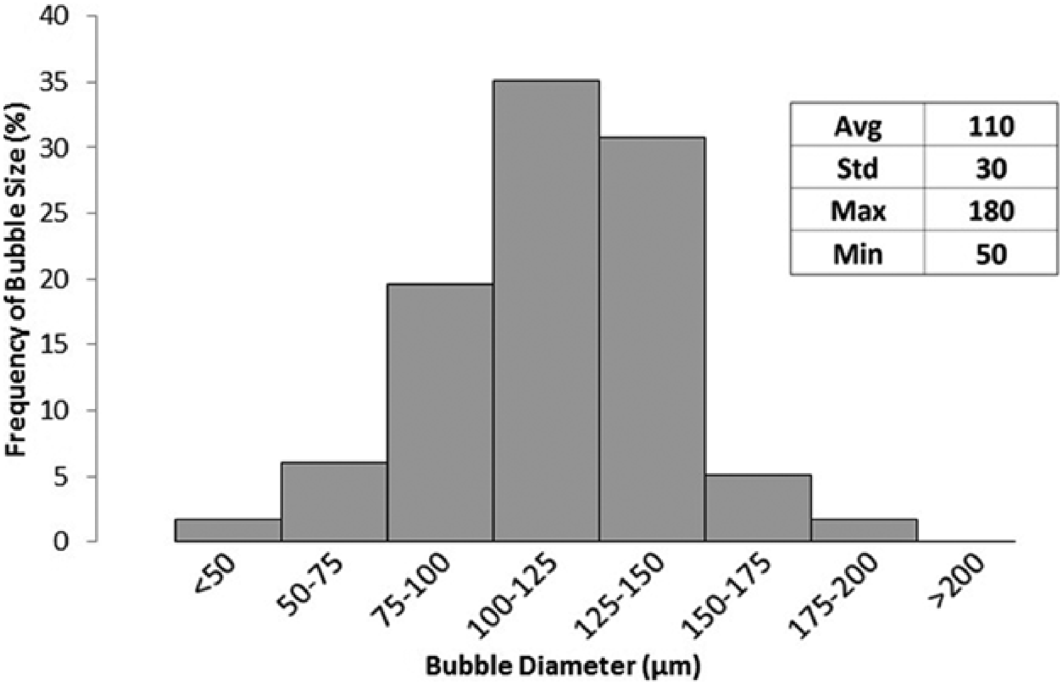

Figure 6.3 Bubble diameter distribution. The average bubble size from the microbubbler with a flow rate of 0.50 mL/min was 110 mm with a standard deviation of 30 mm with a maximum size of 180 mm and minimum size of 50 mm.

In order to see how the bubble size of the microfluidic bubbler compared to a range of other devices for supplying gas, we compared the microfluidic device to an open-tube, a needle tip, an aquatic sparger, as well as an industrial sparger gas feeding system. Shown in Figure 6.4 is the average bubble size determined for the other four methods as a function of gas flow rate. Firstly, the microfluidic bubbler operates at a much lower flow rate than the other methods, with the other methods operating at minimum flow rates of 100, 400, 700, and

500 mL/min for the open-tube, needle, aquatic sparger, and industrial sparger, respectively. At lower flow rates, the other devices did not produce bubbles into the liquid media. At extremely low flow rates, below ~1 mL/min, the bubbles of the microfluidic bubbler were all well below 1000 μm in diameter with the lowest average diameter of 110 μm. The microfluidic device, needle, and open tube exhibit the requirement of trailing gas being pinched off to form bubbles, showing an increase in bubble size with flow rate. The bubble size stayed relatively constant for both spargers based on the pore size of the spargers, leading to the industrial sparger having slightly smaller bubble diameters due to smaller and more concise pores. The spargers created no bubbles below 500 and 750 mL/min for the industrial sparger and the aquatic sparger, respectively, due to too low of a pressure to push the gas through the pores.

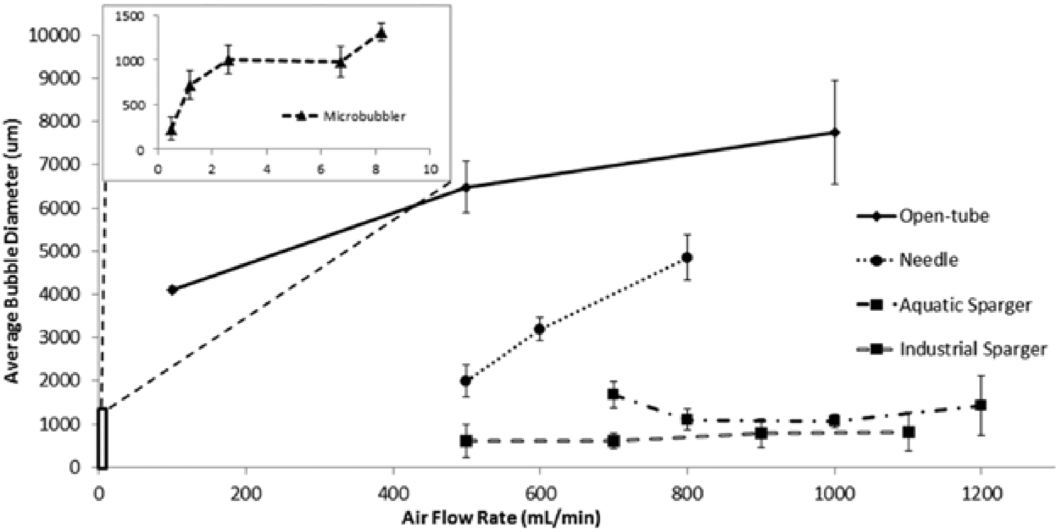

Figure 6.4 Bubble size dependence on flow rate for all devices. All bubble sizes increase with increasing flow rate except for both spargers, which remained constant. The microbubbler had the

smallest bubbles, followed by the industrial sparger, aquatic sparger, then the needle, and finally the open-tube.

6.3.2 Volumetric Mass Transfer Coefficient (K_La)

The goal of the microbubbler is to make gas solutes available in solution more efficiently than conventional spargers. Therefore, the K_La was analyzed for the microbubbler, as shown in Figure 6.5(a) for the lower flow rates achieved. Interestingly, the K_La value for the microfluidic bubbler increased with increasing flow rate until 2.6 mL/min, corresponding to a K_La of 5.22 h^{-1}. After this peak, the K_La decreases gradually with increasing flow rate up to 8.2 mL/min, corresponding to a K_La of 4.16 h^{-1}.

Because the flow rates of the systems were orders of magnitude apart and increasing flow rate increases K_La for most devices, the K_La values were normalized by taking a ratio of the K_La multiplied by the volume of liquid (constant) and divided by the flow rate, making this value dimensionless[103,104]. Previous modeling studies have normalized the K_La with the flow rate and volume[105]. Shown in Figure 6.5(b) are the normalized K_La values for the microfluidic bubbler compared to the open-tube, needle, and sparger systems. According to the normalized K_La values, the microbubbler system is approximately 100 times more efficient in transferring mass from a gas to a liquid than the other aeration systems.

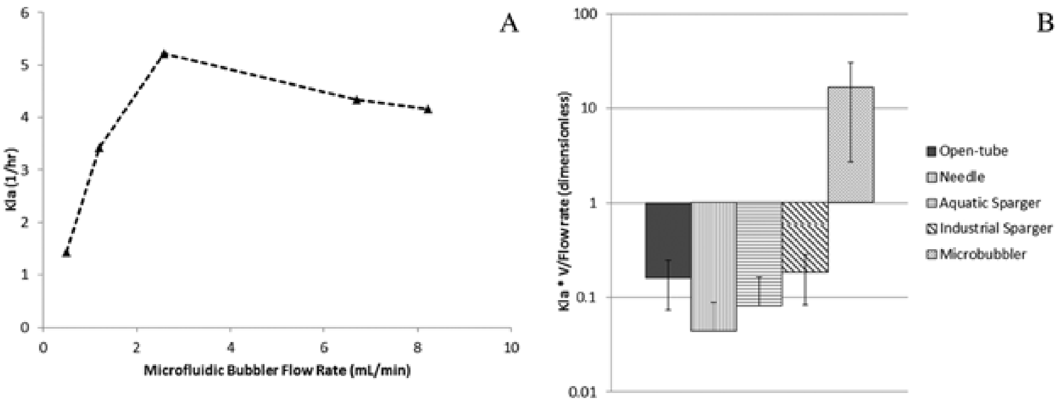

Figure 6.5 $K_L a$ of the microbubbler compared to other methods. (a) $K_L a$ dependence on flow rate for the microfluidic bubbler. (b) All of the $K_L a$ values for all systems were normalized with flow rate and volume of liquid. The microbubbler had a 100-fold better transfer per flow rate than the other four methods.

6.3.3 Fraction Oxygen Transferred

In order to test how much of a particular solute is transferred from the microbubbles into solution, we calculated the fraction of oxygen transferred to the liquid (δ), by utilizing the $K_L a$, C_a^*, height (h) and cross sectional area (A_c) of the liquid perpendicular to the flow, flow rate of the gas ($\dot{V}$) and the density of the component of interest in the gas (j, Equation 6.2) [106].

$$\delta = \frac{K_L a \cdot (C_a^*) \cdot h \cdot A_c}{\dot{V} \cdot j} \tag{6.2}$$

Shown in Figure 6.6 are the values of fraction of oxygen transferred for different sparging devices. The fraction of oxygen transferred for the industrial sparger increases from 0.003 to 0.011 for flow rates of 500–1100 mL/min and the aquatic sparger increases from 0.002 to 0.005 for flow rates of 700–

1,000 mL/min. Conversely, the fraction transferred for the open-tube decreases from a maximum of 0.01 to 0.004 for flow rates from 100 to 1000 mL/min while the needle tip stays approximately constant at a fraction transferred of 0.002 for flow rates of 500 to 800 mL/min. In contrast, the microfluidic bubbler provides a significantly higher fraction of oxygen transferred of 0.91 (±0.15) and 0.90 (±0.13) at the lowest flow rates of 0.5 and 1.2 mL/min, respectively, indicating near complete transfer of oxygen.

Unlike the other devices, the fraction of oxygen transferred increases with decreasing flow rate for both the microfluidic bubbler and the open-tube device (Figure 6.6). Both the spargers increased the fraction of oxygen transferred with higher flow rates because the bubbles remained relatively constant in size regardless of the amount of gas flow rate fed to the system.

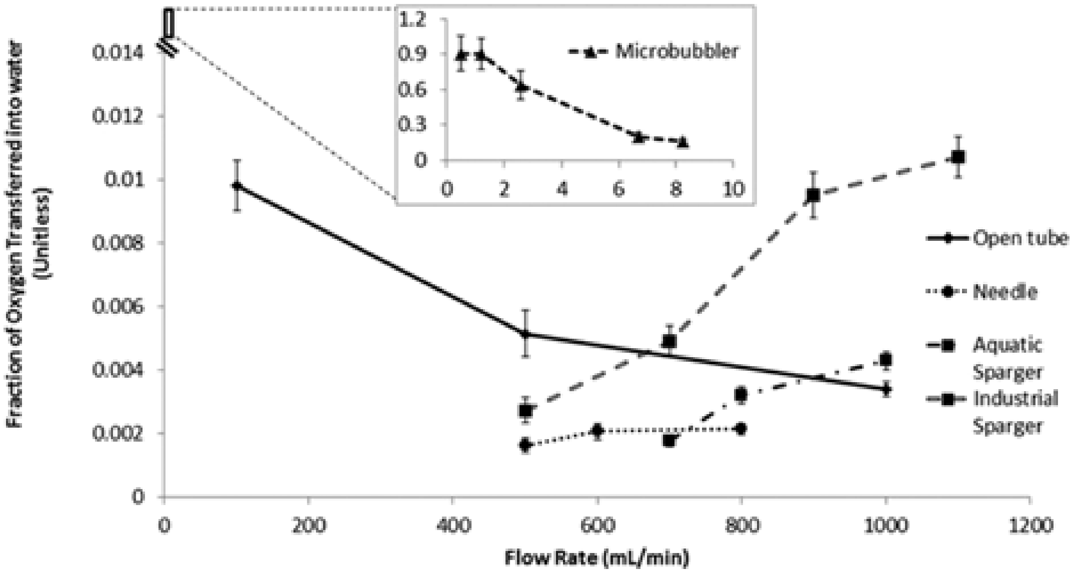

Figure 6.6 Fraction of oxygen transferred dependence on flow rate. Fraction oxygen transferred dependence on flow rate for all systems. For low flow rates (0.5 and 1.2 mL/min) of the microfluidic bubbler, the fraction oxygen transferred is approximately 0.90 whereas the fraction transferred for the other systems is generally <0.01.

As a secondary approach for evaluating the fraction of oxygen transferred, the oxygen gas levels in the headspace were measured using an oxygen gas sensor throughout the K_La trials. The oxygen gas concentrations *(C_O)*, the volume of the head space *(V)*, and the flow rate *(Q)*, can be used to calculate the concentration of oxygen in the bubbles leaving the liquid *(G)* using a modified dilution ventilation equation (Equation 6.3) [107].

$$\frac{dC_0}{dt} = \frac{Q \cdot (G - C_0)}{V} \tag{6.3}$$

Integration of this equation can be used to calculate the average concentration of oxygen in the outlet bubbles (Equation 6.4). The fraction of oxygen transferred using the off gas at any time t_2 can be calculated by dividing the concentration of oxygen in the outlet bubbles by the concentration of oxygen in room air (209 parts per thousand [ppt]).

$$G = \frac{C_2 - C_1 \cdot e^{\left(\frac{-Q \cdot (t_2 - t_1)}{V}\right)}}{1 - e^{\left(\frac{-Q \cdot (t_2 - t_1)}{V}\right)}} \tag{6.4}$$

Shown in Figure 6.7 is the concentration of oxygen in the sealed headspace for $K_L a$ testing of the microbubbler with a flow rate of 0.50 mL/min. The beginning of the oxygen transfer to the liquid (~17.5 min) began at the time at which nitrogen gas feeding was stopped and the microfluidic bubbler began flowing air into the media (see Materials and Method for $K_L a$ determination). When the bubble of air enters the liquid, it consists of air (78% nitrogen, 21% oxygen, 0.9% argon, 0.04% carbon dioxide, and minor other components with less than 0.01%). As the bubble travels through the liquid, the oxygen will diffuse into liquid based on the solubility of the gases in the liquid. Therefore, when the bubble leaves the liquid and enters the headspace, it will have a different composition than entering the liquid. The oxygen level in the headspace progressively declined as a result of the transfer of oxygen from the bubbles into the liquid, leading to the replacement of oxygen with nitrogen in the headspace. The average concentration of oxygen in the bubbles leaving the liquid can be calculated by measuring that change of oxygen concentration in the headspace. A line of best fit for the headspace oxygen concentration was applied from the beginning to the end of the bubbling period in order to estimate the average concentration of oxygen in the bubble exiting the liquid, G, according to Equation 6.4. Calculations indicated that the bubbles exiting the liquid contained approximately 38.06 ppt oxygen, which corresponds to about 18% of oxygen in room air and a fraction of oxygen transferred of 0.82 ± 0.08. Thus, the off gas fraction of oxygen transferred is similar in value to that calculated using Equation 6.2 (0.91 ± 0.15), at an equivalent flow rate.

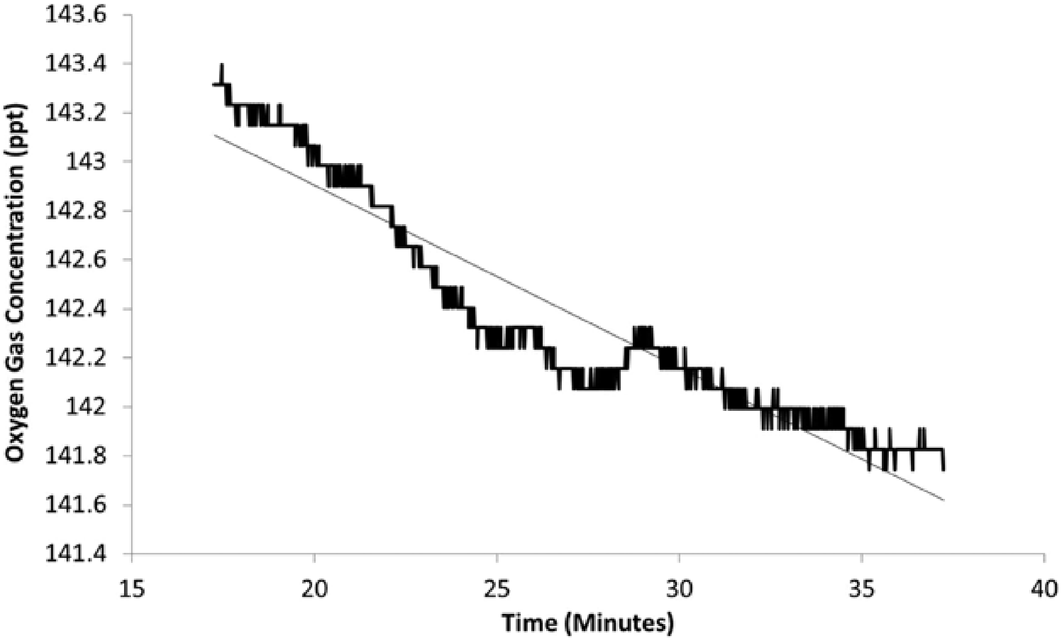

Figure 6.7 Oxygen concentration in headspace above K_La testing with an air flow rate of 0.50 mL/min for fraction oxygen transferred calculation. The equation of the line of best fit for the change in oxygen concentration (ppt) with time (min) is given by $y = -0.0745x + 144.39$ with a coefficient of determination of $R^2 = 0.9$. The drop over time corresponds to a transfer of $82 \pm 8\%$ of the oxygen in the air to the liquid.

Once, we established that the microfluidic bubbler provided optimal conditions for transferring solutes from gas to a liquid, the frequency of bubble generation was measured over a range of liquid heights for various flow rates to see if it can be adjusted for larger reactor sizes (Supplementary Figure S6.5). Below 30 cm in liquid height, the frequency of bubble generation stayed approximately constant at 2–18 bubbles/s for flow rates of 0.22–0.98 mL/min, respectively. With increasing flow rates, we expect higher bubble frequencies and larger heights at which the microbubbler can operate.

6.3.4 Microbubbler in an Algae Culture

We next examined the transfer of carbon dioxide, another sparingly soluble gas, to a growing microalgal culture. The K_La value of carbon dioxide can be estimated by relating the measured K_La of oxygen in the system and applying the diffusivities of both gases, as described below in Equation 6.5[108].

$$K_La(CO_2) = K_La(O_2) \cdot \left(\frac{D_{CO_2}}{D_{O_2}}\right)^{0.5} \tag{5}$$

A culture of *C. vulgaris* was grown using both the microbubbler and the needle tip with flow rates of 0.5 and 400 mL/min, respectively (Table 6.1). The cells were grown for 240 h and then growth and processing parameters were estimated and compared.

As shown in Table 6.1, the culture with the needle tip at a flow rate two orders of magnitude higher exhibited a slightly higher growth rate and a final OD_{600} of 0.841 compared to 0.703 for the microbubbler. This OD corresponds to a biomass density of 0.60 g/L for the needle tip versus 0.48 g/L for the microbubbler. In addition to the final cell densities, the carbon dioxide concentrations in the headspace of the reactors were compared. Table 6.1 also shows the carbon dioxide concentration in the headspace for the microbubbler was less than 10% of the concentration of that in the headspace of the needle tip. Furthermore, given that the feed gas contained 5,000 parts per million (ppm) CO2, the microbubbler culture transferred more than 90% of the CO_2 in the feed. In contrast to this finding, the headspace for the needle feed had 98% of the feed gas concentration, meaning only 2% of the CO_2 in the feed gas was transferred to the culture. Overall, the total CO_2 fed/g of biomass generated was 2.9 g/g for the microbubbler compared to 1900 g/g for the needle tip, an almost 700-fold improvement.

Table 6.1 Performance of the microbubbler in an algae bioreactor.

Bubbling method	Fraction gas transferred	Required CO_2 flow rate (mL/min)	Total cost/L culture/h/fraction oxygen transferred ($/L/h)
Microbubbler	0.908	178	1.76
Open tube	0.010	16,532	7.56
Needle	0.002	75,948	28.63
Aquatic sparger	0.004	37,767	15.09
Industrial sparger	0.011	15,139	7.07

The cost of operation of the various gas sparging systems based on the fraction of gas transferred and the required flow rate of the systems also shows the microbubbler outperforms the other systems. The cost/L media is estimated as $1.70/L and the cost of pure CO_2 gas feed is $0.06/L/h.

6.3.5 Estimate of Gas Feed Costs for Large Scale Algal Bioreactors

Another relevant consideration of the microfluidic bubblers is whether these devices are cost efficient for transferring solute at larger scales. As a first approximation, the cost of inputs was compared for the devices based on the amount of mass transferred (Table 6.2). Device capital and pumping costs were ignored for this initial comparison but can be added in more detailed comparisons. In this analysis, the cost of media and gas needed/L to run a typical microalgae bioreactor with BBM media using 10% CO_2 in air at a required absorption rate of 162 mL of CO_2/min/L culture were considered. An estimated required value of 162 mL CO_2/min/L culture is calculated from the maximum theoretical photosynthetic rates of algal cultures using an estimated average cell density of 1 × 108 cells/mL and ignoring shading effects[109].

We estimated the amount of gas input given the fraction of the gas transferred for each input system, since all systems except the microbubbler will require much higher flow rates to transfer a sufficient amount of gas for cellular consumption. As shown in Table 6.2, the processing costs/L/time basis were nearly four times lower for the microbubbler when compared to the next most efficient systems, the open-tube and industrial sparger. Other systems, such as the needle sparger and aquatic sparger, exhibit processing costs that were orders of magnitude higher due to the high amounts of CO_2 that must be pumped through these spargers to provide for sufficient dissolved CO_2 in the algal bioreactors. This fourfold decrease to the cost of pumping gas decreases the cost of feeding CO2 which represents approximately 5–9% of the total operation cost for an algal culture[110,111].

Table 6.2 Economic analysis of microbubbler operation compared to other bubbling methods.

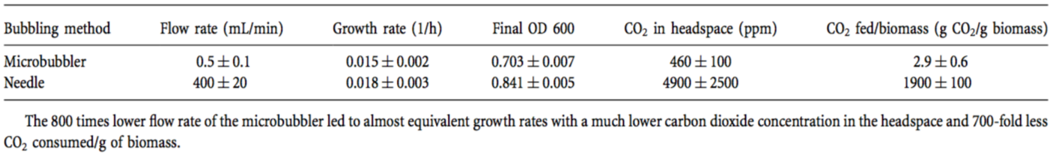

Bubbling method	Flow rate (mL/min)	Growth rate (1/h)	Final OD 600	CO_2 in headspace (ppm)	CO_2 fed/biomass (g CO_2/g biomass)
Microbubbler	0.5 ± 0.1	0.015 ± 0.002	0.703 ± 0.007	460 ± 100	2.9 ± 0.6
Needle	400 ± 20	0.018 ± 0.003	0.841 ± 0.005	4900 ± 2500	1900 ± 100

The 800 times lower flow rate of the microbubbler led to almost equivalent growth rates with a much lower carbon dioxide concentration in the headspace and 700-fold less CO_2 consumed/g of biomass.

6.4 Discussion

In this study, we demonstrated that Y-junction microfluidic devices are able to form stable, small bubbles for use in transferring mass from gas bubbles to liquid. The small standard deviation on the bubble size distribution and the fact that 85% of the bubbles fall within a 75 micron span (75–150 μm) show that the microfluidic bubbler creates near constant bubble sizes at constant, low flow rates. The ability to accurately control and reproduce bubble sizes becomes increasingly important in processes in which it is important to reliably control all parameters, such as in complex biological processes or chemical reactions. This ability to fine tune the sizes of the microbubbles will be especially critical for modeling and control purposes.

At low flow rates, the microfluidic bubbler generates bubbles much smaller than the other systems, showing it outperforms the other system in creating small bubbles, especially at low flow rates. For the microfluidic bubbler, the open-tube, and the needle tip, the bubble diameter becomes larger with increasing flow rate, seen in Figure 6.4, consistent with findings from papers analyzing macroscopic bubble creation[112,113]. The spargers' bubble sizes are maintained with flow rate, because the gas is pushed through the constant sized pores equally, creating relatively constant bubble sizes.

Another benefit to the microfluidic bubbler system is the low flow rates for operation. In contrast, the open tube, needle tip, aquatic sparger, and industrial sparger had minimum flow rates of 100, 400, 700, and 500 mL/min, respectively. Below those flow rates, the systems formed no bubbles. The low flow rate of the microfluidic bubbler allows for a smaller amount of feed gas to form bubbles, which can generate significant savings for processes that use expensive gases. Because many processes, especially in an industrial setting, need a large flow rate of the gas, we can combine multiple devices in parallel to increase the total flow rate and improve the overall $K_L a$ further. We combine devices rather than adjusting the flow rate because raising the flow rate increases bubble diameter and lowers the efficiency of the transfer.

To verify that smaller bubbles improve mass transfer due to the larger surface area to volume ratio, we measured the K_La over a range of flow rates for the microfluidic bubbler. The K_La value for the microfluidic bubbler peaks at a flow rate of 2.6 mL/min. The peak occurs because as the flow rate starts to increase further, the bubble size increases. The larger bubble diameter gives the bubbles a larger volume, increasing the buoyant force on the bubbles, causing the faster rise velocity of the bubbles[108]. This increased buoyant force causes the bubbles to rise out of the liquid faster, giving less time for transfer. Below the peak rate, the K_La decreases because there is a smaller amount of total gas mass released into the liquid. Less oxygen is introduced to the system due to the low flow rates and bubble generation frequency, causing the dissolved oxygen concentration to not increase as rapidly, lowering the overall K_La[105,114,115].

Comparing the microfluidic bubbler to the other devices in terms of the K_La normalized with flow rate demonstrates the benefits of the bubbler compared to other systems that have much higher flow rates. The aim of the microfluidic bubbler is to increase the mass transfer from gas to liquid while minimizing the amount of feed material necessary and improving efficiencies of delivery. Even though the K_La values for all of the systems, including the microbubbler, are approximately constant, the flow rate of the microfluidic bubbler is two orders of magnitude smaller than the other systems. Therefore, the K_La normalized per flow rate of the microfluidic bubbler is 100 times more efficient at transferring mass/amount of material fed. Lowering the flow rates of the other systems to create smaller bubbles and improve K_La values to those comparable to the microfluidic bubbler would be difficult to implement. For these systems, the K_La values increase significantly with higher flow rate, so decreasing the flow rate will likely lead to lower K_La values (Supplementary Figure S6). Using the microfluidic bubbler system, the most time efficient (highest K_La) system used a flow rate of 2.6 mL/min, while the most complete transfer (highest K_La per flow rate) occurred at low flow rates of 0.5 mL/min.

The fraction of oxygen transferred decreased with increasing flow rate, similar to bubble size (Equation 6.2). The increased bubble size gave faster rise velocities and less time for the oxygen to transfer from the bubble to the liquid. At the lowest flow rates for the microfluidic device, the fraction of oxygen transferred was approximately 90%, indicating almost complete transfer of the oxygen from the air to the liquid. We verified this calculation by analyzing the off-gas as part of the K_La measurements (Figure 6.7). By measuring the change in the sealed headspace oxygen, the amount of oxygen transferred was estimated at 82 ± 8%, which is similar to the value of 91 ± 15% determined by Equation 6.2. More importantly, this high percentage of oxygen transfer shows the microfluidic bubbler improves gas mass transfer while minimizing the amount of feed gas necessary.

Although these results are significant advancements at the laboratory scale, it will be important to demonstrate scalability for larger vessels and in commercial application. We have shown that this bubbler system at low flow rates works extremely well in volumes of liquid with heights up to 32 cm (Supplementary Figure S6.5). It can also work effectively at heights above this by increasing the pressure that drives the liquid and gas feeds. Increasing the flow rates also produces a higher frequency of bubble generation, as verified by others[116,117]. One aspect of the microbubblers that could pose a challenge for industrial use is that the pressure drop required for generating gas and liquid feed scales linearly with the device dimensions. In other words, a larger bubbler would require an equally larger pressure drop to produce the necessary bubble rate for industrial bioreactor use. These pressures could place new constraints on both the microfluidic device materials required to safely work under these pressures and the costs associated with continuously sustaining them in the bioreactor. Although our devices can sustain 40 psi before the microfluidic channels rupture and debond from the glass substrate, future work will be needed to evaluate the feasibility of building devices at higher operating pressures as needed. Alternatively, smaller devices can be deployed in parallel and these permit generation of the small bubble sizes.

The flexibility of using different liquid operating heights provides a wide range of operating conditions and applications. For example, a microbubbler can be applied for bubbling gas to algal ponds in long raceways with shallow depths. This device can also be used in mammalian and bacterial cultures for optimal feed of oxygen for maximizing growth.

When implemented into an algal bioreactor, the microbubbler showed a much better fraction transferred and better overall growth and consumption of carbon dioxide than other bubbling methods in terms of total flow rate (Table 6.1). Obtaining nearly equivalent biomass with a flow rate 800 times lower demonstrates the substantial potential enhancements in mass transfer obtained using the microbubbler. Approximately 80–90% of the CO_2 was transferred in the microbubbler compared to only 2% for the needle tip approach, a 45-fold improvement in CO_2 transfer and utilization. The needle tip fed 1,900 g of CO_2/g of biomass whereas the microbubbler only fed 2.9 g of CO_2/g of biomass, an almost 700-fold improvement.

Such an approach of using low flow rates with smaller bubbles for increased mass transfer can help provide significant cost savings by improving the efficiency of the transfer and limiting the amount of feed gas used (Table 6.2). The economic analysis for Table 6.2 takes into account the cost of gas to feed to a typical algae bioreactor, the volume of the reactor, the flow rate of the gas, and the fraction of gas transferred. Systems that have higher fractions transferred will require a lower flow rate of gas, potentially leading to a decrease in operating cost. From this analysis, the microfluidic bubbler is four times more cost efficient because of the lower requirement for feed gases. Furthermore, the savings of the microfluidic bubbler increase with larger systems and with extended use to suggest that this device will have value in a commercial setting. However, final costs must also consider start-up costs of a microfabrication facility and costs associated with pumping the gases through the microbubbler devices. The implementation of a clean room and equipment used for microfabrication include negative photoresists, developer solution, transparency mask, spin coater, mask aligner with ultraviolet (UV) lamp, and a tesla coil or oxygen plasma. The largest of these costs come from the costs for a clean room and a mask aligner with UV lamp. However, smaller, mobile clean rooms can be significantly less expensive, which can dramatically decrease the up-front manufacturing costs. However, once the equipment and clean room are in place, the cost of manufacturing the microfluidic bubblers is extremely low because the materials for making the devices (polydimethylsiloxane [PDMS] and cover slips) are inexpensive.

The benefits of increased mass transfer due to low flow rates and small bubbles help make this microfluidic bubbler a more efficient method of bubbling gases through a liquid. Carbon dioxide, oxygen, and other important gases, such as helium, can be sequestered from the gas phase by dissolving them into liquids more efficiently, providing environmental, cost, and efficiency benefits. A microbubbler also may be used for flocculation of microorganism cultures for more efficient harvesting[118]. This approach will allow users to harness and control gas delivery to liquids more effectively for a wide spectrum of engineering applications that could transform interfacial processing in the coming decades from advances in microfluidic technology.

6.5 Supplementary Materials and Figures

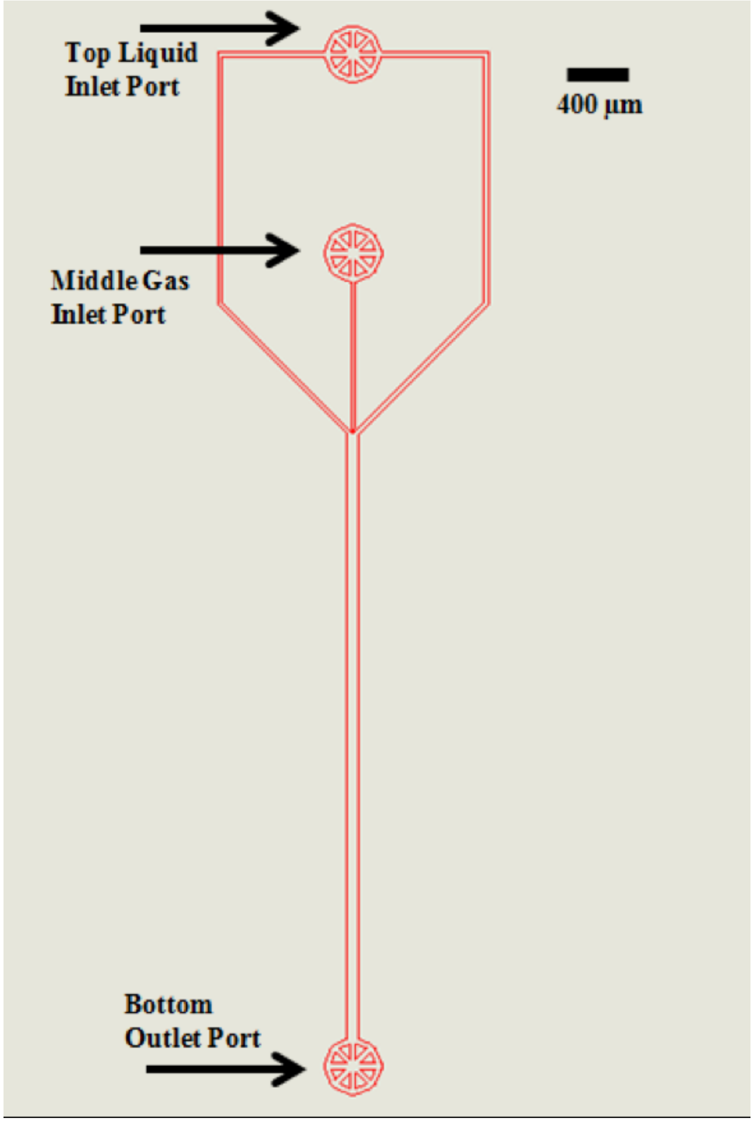

Supplementary Figure S6.1 Microfluidic bubbler channel and mask design. Liquid enters through the PDMS to the top port where it splits into two channels. The two liquid channels converge with the gas channel that enters at a different location. These channels combine to form bubbles that exit through the outlet port at the bottom.

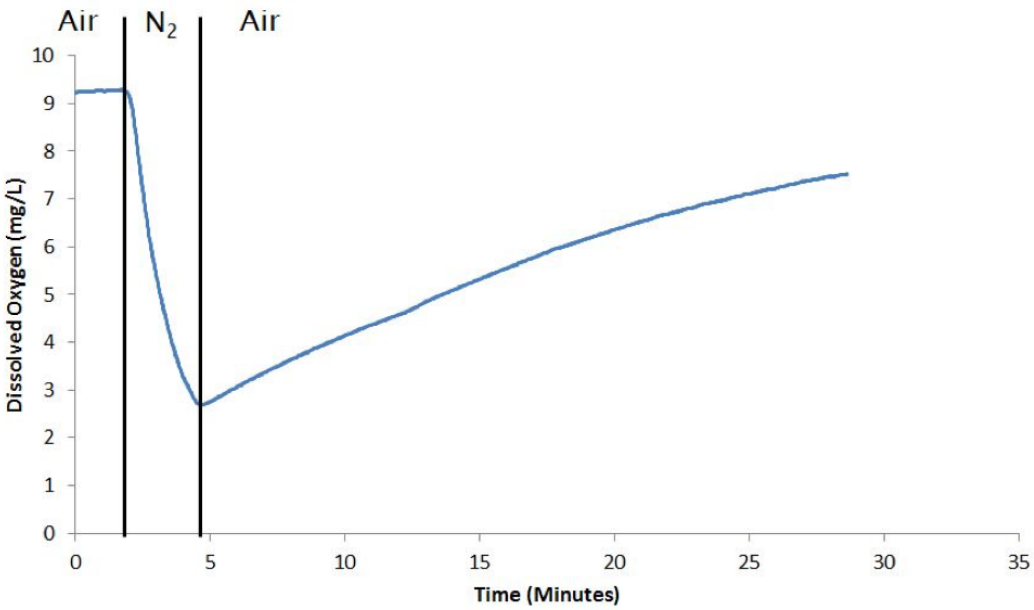

Supplementary Figure S6.2 Dissolved oxygen concentration over time for the calculation of K_La. Air is sparged into the system to obtain the baseline dissolved oxygen concentration, then nitrogen gas is sparged into the liquid to remove the dissolved oxygen. After the dissolved oxygen drops, air is fed back into the liquid and the increase in dissolved oxygen is recorded.

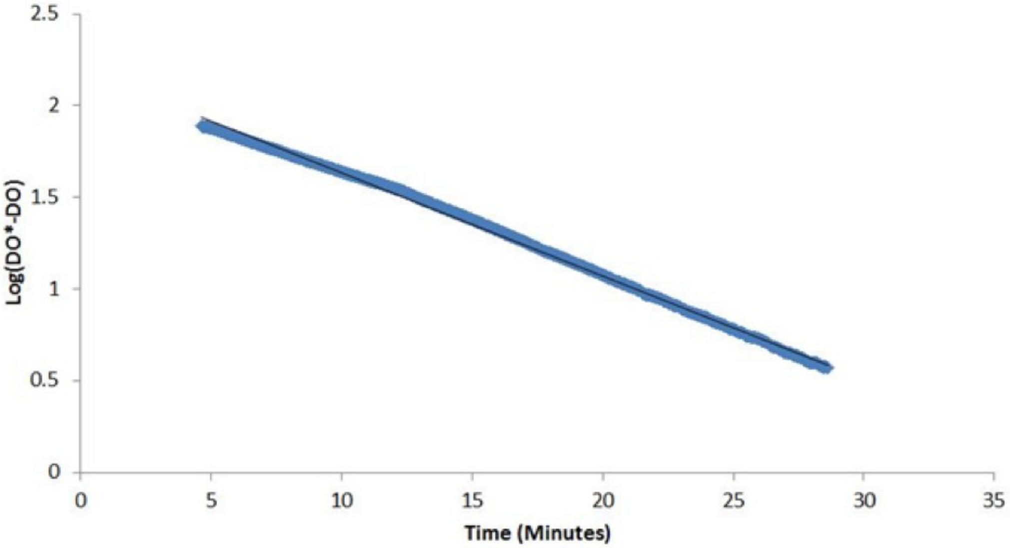

Supplementary Figure S6.3 Plot of the natural log of the saturation dissolved oxygen concentration minus the dissolved oxygen levels for the area of interest. The area of interest is the section when air is sparged back into the system after nitrogen gas. The K_La is calculated as the negative slope of the line.

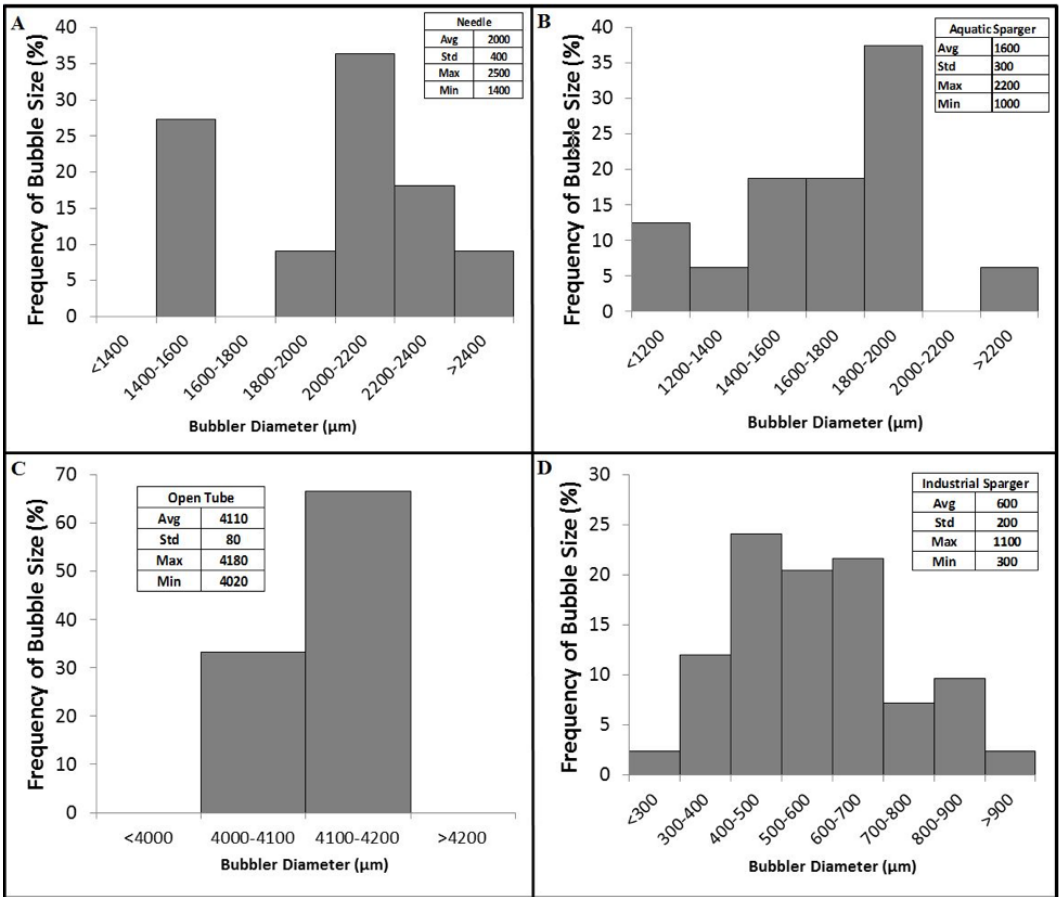

Supplementary Figure S6.4 Histogram of bubble distributions for other sparging methods. Figures show the distribution of bubble sizes along with average, standard deviation, minimum, and maximum for (a) needle, (b) aquatic sparger, (c) open tube, and (d) the industrial sparger.

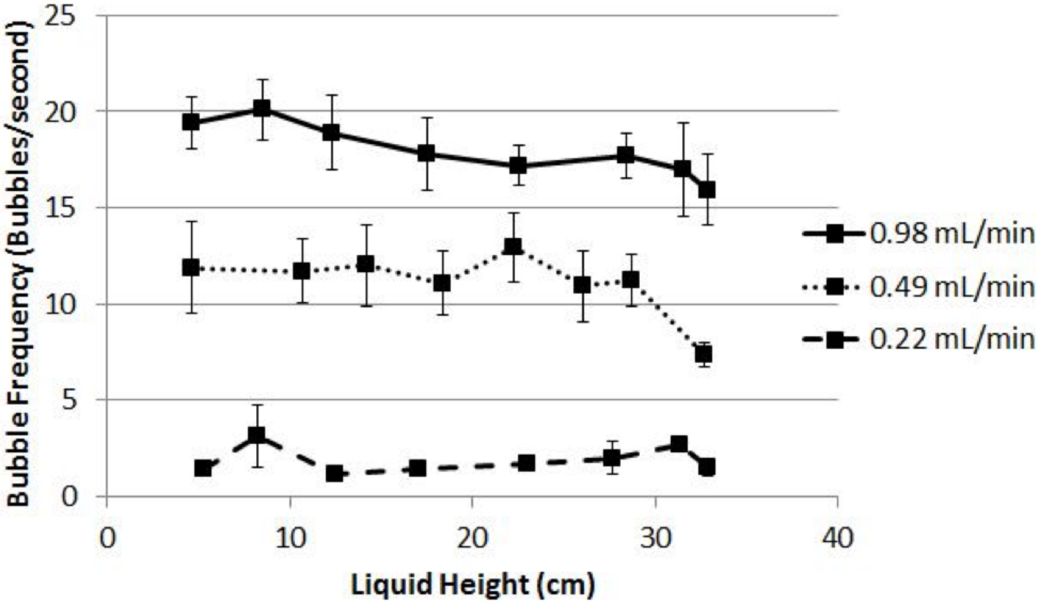

Supplementary Figure S6.5 Bubble frequency dependence on height of liquid for a range of flow rates. Bubble frequency stayed constant up to ~32 cm and increased with increased flow rates.

Reprinted with permission from Biotechnology and Bioengineering[119], copyright 2016, Wiley Periodicals, Inc.

Chapter 7

Label-free biomolecular detection at electrically displaced liquid interfaces using interfacial electrokinetic transduction (IET)

Biosensors require a biorecognition element that specifically binds to a target analyte, and a signal transducer, which converts this targeted binding event into a measurable signal. While current bio- sensing methods are capable of sensitively detecting a variety of target analytes in a laboratory setting, there are inherent difficulties in developing low-cost portable biosensors for point-of-care diagnostics using traditional optical, mass, or electroanalytical-based signal transducers. It is therefore important to develop new biosensing transducer elements for recognizing binding events at low cost and in portable environments. Here, we demonstrate a novel electrokinetic liquid biosensing method for the sensitive label-free detection of a model biomolecule against a background of serum protein. The biosensor is based on the motion of a microfluidic-generated electrical liquid interface when subjected to an external alternating current electrical field. We demonstrate that the electric field-induced motion of the interface can be used as a sensitive and specific transducer for the detection of avidin at femtomolar concentrations in solution. This new detection strategy does not require surface functionalization or fluorescent labels, and has the potential to serve as a sensitive low-cost method for portable biomarker detection.

7.1 Introduction

Biosensors combine targeted biological recognition with physicochemical transduction to detect specific biomolecules within a biological sample. They are used in a wide range of analytical applications, including diagnosis and treatment of infectious diseases, biowarfare detection[120,121], environmental monitoring[122,123], drug discovery[124,125], cell biology[126,127], cancer research[128,129] and point-of-care diagnostic testing[130,131]. Here, we address a key challenge to developing label-free homogenous biosensors for sensitive bio- molecular detection and kinetic analysis using microfluidic bio- sensing systems that normally require fluorescently labeled bio- molecules and optical quantification.

Combining biosensors with microfluidic transducers can fulfill an increasing demand for fast, inexpensive sensors capable of molecular detection and analysis. Microfluidic biosensors provide several advantages over traditional laboratory-based detection methods, including faster analysis time, reduced sample and reagent consumption, and potential automation with sample processing units using on-chip microfluidic valves[132], pumps, mixers[133] and detectors. In micro- fluidics, liquid transport usually occurs at low Reynolds number where the fluid flow is laminar; fluid streams flow side-by-side and mixing is driven only by diffusion[134-136].

Microfluidic liquid interfaces have been used as homogenous biosensing substrates for quantitative molecular detection and kinetic analysis in solution phase. The interface is created using laminar flow, where two streams combine at a fluidic junction and flow side-by-side down a main channel. One stream has a target probe and the second stream contains the biological sample of interest[137,138]. Biorecognition occurs in solution phase as the target and sample streams diffusively mix at their contacting liquid interface where target and sample molecules specifically bind to one another. This approach offers an inexpensive, yet extremely powerful method for biosensing and biomolecular kinetic analysis, and has been used to quantify fast kinetic processes, extract kinetic rate constants, perform sensitive on-chip immunoassays and detect DNA hybridization reactions in solution.

To create a complete biosensor, the microfluidic interface is coupled with a transducing element to convert recognition events into a detectable measurement signal. Depending on the nature of the transduced biosensor signal, detection can be performed optically[139], electrically[140,141], or mechanically[142].

Biosensing at microfluidic liquid interfaces, however, is currently only performed using optical methods such as fluorescent microscopy, fluorescence energy transfer (FRET) [143], fluorescence correlation spectroscopy[144], confocal fluorescent microscopy[145], and fluorescence lifetime imaging microscopy (FLIM) [146]. While effective, they require fluorescently labeled probe molecules and optical components, which can significantly increase the cost and size of the microfluidic platform.

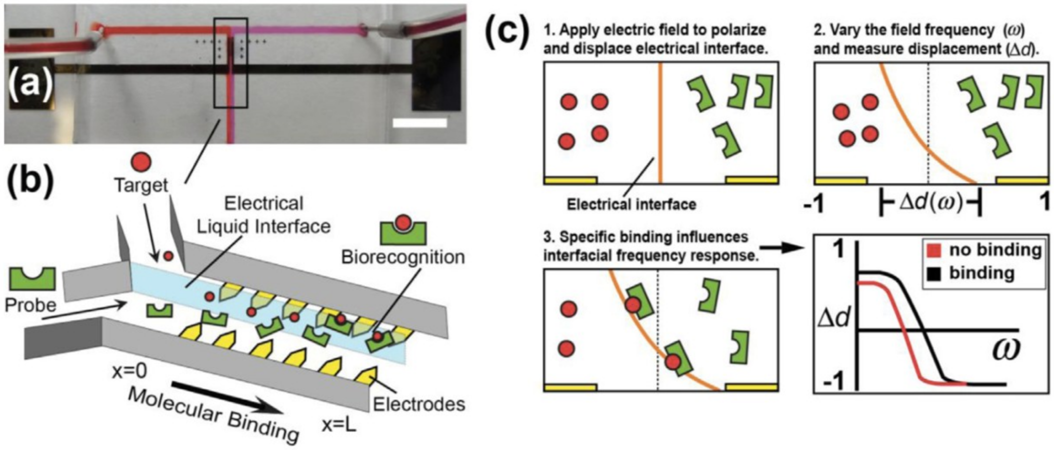

Figure 7.1 Biosensing T-channel schematic. (a) Microfluidic T-channel device with integrated electrodes used to create an electrical liquid interface for the IET sensor. Scale bar 5.0 mm; (b) schematic illustration of target-probe binding along the liquid interface; and (c) principles of IET sensor operation – (1) specific binding occurs at the electrical interface; (2) an electric field polarizes and displaces the interface a distance Δd, which is a function of the field frequency; (3) binding influences the polarizability of the interface and is detected by measuring interface frequency response at different values of field frequency.

We report a label-free homogeneous electrokinetic biosensor for detecting and quantifying bioaffinity interactions in solution. Our approach combines continuous microfluidic flow with alternating current (AC) electrokinetics. Electrokinetics integrates well with microfluidics and is a useful tool for a variety of on-chip fluidic applications including cell manipulation[147,148], liquid mixing[149], particle trapping [147,148] and fluidic routing[150]. In our electrokinetic approach, depicted in Figure 7.1, bioaffinity binding occurs at a microfluidic liquid interface. We create the interface using a microfluidic T-channel device with two fluid inlets and a single fluidic outlet; two fluids combine at the channel junction and create an interface as they flow side-by-side down the main channel to the outlet (Figure 7.1(a)). An array of microelectrodes is fabricated in the main flow channel and used to deliver a polarizing electric field across the fluid interface. To be polarizable, and capable of being manipulated with the applied electric field, we engineer an electrical mismatch into the interface. In this way, the interface is an electrical interface (EI), comprised of two co-flowing fluid streams with different electrical conductivity (σ) and permittivity (ε). Using the EI as a substrate for biomolecular reaction, two solutions – one containing a target protein and the other containing an analyte probe – are pumped into separate T-channel inlets at a constant flow rate, inter-diffuse across the EI and specifically bind at the liquid interface (Figure 7.1(b)). During this process, an AC electrical field is applied across the EI. Due to the large electrical mismatch, the interface polarizes and electro- kinetically displaces across the main flow channel, perpendicular to the main flow direction (Figure 7.1(c)) [151]. The magnitude and direction of this displacement is proportional to the electrical mismatch at the EI. Here, we demonstrate that specific biomolecular interactions influence this mismatch, and allow for biomolecular interactions to be detected and quantified without fluorescent labels by measuring the interfacial displacement under an external electric field during binding (Figure 7.1(c)).

Our label-free biosensing method uses the liquid interface as a homogenous substrate for specific binding, and its motion in an AC electric field as the transducer for biomolecular recognition. We therefore propose a new class of biosensors based on interfacial electrokinetic transduction (IET): specific binding changes the electrical properties at the EI, which is electrokinetically transduced and detected by measuring perturbations in field-induced fluid displacement.

In this work, we demonstrate how to use IET to monitor avidin–biotin binding kinetics in real-time without labels. Moreover, the IET biosensor is specific and sensitive, and able to detect as low as 250 femtomolar avidin concentrations against a 5mg/mL background of bovine serum albumin (BSA). Through this study, we establish a methodology for rapid label-free IET biosensing at electrical liquid interfaces, demonstrate sensor performance and sensitivity for the detection of biomolecules, and measure avidin– biotin binding kinetics with millisecond time resolution. This new electrokinetic sensor can provide a low-cost, rapid, and portable biosensing system for label-free real-time kinetic analysis and on- site biomolecular diagnostics in free solution.

7.2 Materials and methods

7.2.1 Microfluidic device fabrication

Experiments were performed using the microfluidic T-channel device shown in Figure 7.1(a). It was fabricated using standard soft photolithography and microfabrication techniques. First, micro- channel electrodes were fabricated using wet chemical etching. Glass cover slips (50 30 mm2, No. 1, Fisher Scientific) were coated with 20 nm of chromium and 50 nm of gold using electron beam evaporation. The cover slips were patterned with photo- resist (Shipley 1813) and exposed metal was etched using gold and chromium etchant creating an array of patterned metal electrodes. The microchannel was fabricated in PDMS (Momentive, RTV 615A). A 10:1 mixture of PDMS elastomer and curing agent was poured atop the wafer and baked at 85 °C for 50 min. The PDMS was gently peeled off the wafer and fluid ports were punched with a 0.75 mm diameter biopsy punch (Ted Pella, Inc.). The PDMS microchannel and electrode pattern were then exposed to oxygen plasma (Jelight, Model 42A) and immediately aligned and sealed under an inverted microscope. As shown in Figure 7.1(a), the device consists of a main flow channel 100 μm wide and 65 μm high. The embedded electrodes are axially separated by 20 μm and symmetrically bridge the channel width with a total length of 2.0 mm. Electrodes with sharp points are utilized in order to maximize the electric field strength across the liquid interface, as the sharp point serves to focus the electric field to the tip of the electrode.

7.2.2 Sensor measurement

The electrical interface was created using the microfluidic "T- channel". Two fluid streams were introduced into the device via pressure driven flow using an externally pressurized cryogenic vial. Shown in Figure 7.2(a), the left-most (red) high conductivity stream consists of a 0.5 M phosphate buffered saline, pH 7.4, (PBS) solution with 10 ng/mL of Alexa Fluor 594 (Invitrogen). The right-most (purple) high dielectric stream consists of 0.8 M 6-aminohexanoic acid (Sigma-Aldrich) (AHA) labeled with 10 ng/mL of Alexa Fluor 647 (Invitrogen). AHA is a water-soluble zwitterion used for increasing the dielectric constant of aqueous solution. Prior to fluorescent labeling, the AHA solution is spun down in a centrifuge for 15 min in 1 g/mL Dowex MR-3 (Sigma) ion exchange resin to remove trace salts and reduce solution conductivity[2]. A cross-sectional view of the resulting fluid interface was imaged using dual excitation confocal microscopy (Figure 7.2(b)).

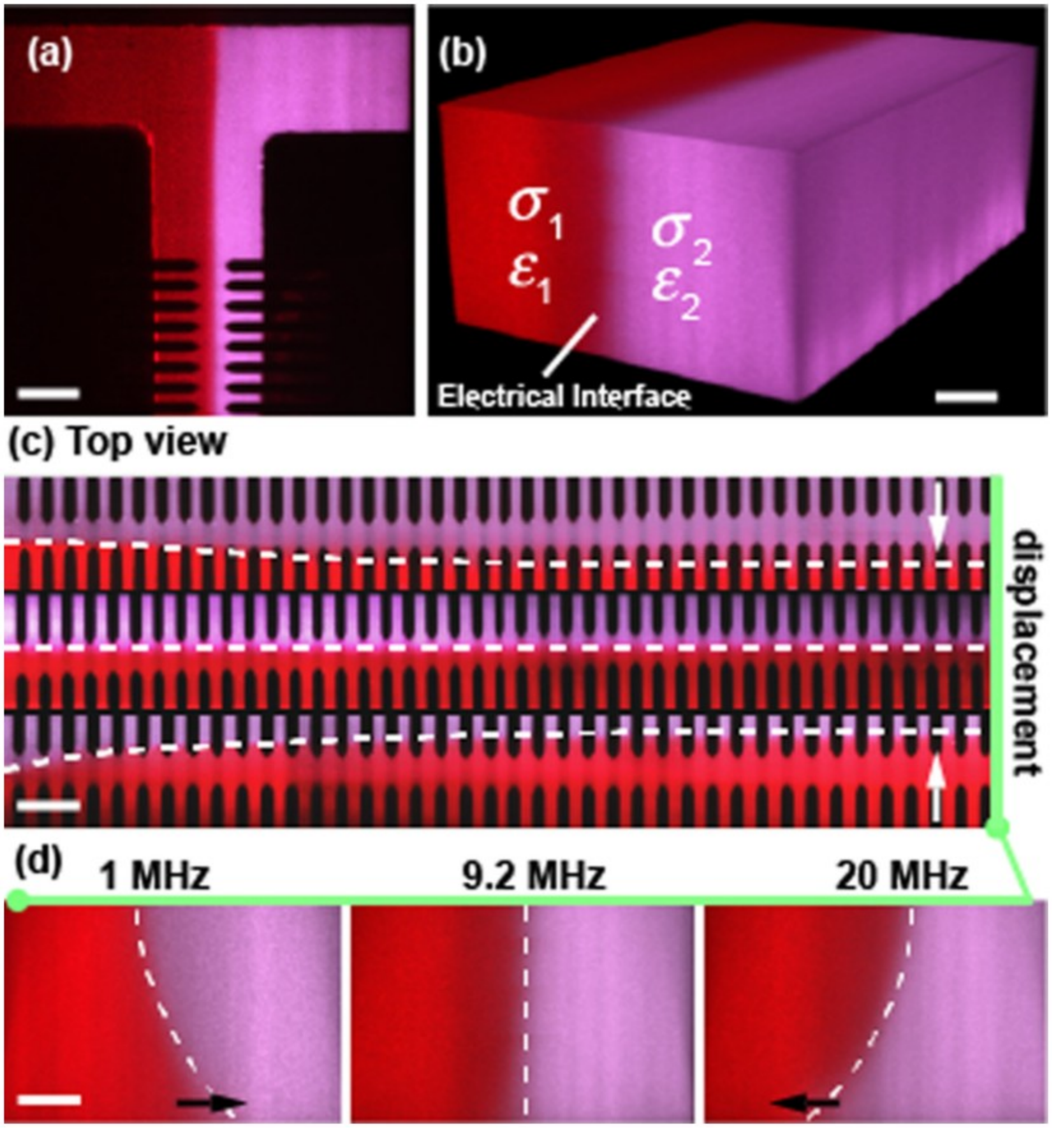

Figure 7.2. Confocal displacement micrographs. (a) Confocal micrograph of two fluorescently labeled fluids flowing side-by-side to create a liquid interface. Scale bar 50 µm; (b) 3D confocal image stack of the electrical interface formed between to fluids with different electrical conductivities and dielectric constants. Scale bar 20 µm; (c) the interface enters the electrode array and displaces across the flow channel. The direction of this displacement is dependent on the frequency of the applied electric field. Scale bar 50 µm; and (d) confocal micrograph illustrates a side-view of the interface at different electric field frequencies. Scale bar 20 µm. (For interpretation of the references to color in this figure legend, the reader is referred to the web version of this article.)

To create the electrical interface two fluid streams, each with a different set of electrical properties, are pressure injected into the microfluidic device. An AC potential of 10 V peak-to-peak (Vpp) at a frequency of 1 MHz was dropped across the electrodes, and slowly is increased to 20 MHz while continuously monitoring the displaced position of the fluid interface.

7.2.3 Protein solutions

Biotin, avidin, bovine serum albumin, and mouse anti-bovine serum albumin were purchased from Sigma Aldrich, USA, and used as received. A 16 μM biotin solution was made by diluting a 4 mM stock with AHA and labeled with 10 ng/ml Alexa Fluor 594, and pH adjusted to 7.4. The avidin solution was made by adding powdered avidin to PBS labeled with 10 ng/ml Alexa Fluor 647. The conductivity of the PBS solution was adjusted to 0.25 mS/cm using DI water. All subsequent solution avidin concentrations were made by serial dilutions with a stock dilute PBS. The final avidin con- centration was calculated using a UV spectrometer (Thermo Scientific Genesys 10S).

7.2.4 The electrical interface

IET biosensors are bioaffinity sensitized electrical liquid inter- faces that electrokinetically displace in response to biomolecular binding. They require both microfluidic and electrokinetic components. The electrical interface is created using a PDMS micro- fluidic T-channel. An AC electric field is generated using an array of co-planar gold microelectrodes lithographically patterned onto the surface of a glass slide. The PDMS-electrode assembly is aligned under an optical microscope and plasma bonded to create a complete electro-fluidic device (Figure 7.1(a)). The EI is composed of two co-flowing electrolyte streams. Both streams – streams 1 (left) and 2 (right) – have finite electrical conductivity and permittivity, but one has a greater electrical conductivity and the other a greater electrical permittivity such that $\sigma_1 > \sigma_2$ and $\varepsilon_2 > \varepsilon_1$. Because the streams do not mix except by diffusion, a sharp electrical mismatch is created at their co-flowing interface, which can be polarized (e.g. charged) and displaced across the microchannel using a perpendicular AC electric field.

7.2.5 Measuring interfacial frequency response

To quantify displacement, the interface position is imaged using confocal microscopy; each stream is labeled with a different fluorescent marker – Alexa Fluor 594 (red) or 647 (purple) – and imaged, yielding top-down 2D (Figure 7.2(a)) and 3D (Figure 7.2(b)) micrographs of the interface and its position within the microchannel. When a perpendicular AC electric field is applied, the interface displaces across the channel in a direction and magnitude de- pendent on the field frequency (ω). This displacement response can be confocal imaged and quantified from a top-down and side view. Figure 7.2(c) shows a top-view of the EI displacement over the length of the electrode array for three different applied frequencies: ω = 1 MHz, 9.2 MHz, and 20 MHz. At a frequency of 1MHz (Figure 7.2(c)-bottom), the interface enters the array and continuously displaces across the main flow channel into the high permittivity flow stream. At high frequency (20 MHz), the displacement direction reverses (Figure 7.2(c)-top). At an intermediate crossover frequency (COF) of 9.2 MHz, the interface does not displace in the electric field and remains stationary over the entire length of the array (Figure 7.2(c)-center).

The force driving interface motion is a surface force that exists over the separation length scale between the electrodes in the array. Because this length scale (20 μm) is smaller than the microchannel height (100 μm), field-driven displacement is localized to the bottom of the microchannel. Fluid near the top of the channel is driven in the opposite direction to satisfy conservation of mass, and the interface appears to tilt to the left or right depending on the applied field frequency. Figure 7.2(d) shows the side-view of the displaced tilted interface for each applied field frequency.

In this work, we propose to use the frequency response of the interface as a biosensing transducer for detecting biomolecules at a microfluidic liquid interface. To accomplish this, we measure the net displacement of the EI as a function of applied electric field frequency at the bottom surface of the microchannel. Figure 7.3(b) shows the complete frequency response of the interface calculated from the micrograph experiment presented in Figure 7.2. The displacement (Δd) has been rendered non-dimensional over the microchannel width, and varies from –1 to 1. At the COF, the interface does not displace: Δd = 0. Above and below the COF the displacement is finite and varies in both direction and magnitude with the applied frequency.

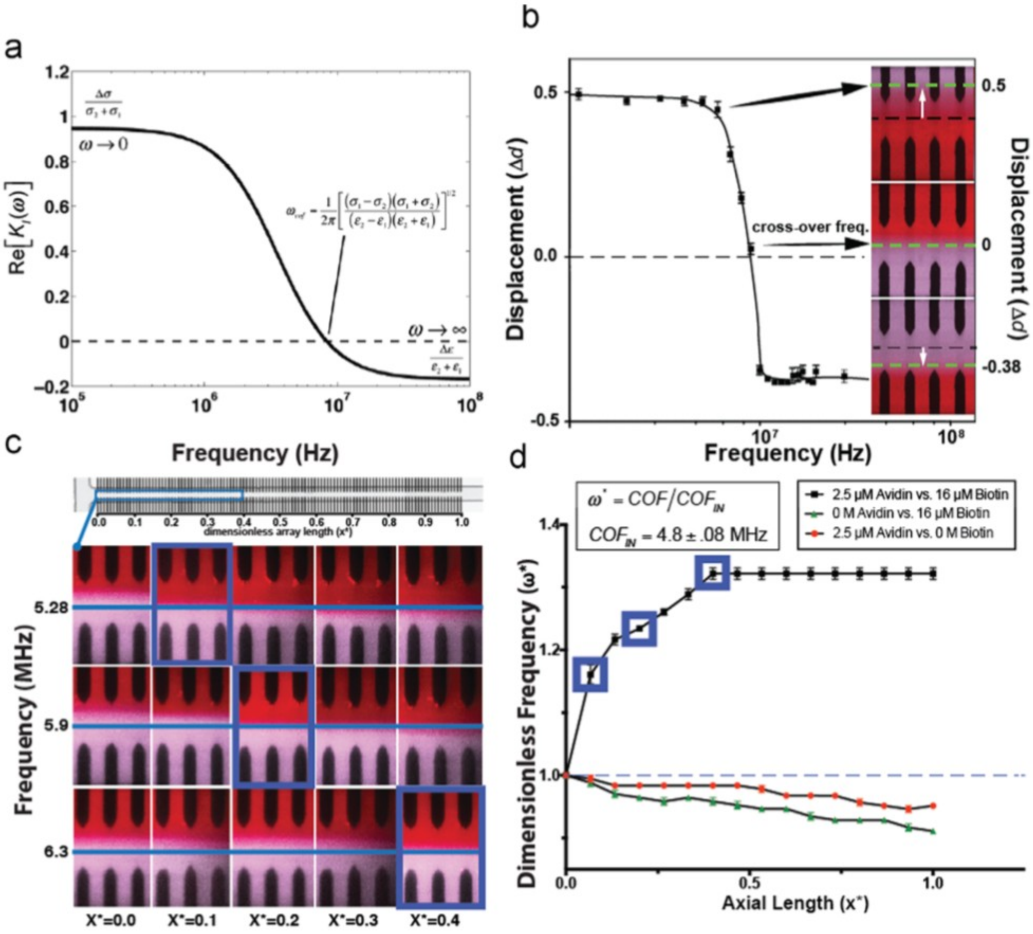

Figure 7.3 Electrical and reaction influence on displacement and dimensionless frequency. (a) Liquid interface polarization [Eq. (1)] plotted as a function of field frequency. Low frequency polarization is driven by differences in electrical conductivity, while the interfacial dielectric constant governs the polarization of the interface at high frequency. A cross over frequency [Eq. (2)] is dependent on both interfacial conductivity and dielectric constant. The crossover frequency

increases during biomolecular binding. (b) Dimensionless interface displacement measured at different electric field frequencies. An optical micrograph highlights interface position at low (1 MHz), intermediate (9.2 MHz) and high (20 MHz) field frequencies; (c) optical micrographs of the electrical interface captured at different positions and electric field frequencies along the length of the electrode array. The interface crossover for each axial position is highlighted in blue and plotted in the adjacent figure; and (d) IET sensorgram showing the influence of binding on interface crossover frequency plotted against two biosensor negative controls. (For interpretation of the references to color in this figure legend, the reader is referred to the web version of this article.)

7.2.6 Electrokinetics of an electrical interface-fluidic dielectrophoresis

The motion of an electrical liquid interface in an externally applied AC electric field is known as fluidic dielectrophoresis (fDEP) [2]. Despite being discovered over six decades ago for particle suspensions[152], dielectrophoresis has only recently been applied to aqueous liquid interfaces. Here, we theoretically define the electrical and frequency dependence on the interface displacement, and apply this to our IET biosensor measurements.

For an EI subjected to a time varying monochromatic AC electric field, the magnitude and direction of the interfacial displacement is directly proportional to the interface polarization factor: $K(\omega)$. This factor describes the magnitude and sign of the field-induced ionic and dielectric charge that is induced at the EI in response to the electric field. Because the field oscillates monochromatically in time, the sign and magnitude of charge at the interface is dynamic, and reverses in phase with the electric field. This process takes a finite time, and depending on the field frequency, not all of the induced charge will be able to dynamically stay in phase. To account for this phase lag, $K(\omega)$ is a complex function with both real and imaginary parts, dependent on field frequency, and liquid conductivity and permittivity differences across the EI. Displacement is driven by the real part of this expression (i.e. interface charging that is in-phase with the applied field). The out of phase (imaginary) part produces a net interfacial electric stress with a zero time-average and does not contribute to interfacial motion. Therefore, we use the real part of the polarization factor in this work.

For an electrical interface composed of two co-flowing aqueous electrolytes with different electrical conductivities and permittivities, the real part of the interfacial polarization factor is

$$Re[K(\omega)] = \frac{((\varepsilon_2-\varepsilon_1)\tau^2\omega^2)}{((\varepsilon_2+\varepsilon_1)(\tau^2\omega^2+1))} + \frac{((\sigma_2-\sigma_1)\tau^2\omega^2)}{((\sigma_2+\sigma_1)\tau^2\omega^2+1)}, \tag{7.1}$$

where $\tau = (\varepsilon_2+\varepsilon_1)/(\sigma_2+\sigma_1)$ is the characteristic charge relaxation timescale at the interface between the two liquids.

Illustrated in Eq. (1), fDEP provides a unique method for quantifying the electrical properties of an EI because displacement direction and magnitude are both dependent on the relative electrical property mismatch between the interface's two co-flowing fluid streams. In Figure 7.3(a), we plot Eq. (1) as a function of electric field frequency, and highlight the influence of electrical conductivity and permittivity mismatches at high, intermediate, and low AC field frequencies. At low frequency below the COF, polarization is driven by differences in electrical conductivity between the two co-flowing fluids ($\sigma_1 - \sigma_2$), which we define here as interfacial conductivity (Δσ). Above the COF at high frequency, displacement is governed solely by interfacial permittivity (Δε). The COF (ω_{COF}) occurs where the net polarization and displacement of the interface is zero (Figure 7.3(b)). It is sensitive to both interfacial conductivity and permittivity, shown here by setting the polarization factor equal to zero (*Re[K(ω)]*=0), and solving for frequency:

$$\omega_{cof} = \frac{1}{2\pi}\left[\frac{(\sigma_1-\sigma_2)(\sigma_1+\sigma_2)}{(\varepsilon_2-\varepsilon_1)(\varepsilon_2+\varepsilon_1)}\right]^{1/2}. \tag{7.2}$$

Depicted in Figure 7.3(a), interface displacement at low and high frequency is influenced only by interfacial conductivity and permittivity, respectively, and the COF is a function of both properties.

The transducing element of our IET biosensor is based on the interface COF. First, because the interface COF is influenced by both EI conductivity and permittivity, it is a single frequency measurement capable of monitoring both of these properties simultaneously at a liquid interface. Second, because the COF occurs when interfacial displacement is zero, it is a simple measurement to observe, and can be made at any axial position along the length of the electrode array.

7.2.7 Using interfacial crossover frequency to detect specific binding

To detect specific binding at a liquid interface, the EI is sensitized with target probe molecules and forced to flow adjacent to a sample stream containing an analyte. With developed and continuous flow down the T-channel, the fluid at each axial position within the main channel has a different average residence time, and the binding process will be at different time points of diffusive-reactive transport. To monitor binding dynamically during this process, the COF at the EI is quantified at discrete axial positions down the length of the main flow channel. Changes in EI electrical properties during binding influence the COF. Because specific binding progresses forward in time as fluid flows down the length of the array, biomolecular binding can be electrokinetically quantified in time by measuring the COF at varying positions in axial space down the channel length.

7.3 Results and discussion

7.3.1 The IET biosensor sensorgram

Our IET biosensor signal was the COF of the liquid interface. We performed this measurement at discrete positions over the entire axial length of the microelectrode array to detect biomolecular binding dynamically in time. We used biotin–avidin as the model system for studying the biosensor response. Avidin binds up to four molecules of biotin with high specificity and affinity, and is a useful binding model for characterizing biosensing systems. To more clearly compare sensor performance against different concentrations of avidin, both experimental variables – the COF and the array position – were rendered dimensionless. Shown in Figure 7.3(c), the electrode array was rendered dimensionless by its total length (2.0 mm); COF measurements were quantified along a dimensionless axial variable x*, spanning the domain {0,1}. To maintain consistent reaction residence times within the electrode array, the fluid flow rate was fixed at 5.0 μL/min. We performed all min biosensing experiments using buffers with constant conductivity and permittivity. Because these properties were constant, the COF at x* = 0 was fixed: $\mathrm{COF}_{\mathrm{IN}}$ = 4.8 MHz ± 1%. To track the evolution of the COF over the axial position of the array, the COF was rendered dimensionless (ω*) by $\mathrm{COF}_{\mathrm{IN}}$ such that ω* = 1 at x* = 0.

To determine if specific avidin–biotin binding influences the COF of the interface, a COF sensorgram was captured using 2.5 μM avidin flowing adjacent to 16 μM biotin. We used two negative controls for this experiment – one COF sensorgram was taken without biotin, and a second without avidin. Finally, we measured the COF sensorgram along the EI within the electrode array with both avidin and biotin. Figure 7.3(d) shows the ω* vs. x* sensorgram from each experiment. In the absence of binding, the interfacial COF decreases by ~8% over the microchannel length. During avidin–biotin binding, however, the interface

COF increases by over 30%, reaching an equilibrium value of $\omega^* = 1.3$ at a distance $x^* = 0.4$ down the array.

The polarized interface behaves as a biosensor transducer; specific binding influences the interfacial electrical properties, which are transduced electrokinetically as a change in COF for a given position down the electrode array. The COF changes dynamically, transducing biomolecular binding events over axial length as they proceed forward in time. This concept is reflected in the sensorgram data (Figure 7.3(d)), where the COF appears as a binding curve, increasing over the array length and plateauing as the re- action saturates at the EI. The transduction properties of the EI can be observed optically, as depicted in the confocal micrographs shown in Figure 7.3(c). As the field frequency is increased, the axial position where no interface displacement occurs shifts. The COF at $x^* = 0.1$, for example, is 5.28 MHz; no displacement is observed at this point in the array. This frequency is above COF_{IN} (4.8 MHz) at $x^* = 0$ and below the COF for any position where $x^* = 0.1$, so the interface deflects in opposing directions surrounding this inflection point. As the applied frequency is increased, the position of the inflection point shifts, corresponding to a new position-dependent COF. These COF inflections are highlighted with blue boxes in Figure 7.3(c). They represent COF measurements for three axial positions within the electrode array, and correspond to the sensorgram data points emphasized with square boxes in Figure 7.3(d).

7.3.2 Avidin–biotin binding influences interfacial conductivity

The response of the IET sensor is based on the influence of bioaffinity binding on the interfacial electrical properties at the EI. Because the COF is sensitive to both interfacial conductivity and permittivity, COF measurements are not enough to determine the exact electrical influence that biomolecular binding has on the interface. To determine how binding influences the electrical properties across the interface, we measured the net displacement during binding over varying AC field frequency at the saturation position x* = 0.4 down the electrode array. Figure 7.4(a) shows interfacial displacement spectrum as a function of field frequency for three different avidin concentrations: 0 nM, 25 nM, and 2.5 μM. The electrical mismatch of each of the fluids containing both avidin and biotin were held constant for each experiment. As shown above in Figure 7.3(a), low frequency displacement is dependent solely on the interfacial conductivity and depends only on interfacial permittivity at high frequency. From the spectra presented in Figure 7.4(a), avidin–biotin binding influences the low frequency displacement measurements – displacement increases with avidin concentration. At high frequency, however, interfacial displacement remains constant and is not influenced by interfacial binding. Figure 7.4(b) shows a series of confocal micrographs depicting this observation. At 1 MHz the displacement increases as avidin concentration increases (Figure 7.4(b) – Left), and high frequency (20 MHz) displacement remains unaffected with binding (Figure 7.4(b) – Right).

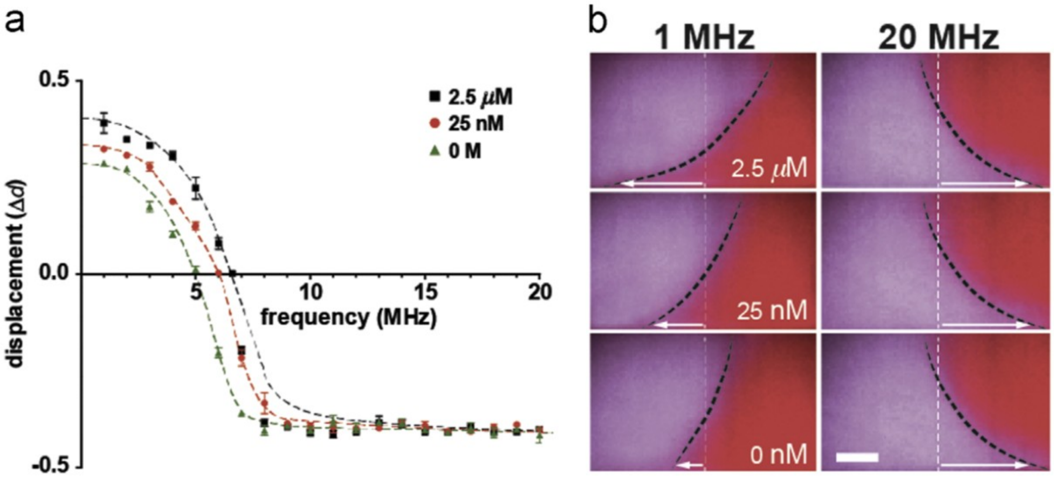

Figure 7.4 Effects of biotin-avidin binding on interfacial displacement. (a) Interface displacement measured over increasing concentrations of avidin: 0 M, 25 nM, and 2.5 μM. (b) Confocal micrographs illustrate interface position at low (1 MHz) and high (20 MHz) for increasing avidin concentrations. Scale bar 20 μm.

The displacement measurements in Figure 7.4 demonstrate that the biomolecular binding of avidin–biotin increases the interfacial conductivity (Δd increases at low frequency with binding), but not alter the interfacial permittivity (Δd remains unaffected at high frequency). While fDEP can give insight as to how the interface is being influenced electrically, it cannot currently provide any mechanistic information about why this increase is occurring. The increase in interfacial conductivity may be due to counterion release during binding. One possibility is that a diffuse layer of spatially confined counterions surrounds the charged proteins in solution. During binding, ions are released, which could potentially increase the electrical conductivity in the vicinity of the interface, and produce an increase in COF. Another possibility could be due to a change in electrophoretic mobility due to the negative charge of the bound biotin molecule, which would make the complex a more effective charge carrier at the interface. Currently, however, the precise physical mechanism for the interfacial conductivity increase remains unknown.

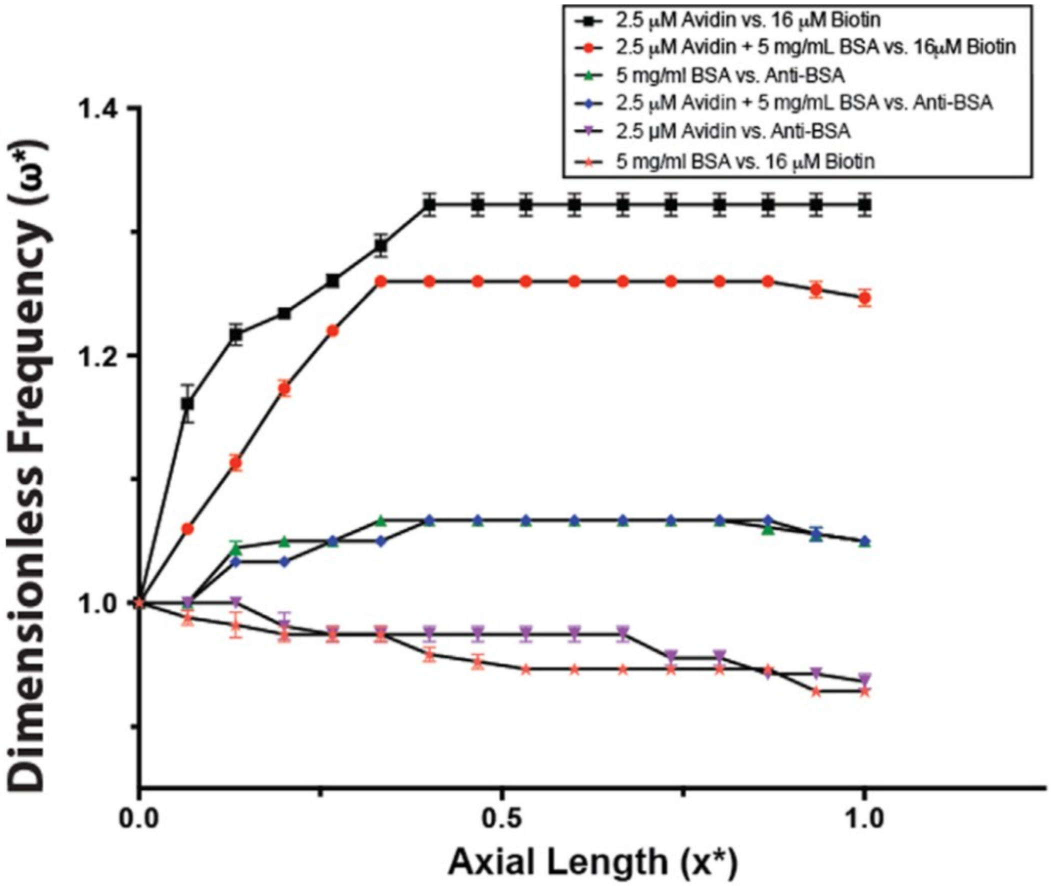

Figure 7.5 IET sensorgram illustrating selective sensor response to both BSA/anti-BSA and avidin/biotin binding.

7.3.3 Selective and specific biosensing in a BSA background

Surface-based heterogeneous biosensors can suffer from non-specific adsorption of background proteins, which can reduce sensor sensitivity. The IET sensor utilizes a liquid interface as a biorecognition substrate, and therefore is much less prone to suffer from biofouling or non-specific adsorption of proteins to the sensor surface. However, background interference from non-specific proteins is a major concern when working with real-world clinically relevant samples. To investigate sensor performance in the presence of an abundant background protein, we challenged the sensor with 5 mg/mL of bovine serum albumin (BSA). In order to be able to compare our findings with the avidin–biotin experiments performed without a background (Figure 7.3(d)), the inlet COF and microchannel flow rate were held to less than a 1% deviation from their previous experimental values. Shown in Figure 7.5, the COF increases about 25% over the length of the array when taken with 2.5 μM avidin flowing adjacent to 16 μM biotin in the presence of a serum background. To investigate the ability to design specific bioaffinity response into the EI, we removed avidin from the sample stream and replaced it with a 100 nM concentration of anti-BSA. Shown in Figure 7.5, the sensor responds to the presence of BSA instead of avidin. Two control experiments were performed to ensure these measurements were specific – removal of anti-BSA and avidin from the sample stream does not produce an increase in the COF along the length of the array.

There are several important features to note regarding the sensor performance depicted in Figure 7.5. First, as shown, when compared to the sensorgram without BSA, the selectivity of the sensor towards avidin in the presence of serum decreases by 30%. This decrease could be due to several factors. There is a possibility that non-specific charge–charge interactions[153] between BSA and the surrounding biomolecules in solution could be influencing the interfacial conductivity and total concentration of avidin available for binding. However, as shown in the BSA sensorgram in Figure 7.5, the addition of background avidin to the BSA solution during binding with anti-BSA does not affect the magnitude of the sensorgram. This suggests that non- specific interactions between BSA and avidin are minimal.

Because the sensor COF is driven by a combination of both target–receptor binding and interfacial smoothening by ionic diffusion, we speculate that the addition of BSA hinders the rate of avidin diffusion towards and across the interface, which slows the rate of the binding and leads to a lower sensor COF. Finally, it is worth noting that the reaction between BSA and anti-BSA does not produce the same change in COF when compared to the avidin and biotin reaction. We hypothesize this difference is due to the difference in binding kinetics between these two reactions. In comparing the K_d of each reaction, 10^{-15} and 10^{-4}, for the avidin– biotin and BSA–anti-BSA[154] reaction, respectively, the reaction between BSA and anti-BSA occurs at a slower rate than that of avidin and biotin. Since the reaction time is slower, binding requires a longer distance down the axial length of the microchannel. Because the diffusion of ions across the electrical interface is constantly occurring and decreasing the interfacial conductivity, the reaction requiring a greater length scale must compete with an ever-decreasing interfacial conductivity, which ultimately leads to a smaller magnitude in the change of COF. Future work will focus on developing a better understanding of these physicochemical mechanisms that link species reaction and diffusional rates with interfacial conductivity in order to better optimize sensor response.

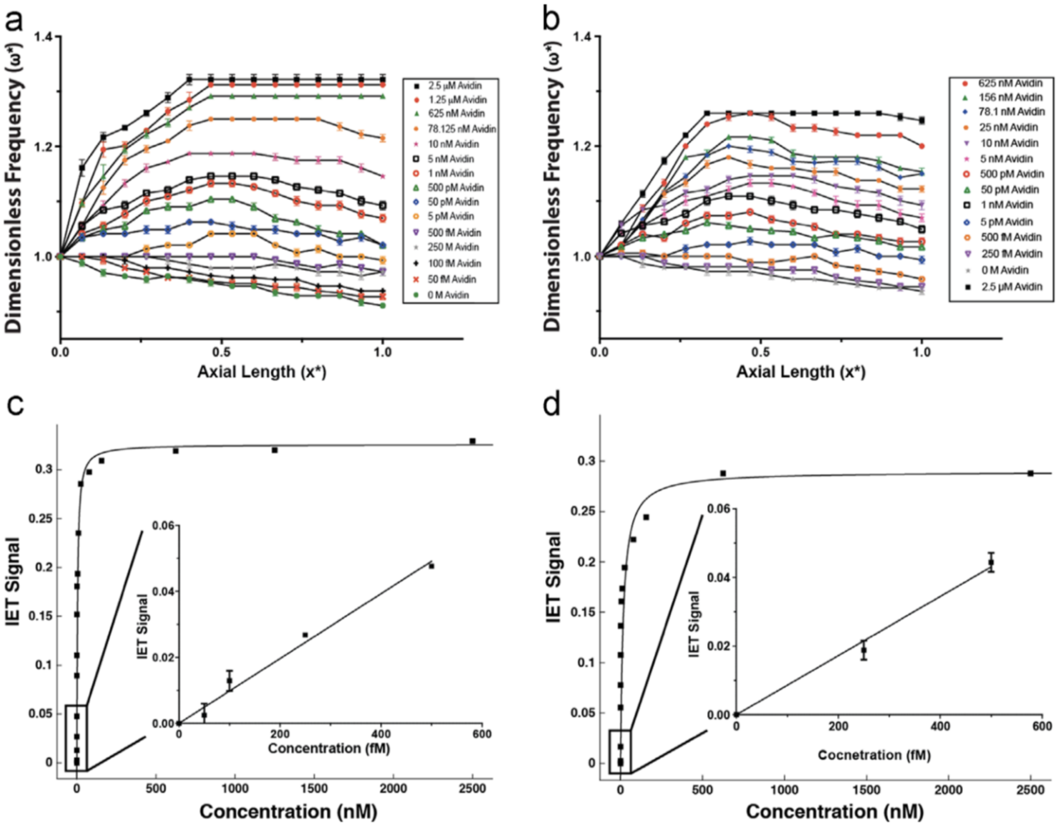

Figure 7.6 IET sensorgrams and binding curves. (a) IET sensorgram of increasing concentrations of avidin; (b) sensorgram illustrating sensor response against a background of serum albumin; (c) sensor binding curve showing IET limit of detection without a BSA background; and (d) with a BSA background.

7.3.4 Label-free femtomolar detection in BSA

We next performed a series of experiments to determine the IET sensor's limit of detection (LOD) and how the IE performs as a transducer against an abundant background protein (5 mg/mL BSA). The IET biosensor response was measured as a function of avidin concentration, ranging from 50 fM to 2.5 μM, both with and without BSA. Figure 7.6 shows a series of sensorgrams for avidin–

biotin binding at the EI (Figure 7.6(a)) and with a BSA background (Figure 7.6(b)). The net IET sensor response increases with avidin concentration, and eventually levels to a constant value some distance down the electrode array. The eventual leveling of the IET signal at a given position down the array length can be attributed to the saturation of the interface with bound avidin–biotin complex; avidin is depleted from the local EI and the sensor response saturates.

The magnitude of each saturated sensorgram response at a fixed distance down the electrode array ($x^* = 0.5$) was isolated and plotted as a function of avidin concentration. The resulting calibration curve is shown in Figure 7.6(c) for an EI without BSA and in Figure 7.6(d) for the interface subjected to a serum background. For each analytical curve, the sensor exhibits a linear response with increasing concentrations of avidin up to 500 fM, as shown in the subplots of each (Figure 7.6(c) & (d)). Beyond this linear concentration range, the sensor deviates and begins to level off, eventually saturating at an avidin concentration at approximately 1 μM. The concentration LOD was calculated using the 3-sigma method ($S/N = 3$) for each binding curve. Without background BSA, the sensor LOD was 209 fM, while the addition of BSA decreased sensor sensitivity with a corresponding LOD of 626 fM.

7.4 Conclusions

In this work, we presented a sensitive and selective label-free electrokinetic biosensor for detecting biomolecules at electrically polarizable liquid interfaces. Biomolecular binding occurs at the diffuse electrical interface formed between two co-flowing microfluidic laminar streams with different electrical properties. The biosensor approach is based on measuring the electrical field-induced displacement frequency response of this interface, which is sensitively influenced by specific biomolecular binding. In this manner, the biosensor design utilizes this interface as substrate for biomolecular binding, and its motion in an electric field as a signal transducer. We have shown that binding increases the electrical conductivity at the interface, which is transduced as a change in interfacial frequency response, and forms the basis for our presented interfacial electrokinetic transduction (IET) method. The system developed can detect low femtomolar avidin concentrations against a 5 mg/mL background of serum albumin, and can be reconfigured to detect other proteins. The IET sensor has the potential be extended to other biomolecular systems for the detection of disease biomarkers in serum and urine. Furthermore, because binding occurs dynamically in time over the length of the microchannel interface, it should be possible to use this IET approach to study the binding kinetics of a variety of specific ligand–receptor pairs. Finally, while fluorescent microscopy was used in this work to measure interface position, future work will focus on developing inexpensive methods for measuring interface displacement electrically, extending our IET approach to more complex samples such as whole blood and urine, reducing interfacial diffusion of the electric interface, and developing reactive trans- port models to study binding kinetics at the liquid interface.

Reprinted with permission from Biosensors and Bioelectronics[24], copyright 2015, Elsevier.

Chapter 8

Nanoparticle-based biosensing using interfacial electrokinetic transduction

In this chapter, we present a novel label-free electrokinetic method for detecting biomolecular binding on nanoparticles suspended in the vicinity of a laminar microfluidic interface. The sensor is based on the deflection of the liquid interface in an external AC electric field. Biomolecular binding on particles is shown to increase the interfacial electrical conductivity of the suspending electrolyte, which is sensitively transduced as a change in electrokinetic interfacial deflection. Using this approach, we detect the binding of biotin on streptavidin-functionalized nanoparticles at concentrations as low as 500 aM and perform detection of human IgG at clinically relevant concentrations (1.25–12 mg/mL) without labels. The interface response is only influenced by specific binding on nanoparticle binding sites and decreases when the particle concentration of reactive particles is reduced. Furthermore, we show that control experiments with both non-reactive particles and lack of a specific target analyte do not produce interfacial deflection. This work provides a promising method for quantifying bead-based binding kinetics for sensitive and specific biosensing in solution without labels.

8.1 Introduction

The ability to detect biomolecular targets at low concentrations without labels is an important requirement in areas including clinical diagnostics, drug discovery, environmental monitoring, and biomedical research. To be successful, biosensors typically require three basic components – a substrate for specific binding to occur, a transducer to translate the binding event into a detectable signal, and a detector to measure the transduced signal. Bead-based heterogeneous biosensors use nanoparticles with surface-immobilized receptors as a biosensing substrate for detecting a wide range of biomolecular analyte targets including proteins[3], DNA, and bacteria[4,5]. In comparison to traditional substrate-based microarray technology, the high surface-area-to-volume ratio of functionalized nanoparticles can lead to increased detection sensitivity and reduced assay time. Bead-based methods, for example, have been shown to increase the limit of detection (LOD) in SPR sensing[6], fluorimetric assays[7], and electrochemical amperic detection[8] and have been used in a broad range of colorimetric[5], enzymatic[9], mechanical[10], electrochemical[11] and fluorimetric[7] assays.

Nanoparticle-based biosensing is often accomplished using a heterogeneous support, where particles are adsorbed onto a solid surface[12] or a sol-gel matrix[13]. Nanoparticles functionalized with specific receptors are then flushed with a fluid or gas containing the relevant target analyte. Because colloids must be functionalized and assembled, current bead-based methods typically require multiple rinsing/drying steps[14,15], can suffer from functional group crowding[16] and surface fouling[17], and are usually designed for single use.

To reduce detection time and assay complexity, and to improve portability, biosensors can be integrated with microfluidics. With microfluidics, biomolecular binding can occur not only on functionalized solid surfaces, but also in solution phase at the interface formed between laminar liquid streams using low Reynolds number fluid flow. This sensing strategy is robust and has been successfully applied to detecting DNA hybridization[18] and for protein immunoassays[19]. Matthews et al, for example, reported a novel homogenous microfluidic biosensor using laminar aqueous interfaces as a biosensing substrate. Two co-flowing fluids – one containing a target analyte and a second with complimentary receptors – were forced to flow side-by-side along a main flow channel. Biomolecular binding occurred as target and receptor molecules diffused across the fluid interface formed between the two fluids. Using fluorescent microscopy, binding kinetics were quantified by measuring fluorescent intensity produced from bound product at varying distances down the microchannel length[155].

Laminar liquid interfaces can be created using “T-channel” or “Y-channel” microfluidic geometries[20,21]. The two fluids produce a quasi-stable liquid interface at their co-flowing contact region, where at low Reynolds number mass transport across the interface is driven strictly through diffusion[22]. Performing biosensing though diffusional mixing and biomolecular binding has several advantages over traditional heterogeneous biosensing at solid substrates. First, because biomolecular binding occurs in solution phase as opposed to a solid surface, diffusion-limited binding occurs over much shorter timescales. Second, the interfacial substrate is continually replenished and renewed at any given position in the microchannel and is therefore not subject to surface fouling and non-specific adsorption.

Despite the usefulness and advantages, current liquid interface-based microfluidic strategies require fluorescent labeling and fluorescent microscopy for signal transduction and detection[23]. Recently, Mavrogiannis et al. reported a novel label-free electrical detection strategy using an electrokinetic phenomena known as fluidic dielectrophoresis (fDEP). In fDEP, alternating current (AC) electric fields are used to polarize and electrically stress a liquid interface. The interface is an electrical interface, where one co-flowing fluid stream has a different electrical conductivity and dielectric constant than the adjacent stream. When an electric field is applied, charges accumulate and force the interface to deflect across a microfluidic channel. The magnitude and direction of this deflection is sensitive to the interfacial electrical properties[2]. Exploiting this phenomena, Mavrogiannis et al. demonstrated that interfacial biomolecular binding influences the liquid electrical conductivity and polarizability of the liquid interface, and that binding can be detected by quantifying the degree of interfacial deflection at varying positions down the microchannel[24]. In this way, binding is transduced as a change in the interfacial deflection of the fluid interface, which can be imaged and detected optically or electrically without labels.

Biomolecular detection using fDEP has been termed interfacial electrokinetic transduction (IET)[24]. In this method, the displacement of the interface is measured to detect biotin-streptavidin binding. This approach has been used to detect model avidin:biotin biomolecular binding at avidin concentrations as low as 50 femtomolar (fM), enabling it to compete with methods like surface plasmon resonance (SPR) (3 nm to 1.5 fM)[156] and enzyme-linked immunosorbent assays (ELISAs) (100 fM and below)[157], which are the current standard of clinical sensitivity.

In this work, we extend the usefulness of IET to that of nanoparticle bead-based assays and show that biomolecular binding on nanoscale particles can influence the deflection of a microfluidic liquid interface. More specifically, we investigate the ability to detect biomolecular binding on the surface of functionalized colloids subjected to specific biomolecular binding events suspended in solution in the vicinity of a liquid interface. The nanoparticles are functionalized with streptavidin molecules, which serve as specific binding receptors for biotin in solution. We demonstrate that specific binding on the nanoparticles produces a change in the electrical conductivity across the liquid interface, which is detected by IET. This colloid-based biosensing strategy does not use labels, amplified signaling, or methods for concentrating the analyte samples and is capable of detecting binding for biotin concentrations as low as 500 aM.

8.2. Material and Methods

8.2.1 Device Fabrication

In this section we describe the methods to fabricate the experimental devices and describe a theoretical basis for the biosensing measurements. The biosensing device used in this work requires a combination of microfluidic flow, electrokinetics, and colloid-based biomolecular surface chemistry. We utilize a microfluidic T-channel device to create a liquid interface through forcing fluid streams to flow side-by-side. One fluid phase contains a suspension of functionalized nanoparticles, while the other contains a specific target molecule.

To deliver an electric field across the interface, we integrate an array of microelectrodes within the main flow channel. The complete device, illustrated in Figure 8.1, is fabricated using a combination of microfluidic soft lithography and wet etching techniques. To fabricate the microarray of electrodes, we first coat glass cover slides (50x30 mm, no. 1, Fisher Scientific) with a 20 nm layer of chromium, followed by a 30 nm layer of gold, using electron beam deposition. Positive photoresist (S1813, Shipley) is spun onto the gold-coated slides and exposed using a UV contact aligner with a positive mask (Fineline Imaging) before etching the gold and chrome layers with chemical etchants (Alfa Aesar). The resulting electrodes are aligned symmetrically across the main flow channel axis, and spaced at 20 μm intervals, with pointed tips to focus the electric field at the liquid interface (Figure 8.1(b)). To fabricate the microchannel, we create a T-channel master mold by spin-coating negative photoresist (SU-8 3050, Microchem Corp.) on a 4-inch silicon wafer (Silicon Inc.) and exposing to a UV light source through a negative mask. The microfluidic channels are created by pouring PDMS, mixed in a 10:1 elastomer-to-curing-agent ratio, over the wafer mold and cured at 85 °C for 30 minutes. The cured polymer is peeled off and cut to size; fluid ports are created with a 0.75 mm biopsy punch (Ted Pella, Inc.). Finally, PDMS is bonded to the glass slide by exposure to oxygen plasma (Model 42A, Jetlight) for 1 minute, and immediately aligned and sealed by eye under an inverted microscope. The completed device consists of two inlet channels connected to a main microfluidic channel measuring 100 μm across and 35 μm high (Figure 8.1(b)).

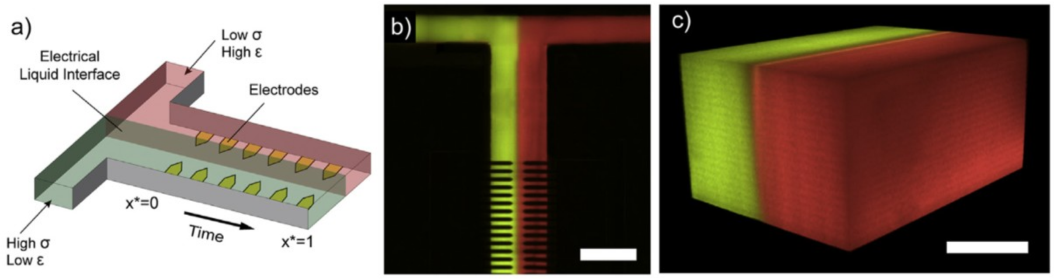

Figure 8.1. Microfluidic T-Channel. (a) Schematic of the microfluidic T-channel device with two co-flowing fluorescently labelled fluids. Scale bar 100 μm. (c) 3D confocal with integrated electrodes. (b) Top-down confocal micrograph of the T-channel device z-stack of the microfluidic-generated electrical liquid interface. Scale bar 50 μm.

8.2.2 Creating the Electrical Liquid Interface

Fluid flow is driven into the device using an external pressure source at a constant flow rate of 5 μL/min. To create the electrical properties necessary for fDEP, one fluid stream consists of a 10x diluted phosphate buffered saline (PBS) solution and the adjacent stream contains a 0.8 M solution of 6-aminohexanoic acid (AHA) (Sigma Aldrich). AHA is a water-soluble zwitterion intended to increase the dielectric constant of the aqueous solution[158]. To create a biosensing system at the liquid interface, we integrated a biomolecular recognition event between the two fluids, where one stream contained a suspension of functionalized nanoparticles, and the adjacent phase was used as a stream containing either the target analyte or a negative control. We used biotin and streptavidin-coated nanoparticles as a model biomolecular system to test our particle-based sensing strategy. Biotin (Sigma Aldrich) and 100 nm streptavidin-coated silica nanospheres (ζ = -34.6 mV) (Corpuscular Inc.) were used as the model bioreaction for this system; 100 nm carboxylated silica nanospheres (ζ = -34.3 mV) (Corpuscular Inc.) were used as a non-reactive negative control. A 4mM biotin stock solution was made in 0.8 M AHA and subsequently diluted to experimental concentrations ranging between 500 aM and 16 μM. The PBS stream contained the nanoparticle substrate: streptavidin-coated particles were triple washed and re-suspended in PBS solution and particle suspensions were maintained at 0.0375 wt% for all experiments unless specified otherwise. Human immunoglobulin G (IgG) (Sigma Aldrich) and 350 nm protein-A-coated silica nanospheres (Corpuscular Inc.) served as the physiologically relevant reaction scheme. Human IgG was dissolved in deionized water at a concentration of 5 mg/mL and diluted to experimental concentrations. Finally, the resulting fluid interface was imaged using confocal microscopy. The fluid stream containing AHA (with or without biotin) was fluorescently labeled “red” with 10 ng/mL Alexa Fluor 594 and the adjacent PBS stream (containing either streptavidin or carboxylated particles) was labeled “green” with 10 ng/mL Alexa Fluor 488 (Figure 8.1(c)).

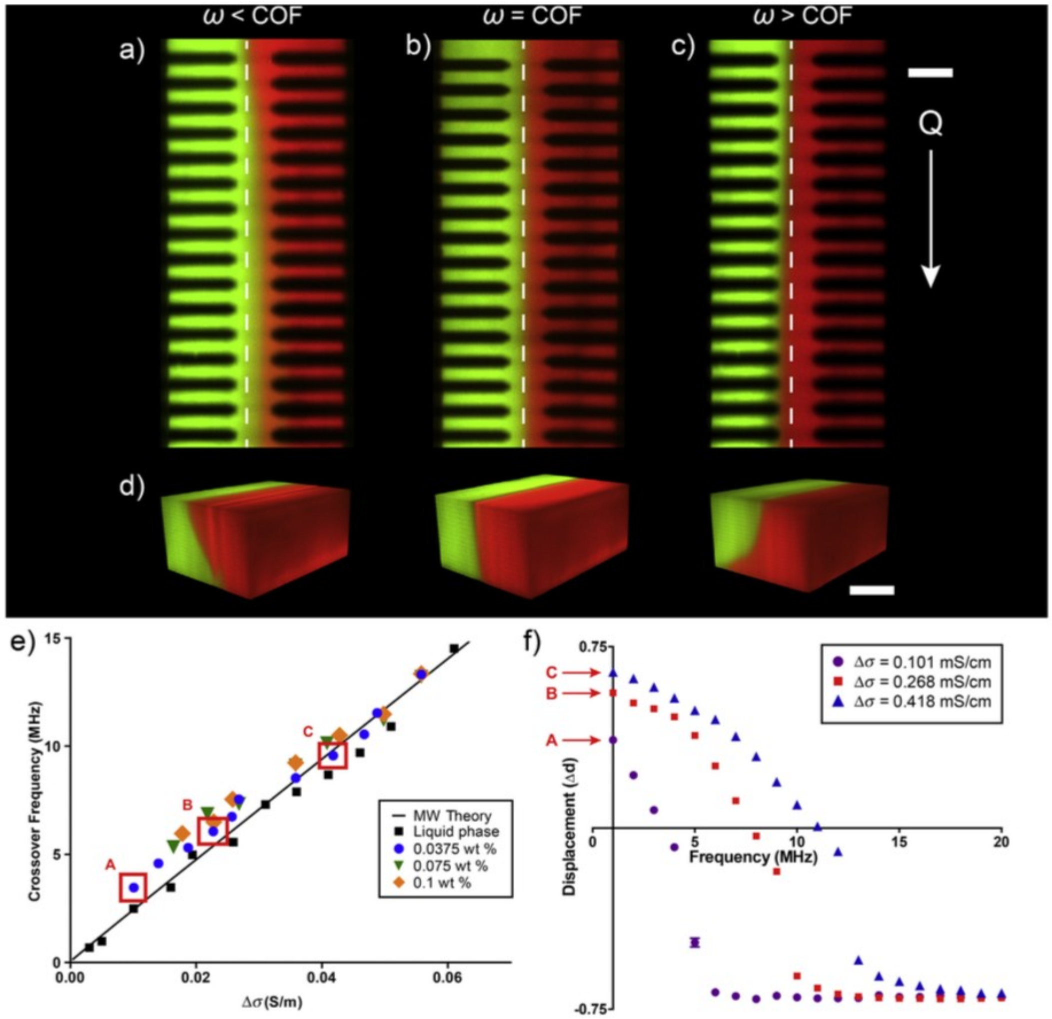

Figure 8.2. fDEP Crossover Frequency. (a) Top-down confocal images of the microfluidic channel, showing interfacial displacement for frequencies below the crossover, (b) at the crossover, (c) above the crossover. Scale bar 25 µm. (d) 3D confocal images showing the tilt of the electrical interface for frequencies below the crossover (left), at the crossover (center), and above the crossover (right). Scale bar 50 µm. (e) Crossover frequency plotted as a function of conductivity difference. The MW Theory line is plotted as Equation (3) for fixed values of $\varepsilon_1 = 78.2$ & $\varepsilon_2 = 110$. Lettered boxes are selected from the 0.0375 wt% data. (f) Displacement of the electrical interface as a function of applied frequency. Each complete dataset's COF is highlighted in a lettered box in (e).

8.2.3 Fluidic Dielectrophoresis

When each fluid phase is driven into the main microchannel, the resulting liquid interface has a steep gradient in the electrical properties between each fluid phase. The PBS stream has a high relative conductivity and a low permittivity (σ = 0.35 mS/cm, ε = 78.2), while the AHA stream has a low electrical conductivity but a high permittivity (σ = 32 μS/cm, ε = 110). When an AC electric field is applied across the interface at a potential of 10 volts peak-to-peak (V_{pp}), the electrical mismatch drives an electric field-driven charge accumulation at the fluid interface, which leads to an electrical stress and a physical electrohydrodynamic displacement of the fluid interface that is visually observable. This phenomenon is depicted at different AC electric frequencies in Figure 8.2(a)&(b). Because it takes a finite amount of time for the interface to polarize and displace from its original position, the sign and magnitude of the interfacial stress is sensitive to the AC frequency of the electric field. At low AC field frequency, for example, the high conductive PBS stream displaces into the less conductive AHA stream, as the field oscillates slowly enough for mobile ions in solution to electromigrate to the interface (Figures 2(a)&(b)). At higher frequency, however, polarization by ionic conduction does not have enough time to occur, and dielectric polarization dominates the interfacial charging. When this occurs, the direction of the displacement reverses, and the high-dielectric stream displaces across the channel into the low-dielectric stream (Figures 2(a)&(b)). Because we engineer the fluid interface such that one phase has a greater electrical conductivity and the other a greater dielectric constant, the direction and magnitude of the interfacial displacement is highly sensitive to the value of the AC frequency applied. We use this behavior as a means to assess whether biomolecular binding has occurred at the interface. This frequency dependence can be adequately described using Maxwell-Wager polarization mechanics and used to derive the frequency-dependent expression for the interfacial fDEP force[2], given by

$$\langle F_{DEP} \rangle = \langle \sigma_t E \rangle = 1/2Re[K(\omega)]\varepsilon_0 E_0^2. \tag{8.1}$$

The frequency at which the two charging mechanisms – conductive and dielectric – are balanced, (e.g. where $F_{DEP} = 0$) and no displacement occurs, is referred to as the crossover frequency (COF), which is sensitive to any electrical perturbations at the liquid interface (Figures 2(a)&(b)). If a biomolecular reaction occurs at the interface, for example, the COF will change if the reaction alters the electrical properties of the system; this modification becomes magnified as the reaction propagates downstream. As such, this electrical change over time can be reflected as a change in COF at varying axial positions within the main flow channel which can be equated to a different time step in the binding reaction. Therefore, we detect binding by inducing specific biomolecular reactions on functionalized nanoparticles suspended at the liquid interface, monitor the resulting liquid COF along the axial position down the length of the microchannel, and use the deviation from the original COF to determine the presence of a specific biomolecular binding event.

8.3 Results and Discussion

8.3.1 Maxwell-Wagner Polarization

In this work, we demonstrate that biomolecular binding on colloidal particles in suspension can influence the electrical polarization and motion of a surrounding laminar liquid interface. This polarization factor satisfies the charging mechanics described by classical Maxwell-Wagner polarization theory[151], and can be shown as

$$Re[K(\omega)] = \frac{((\varepsilon_2 - \varepsilon_1)\tau^2 \omega^2)}{((\varepsilon_2 + \varepsilon_1)(\tau^2 \omega^2 + 1))} + \frac{((\sigma_2 - \sigma_1)\tau^2 \omega^2)}{((\sigma_2 + \sigma_1)\tau^2 \omega^2 + 1)}. \tag{8.2}$$

Re[K(ω)] is the real (in phase) component of the Clausius–Mossotti factor which describes the degree to which the interface has polarized as a function of electric field frequency and $\tau = (\varepsilon_2 + \varepsilon_1)/(\sigma_2 + \sigma_1)$ is the charge relaxation timescale of the electrical liquid interface, which is related to the time required for mobile ions to electromigrate to the interface. The interfacial COF occurs when the net charge at the interface is zero, and is determined by setting Re[K(ω)] = 0,

$$\omega_{cof} = \frac{1}{2\pi}\left[\frac{(\sigma_1 - \sigma_2)(\sigma_1 + \sigma_2)}{(\varepsilon_2 - \varepsilon_1)(\varepsilon_2 + \varepsilon_1)}\right]^{1/2}. \tag{8.3}$$

Equation 8.3 can be used to determine the COF for the interface as a function of the fluid electrical properties. Plotted as a function of the fabricated electrical mismatch in properties (Figure 8.2(c)), we observe that there is a linear relationship between electrical conductivity difference across the fluid interface and the COF.

In this work, we utilize a dilute suspension of colloids instead of a pure electrolyte. In order to determine if the existing MW polarization theory is appropriate for the case of a dilute colloidal suspension, we first performed experiments to determine the interfacial COF as a function of electrolyte conductivity using a dilute colloidal suspension of 100 nm carboxylated silica particles in PBS buffer. The resulting COF data is plotted against our theoretical model (Equation 8.3) in Figure 8.2(c) for varying concentrations of colloid weight percent. The data show good agreement with the MW theory for both the pure liquid-liquid and liquid-colloid experiments. From Figure 8.2(c), we therefore assume that the colloidal suspensions used in this work are dilute enough to be mathematically and electrically approximated as a pure fluid, and that the presence of particles does not require additional modifications to our existing polarization model. We next measured the net displacement of the interface at different electric field frequencies and interfacial electrical conductivities. To accomplish this, we adjusted the conductivity of the colloidal suspension while keeping the weight percent and adjacent stream conductivity constant. In Figure

8.2(d) we plot the experimental displacement of three different interfacial conductivities. The varying interfacial conductivities are labeled a to c, and correspond to three COF data points in Figure 8.2(c) highlighted in boxes. The data demonstrates that at low frequency the magnitude of the interfacial displacement increases with increasing conductive difference across the two fluids. However, at high frequency the magnitude of the displacement is not affected by conductive differences, because this frequency range is only influenced by the dielectric differences between the two fluids.

Based on these COF and interfacial displacement results, we demonstrate how this interfacial motion can be used as a transducing element for our colloidal biosensor. To detect specific binding at the electrical interface, one fluid stream containing the target-probe is driven against an adjacent stream containing the analyte of interest. During binding on the nanoparticles, changes in the electrical properties at the interface due to this biorecognition event will lead to measurable changes in the interface COF.

8.3.2 Biotin-Streptavidin Binding

As mentioned previously, to determine if the electrical interface acts as a suitable substrate and transducer, a well-explored model reaction – biotin and streptavidin – was used. The biomolecular reaction between biotin and streptavidin is known to have a very small dissociation constant ($K_d \sim 10^{-15}$ M)[159], and therefore the reaction is rapid, nonreversible and serves as a good model system to demonstrate our biosensing strategy. It is advantageous to incorporate nanoparticles into the fDEP biosensor not only for their increased reactive surface area, but also for their diffusion-limiting properties. With a small diffusional coefficient (10^{-8} cm^2/s)[160], the streptavidin-coated silica provides a well-defined region of active binding sites at the liquid-liquid interface for biotin, a smaller, quickly-diffusing molecule, to rapidly diffuse towards the nanocolloidal interface and bind. We first supply biotin in excess (16 μM) to provide a constantly replenished source of analyte. We first measure the COF at the inlet, which we denote as COF_{in}, taking subsequent COF measurements down the electrode array. Upon binding, the biotin-streptavidin complex is observed to produce an increase in the interfacial COF. This is shown in Figure 8.3, where the COF increases down the axial length of the channel, corresponding to product propagation, before reaching a plateau, which we believe is indicative of binding saturation in the vicinity of the nanocolloidal-functionalized interface.

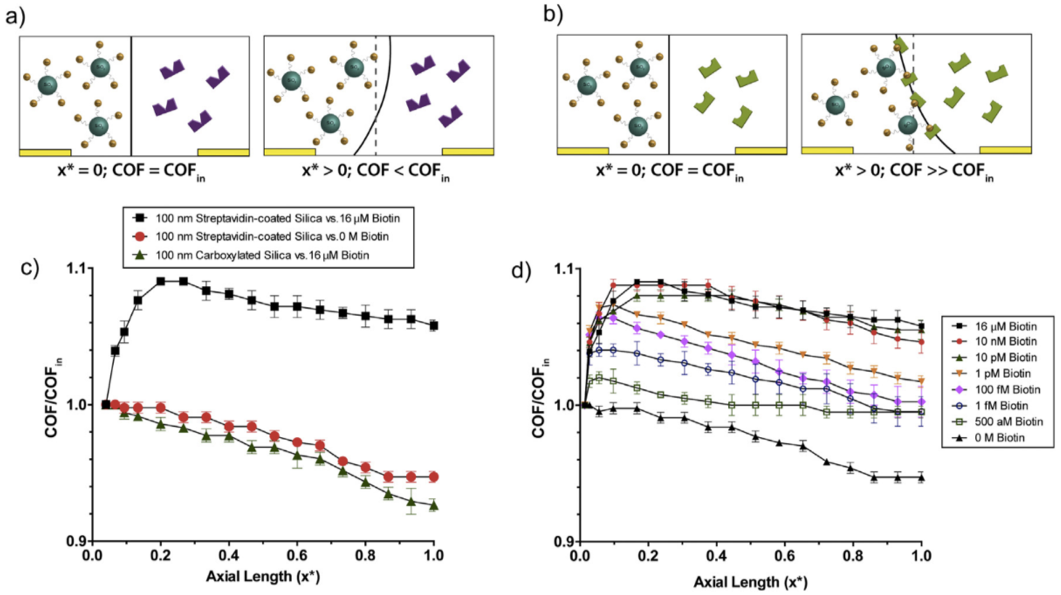

Figure 8.3. IET Bead-Based Biosensing Assay. (a) A schematic illustration of the case where no reaction is present. Down the length of the channel, the crossover decreases. (b) In the case of a biomolecular reaction, the crossover increases as the reaction propagates down the channel. (c) Detection sensorgram showing positive detection in the presence of a reaction, with decreasing control signals. (d) Limit of detection sensorgram showing the lowest biotin concentration detected with the colloid-assisted platform.

As one type of negative control, we performed the same experiment without biotin in the AHA stream. We observed that the COF does not increase, but rather it decreases over the axial channel length (Figure 8.3(a)). We attribute this decrease to diffusional blending downstream, which smoothens the interface and gradually reduces the initially sharp differences in electrical properties across the interface, leading to a reduced COF. As a second non-reactive negative control, we replaced the 100 nm streptavidin-coated silica nanospheres with carboxylated silica beads of the same size and tested the interface response against the same excess concentration of biotin (16 μM). The surface carboxyl groups (-COOH) are meant to emulate the nanocolloidal interface, while providing a non-reactive surface to observe any false positive signal from non-specific adsorption. Similar to the first negative control experiment, the COF decreased (Figure 8.3(a)).

8.3.3 Limit of Detection

To test the limit of detection for this biosensing strategy, the same experiments were performed over decreasing concentrations of biotin ranging between 16 μM and 500 aM (Figure 8.3(b)). Samples with several order-of-magnitude decreases in biotin concentration were used and introduced against streptavidin-coated beads. The biosensor response, as determined by the interface COF, was observed to increase with increasing concentrations of biotin (Figure 8.3). Using the 3-sigma method, we determined the experimental LOD for biotin to be 500 aM. Given the dimensions of the microfluidic device (100 μm main channel width x 35 μm channel height) and a total internal volume of 60 nL, this concentration translates to approximately 36 molecules of biotin in the device at any given time.

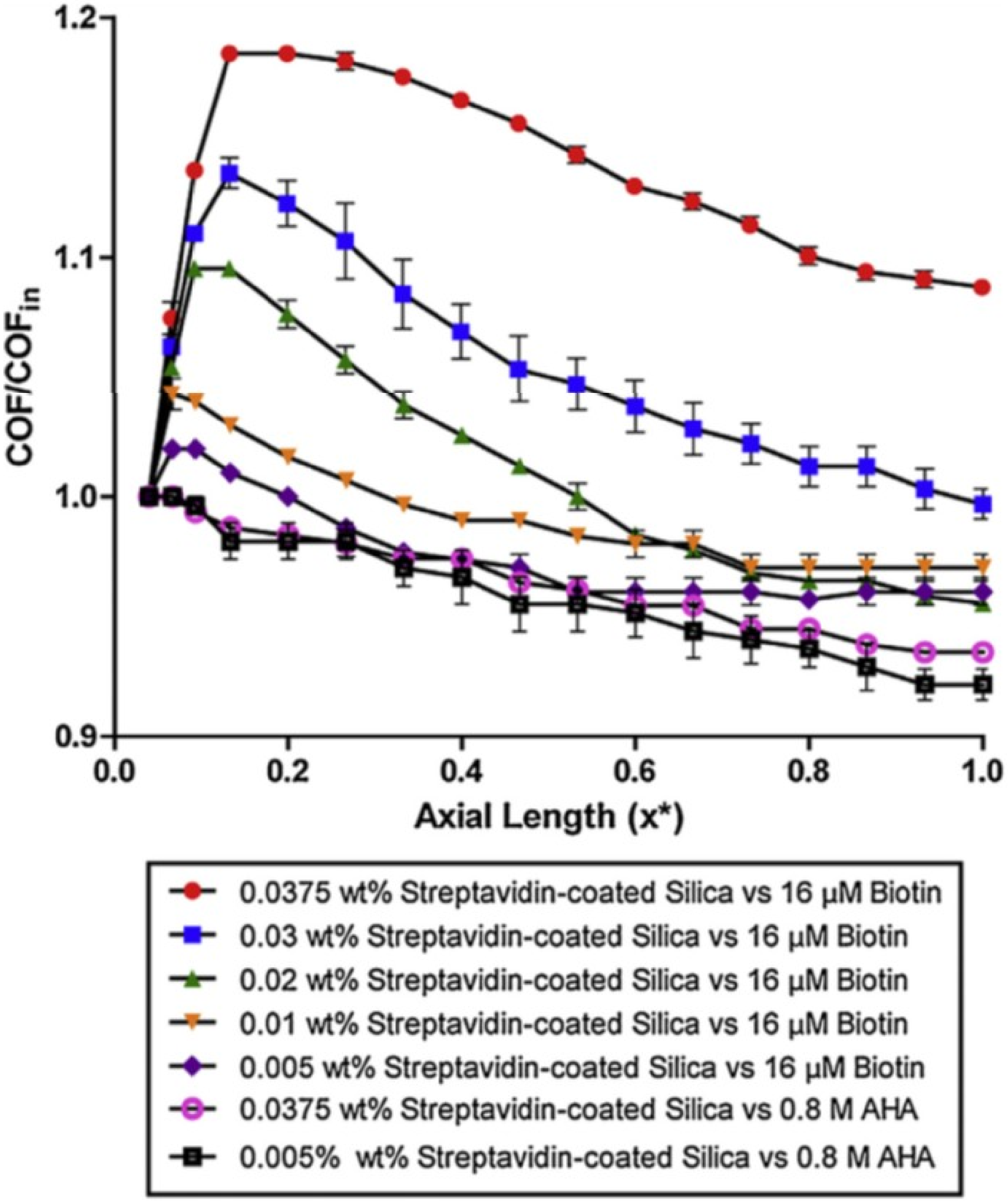

Figure 8.4. Streptavidin Limited Detection by Varying Particle wt%. Sensorgram illustrating the decrease in signal with decreasing weight percent of streptavidin-coated particles.

We perform another LOD experiment, this time limiting streptavidin. We find that by decreasing the weight percent of nanoparticles, and thus limiting the available streptavidin, we reduce the signal response (Figure 8.4). In this experiment, we have also decrease the conductivity of the highly conductive stream from 0.35 mS/cm to 0.24 mS/cm. The conductivity of this stream is still much greater than its neighbor, but the conductivity difference has been slightly reduced. It is interesting to note that by reducing the conductivity of the highly conductive stream, we increase the contribution of the reaction's response relative to the conductivity difference, and thus increase the magnitude of the signal response. The difference can be seen when comparing the saturated case from Figure 8.3, where the maximum signal response is 1.09, to the case in Figure 8.4, where the maximum response for the saturated case has increased to 1.19. We can conclude from this that decreasing the conductivity difference even further could bring the limit of detection down below its current 500 aM.

8.3.4 Background Protein

To test the robustness and selectivity of the biosensor, we then introduced a background of 5 mg/ml bovine serum albumin (BSA) to the biotin stream. We observed that the addition of BSA to the system dampens the COF signal, and while the COF of the 500 aM case does not increase significantly, it does not display the dramatic and immediate decrease in COF as the case of the BSA control but is still indicative of positive biotin detection (Figure 8.5).

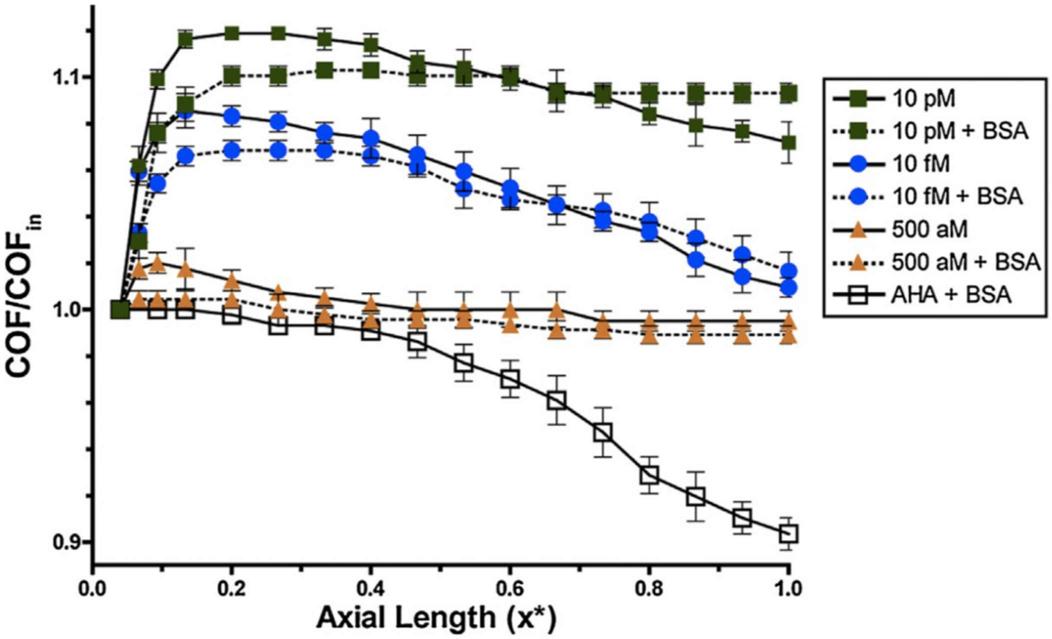

Figure 8.5. Biotin Detection in BSA Background. Sensorgram illustrating the ability of the fDEP biosensor to detect biotin-streptavidin binding in a background of 5 mg/mL BSA.

8.3.5 Human IgG-Protein A

In moving toward detection of physiologically relevant targets, we test the presence of human IgG in solution against 350 nm silica nanoparticles coated with protein A. The affinity of protein A binding to human IgG is reported to be on the order of $K_d \sim 10^{-10}$ M[161], five orders of magnitude weaker than biotin-streptavidin binding. In Figure 8.6, we find a positive response for concentrations down to 1.25 mg/mL, which is comparable to relevant concentrations in ELISA assays[162].

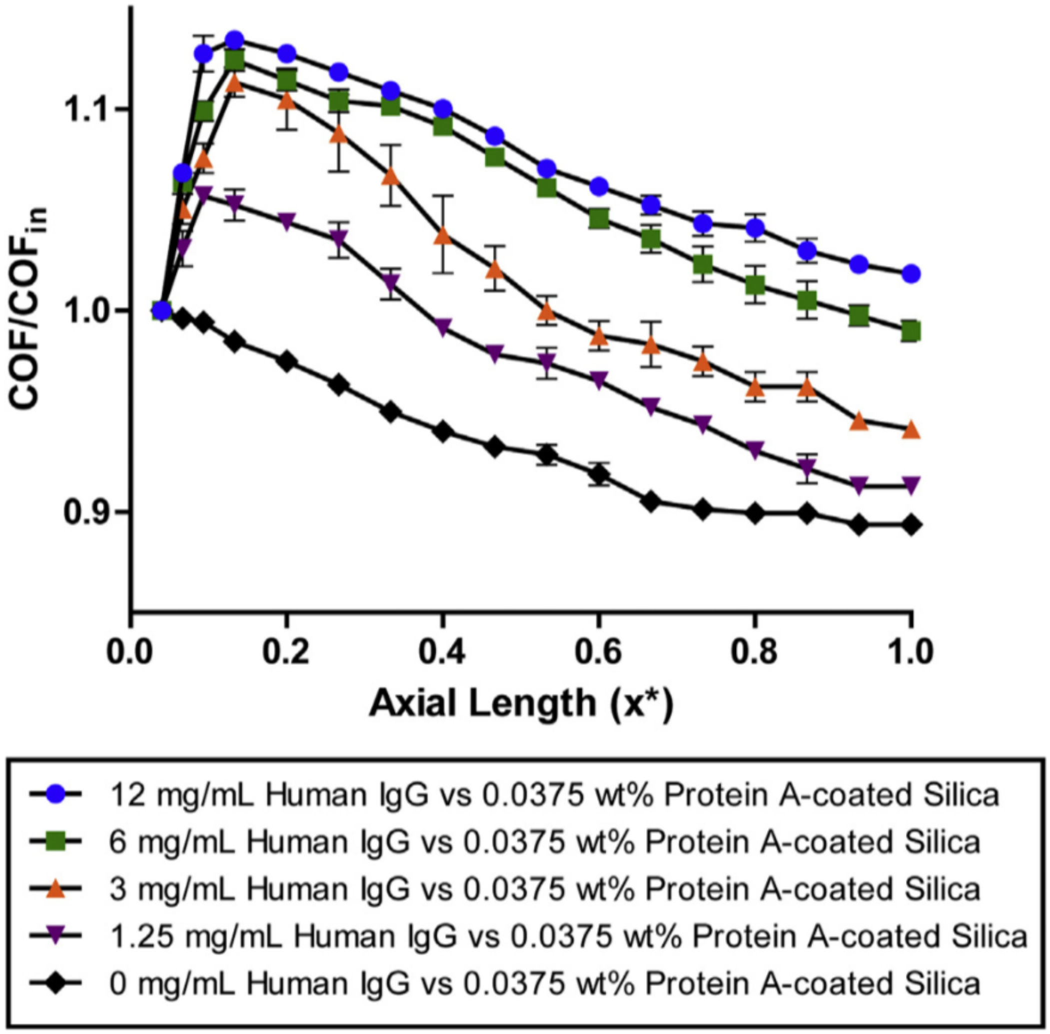

Figure 8.6. Detection of Human IgG-Protein A Binding. Detection sensorgram showing positive detection of human IgG with 350 nm silica nanoparticles coated with protein A.

We next performed a series of experiments to understand why biomolecular binding increases the interface COF. In previous work, Mavrogiannis et al. demonstrated that biomolecular binding in solution without particles produces a local increase in electrical conductivity difference across the liquid interface.[151] The authors demonstrated this by measuring the magnitude of the interfacial deflection for different analyte concentrations during binding and showed that increased analyte concentration only produced a measurable change in the interfacial displacement at low field frequency and motion at high frequency above the COF was not influenced by binding.

To determine what electrical properties were influence through binding, we measured the magnitude of interfacial deflection at varying voltage (1-20 Vpp) and frequencies both below (500 kHz) and above (40 MHz) the COF for systems with and without a nanoparticle-based biomolecular reaction. In the presence of a reaction, we observe that low frequency interfacial displacement is affected by binding, while there is no difference observed at high frequency above the COF (Figure 8.6). Based on these experiments, we believe that biotin binding on streptavidin nanoparticles increases the local electrical conductivity difference across the liquid interface. This is demonstrated in our deflection experiments as an increase in interfacial displacement at low frequency, and exploited as a biosensing transducer an increasing COF.

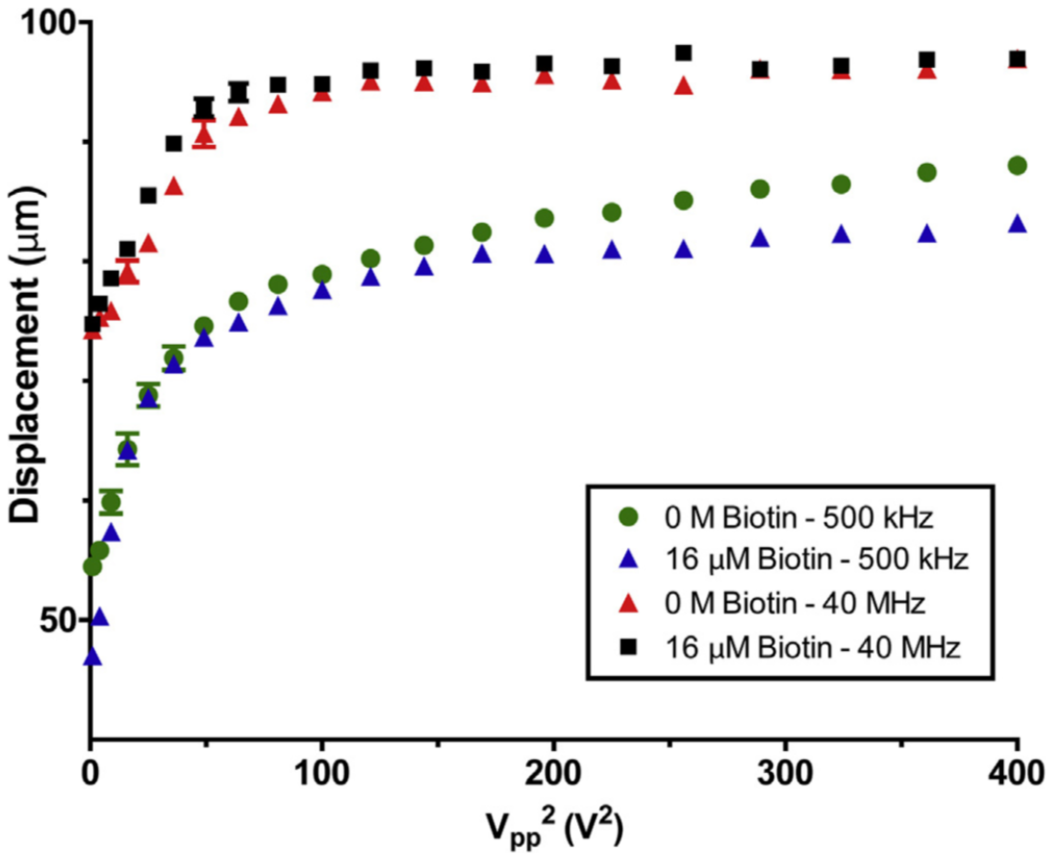

Figure 8.6. Influence of binding reaction on electrical properties measured by interface displacement. Displacement of the electrical interface versus applied voltage squared for both the low and high frequency case, in the case of a biomolecular reaction and a negative control. The divergence of the low frequency data suggests that the presence of a reaction alters the local conductivity at the electrical interface.

8.4 Conclusions

We have shown successful label-free detection of a biotin:streptavidin binding on nanoparticles using a colloid-based fDEP biosensor. We were able to effectively detect biotin-streptavidin binding at concentrations as low as 500 aM, and demonstrate experimentally that the presence of this specific biomolecular reaction drives a local increase in the electrical conductivity difference across the fluid interface. The addition of nanoparticles to the system increased the sensitivity by two orders of magnitude when compared to previous work conducted using only two liquid phases. The theoretical polarization model accurately predicts the experimental COF data, and demonstrates the ability to engineer a desired interfacial COF response by simple doping each fluid with specific differences in electrical conductivity and dielectric constant. Future experiments will involve developing this biosensing strategy into a system for testing analytes in physiologically relevant samples. Beads can very easily be functionalized with the relevant receptors to detect malaria, various cancers, and for other diagnostic exams that require femtomolar detection capabilities. The fDEP biosensor can also be used to monitor and study specific time points in a reaction at different points down the channel length, given the nature of the microfluidic flow device. Finally, future work will incorporate impedance spectroscopy to measure interfacial deflection where the fDEP biosensor becomes both label-free and non-optical. Removing this current limitation will allow this diagnostic device to become completely portable and inexpensive while still being highly sensitive and requiring very little sample volume, making it ideal for applications in point-of-care diagnostics and at-home testing.

Reprinted with permission from Sensors and Actuators B: Chemical[47], copyright 2016, Elsevier.

Chapter 9

Conclusions

In the introduction, we presented several problems requiring investigation, particularly in the realm of autologous blood doping. While this thesis does not represent or provide all the work and components required to fully realize the challenges addressed in the body of work, invaluable progress has been made toward our research goals.

In Chapter 4, we explored the possibility of dielectrophoresis (DEP) as an assay for implementation into the Athlete Biological Passport as a direct test for autologous blood doping. During the course of this project, we learned that storage volumes of blood sample aliquots plays a role in the overall red blood cell aging process. We can correct for this by taking larger (~1mL) blood samples, but will not investigate further into this phenomenon. We confirmed our assumption that *in vitro*, simulated reinfusions are not representative of the more complex nature of a real, *in vivo* reinfusions. We were surprised to find that while separation of the reinfused population grew increasingly difficult in the move from *in vitro* to *in vivo* transfusions, detection the transfusions actually became easier; our results reaffirm the need to investigate further into *in vivo* autologous transfusions.

In Chapter 5, we proposed a method to detect autologous transfusions with increased throughput. With increased throughput and larger sample sizes, sporting entities can achieve greater confidence in results without false positives. Unlike the DEP assay in Chapter 4, the RTDC assay was not hindered by the issue that arose with storing small whole blood volumes and was able to identify the reinfused subpopulation *in vitro*. Due to the glutaraldehyde-fixed condition of the blood doped samples received from our collaborators, the RTDC assay has not yet been used to detect *in vivo* autologous transfusions, which is the next step for this platform. After *in vivo* detection is established, implementation of the DEP and RTDC assays into the Athlete Biological Passport require only that these assays be automated and troubleshot.

In Chapter 8, we presented enhanced detection capabilities over Chapter 7, by the addition of a colloidal suspension functionalized with receptors for the analyte of interest. This bead-based biosensor is currently being utilized in the lab to run biologically relevant detection assays in unadulterated serum and whole blood samples. With the addition of impedance spectroscopy, also ongoing in the lab, this platform is making large steps toward becoming a sensitive, inexpensive, portable diagnostic tool for detection in droplet-scale samples of whole blood.

References

(1) Gagnon, Z. R. Cellular Dielectrophoresis: Applications to the Characterization, Manipulation, Separation and Patterning of Cells. *ELECTROPHORESIS* **2011**, *32* (18), 2466–2487.

(2) Mavrogiannis, N.; Desmond, M.; Gagnon, Z. R. Fluidic Dielectrophoresis: the Polarization and Displacement of Electrical Liquid Interfaces. *ELECTROPHORESIS* **2015**, *36* (13), 1386–1395.

(3) De, M.; Rana, S.; Akpinar, H.; Miranda, O. R.; Arvizo, R. R.; Bunz, U. H. F.; Rotello, V. M. Sensing of Proteins in Human Serum Using Conjugates of Nanoparticles and Green Fluorescent Protein. *Nature Chemistry* **2009**, *1* (6), 461–465.

(4) Lee, H.; Yoon, T. J.; Weissleder, R. Ultrasensitive Detection of Bacteria Using Core–Shell Nanoparticles and an NMR-Filter System. *Angewandte Chemie International Edition* **2009**, *48* (31), 5657–5660.

(5) Miranda, O. R.; Li, X.; Garcia-Gonzalez, L.; Zhu, Z.-J.; Yan, B.; Bunz, U. H. F.; Rotello, V. M. Colorimetric Bacteria Sensing Using a Supramolecular Enzyme–Nanoparticle Biosensor. *J. Am. Chem. Soc.* **2011**, *133* (25), 9650–9653.

(6) Jonathan C Riboh; Amanda J Haes; Adam D McFarland; Chanda Ranjit Yonzon, A.; Van Duyne, R. P. A Nanoscale Optical Biosensor: Real-Time Immunoassay in Physiological Buffer Enabled by Improved Nanoparticle Adhesion. *J. Phys. Chem. B* **2003**, *107* (8), 1772–1780.

(7) Wang, L.; Wang, L.; Wang, L.; Dong, L.; Bian, G.; Xia, T.; Chen, H. Direct Fluorimetric Determination of Γ-Globulin in Human Serum with Organic Nanoparticle Biosensor. *Spectrochimica Acta Part A: Molecular and Biomolecular Spectroscopy* **2005**, *61* (1-2), 129–133.

(8) Stern, E.; Klemic, J. F.; Routenberg, D. A.; Wyrembak, P. N.; Turner-Evans, D. B.; Hamilton, A. D.; LaVan, D. A.; Fahmy, T. M.; Reed, M. A. Label-Free Immunodetection with CMOS-Compatible Semiconducting Nanowires. *Nature* **2007**, *445* (7127), 519–522.

(9) Liu, T.; Zhao, J.; Zhang, D.; Li, G. Novel Method to Detect DNA Methylation Using Gold Nanoparticles Coupled with Enzyme-Linkage Reactions. *Anal. Chem.* **2009**, *82* (1), 229–233.

(10) Su, M.; Li, S.; Dravid, V. P. Microcantilever Resonance-Based DNA Detection with Nanoparticle Probes. *Appl. Phys. Lett.* **2003**, *82* (20), 3562–3564.
(11) Cai, H.; Wang, Y.; He, P.; Fang, Y. Electrochemical Detection of DNA Hybridization Based on Silver-Enhanced Gold Nanoparticle Label. *Analytica Chimica Acta* **2002**, *469* (2), 165–172.
(12) Goluch, E. D.; Nam, J.-M.; Georganopoulou, D. G.; Chiesl, T. N.; Shaikh, K. A.; Ryu, K. S.; Barron, A. E.; Mirkin, C. A.; Liu, C. A Bio-Barcode Assay for on-Chip Attomolar-Sensitivity Protein Detection. *Lab Chip* **2006**, *6* (10), 1293–1299.
(13) Jianbo Jia; Bingquan Wang; Aiguo Wu; Guangjin Cheng; Zhuang Li, A.; Dong, S. A Method to Construct a Third-Generation Horseradish Peroxidase Biosensor: Self-Assembling Gold Nanoparticles to Three-Dimensional Sol−Gel Network. *Anal. Chem.* **2002**, *74* (9), 2217–2223.
(14) Bunimovich, Y. L.; Shin, Y. S.; Yeo, W.-S.; Amori, M.; Kwong, G.; Heath, J. R. Quantitative Real-Time Measurements of DNA Hybridization with Alkylated Nonoxidized Silicon Nanowires in Electrolyte Solution. *J. Am. Chem. Soc.* **2006**, *128* (50), 16323–16331.
(15) Nicu, L.; Guirardel, M.; Chambosse, F.; Rougerie, P.; Hinh, S.; Trevisiol, E.; Francois, J.-M.; Majoral, J.-P.; Caminade, A.-M.; Cattan, E.; et al. Resonating Piezoelectric Membranes for Microelectromechanically Based Bioassay: Detection of Streptavidin–Gold Nanoparticles Interaction with Biotinylated DNA. *Sensors and Actuators B: Chemical* **2005**, *110* (1), 125–136.
(16) and, L. M. B.; Lisa A DeLouise. Steric Crowding Effects on Target Detection in an Affinity Biosensor. *Langmuir* **2007**, *23* (10), 5817–5823.
(17) Spisak, S.; Tulassay, Z.; Molnar, B.; Guttman, A. Protein Microchips in Biomedicine and Biomarker Discovery. *ELECTROPHORESIS* **2007**, *28* (23), 4261–4273.
(18) Kim, J. H.-S.; Marafie, A.; Jia, X.-Y.; Zoval, J. V.; Madou, M. J. Characterization of DNA Hybridization Kinetics in a Microfluidic Flow Channel. *Sensors and Actuators B: Chemical* **2006**, *113* (1), 281–289.
(19) Cesaro-Tadic, S.; Dernick, G.; Juncker, D.; Buurman, G.; Kropshofer, H.; Michel, B.; Fattinger, C.; Delamarche, E. High-Sensitivity Miniaturized Immunoassays for Tumor Necrosis Factor ? Using Microfluidic Systems. *Lab Chip* **2004**, *4* (6), 563–567.
(20) Mavrogiannis, N.; Ibo, M.; Fu, X.; Crivellari, F.; Gagnon, Z. Microfluidics Made Easy: a Robust Low-Cost Constant Pressure Flow Controller for Engineers and Cell Biologists. *Biomicrofluidics* **2016**, *10* (3), 034107.

(21) Morgan, H.; Green, N. G.; Ramos, A.; Garcia-Sanchez, P. Control of Two-Phase Flow in a Microfluidic System Using Ac Electric Fields. *Appl. Phys. Lett.* **2007**, *91* (25), 254107–4.

(22) Andrew Evan Kamholz; Bernhard H Weigl; Bruce A Finlayson, A.; Yager, P. Quantitative Analysis of Molecular Interaction in a Microfluidic Channel: the T-Sensor. *Anal. Chem.* **1999**, *71* (23), 5340–5347.

(23) Robinson, T.; Valluri, P.; Kennedy, G.; Sardini, A.; Dunsby, C.; Neil, M. A. A.; Baldwin, G. S.; French, P. M. W.; de Mello, A. J. Analysis of DNA Binding and Nucleotide Flipping Kinetics Using Two-Color Two-Photon Fluorescence Lifetime Imaging Microscopy. *Anal. Chem.* **2014**, *86* (21), 10732–10740.

(24) Mavrogiannis, N.; Crivellari, F.; Gagnon, Z. R. Label-Free Biomolecular Detection at Electrically Displaced Liquid Interfaces Using Interfacial Electrokinetic Transduction (IET). *Biosensors and Bioelectronics* **2016**, *77*, 790–798.

(25) O'Brien, P. G.; Puzzo, D. P.; Chutinan, A.; Bonifacio, L. D.; Ozin, G. A.; Kherani, N. P. Selectively Transparent and Conducting Photonic Crystals. *Adv. Mater.* **2010**, *22* (5), 611–616.

(26) Yokogawa, M. H. A. S. U. A. R. N. A. K. Postdeposition Annealing Influence on Sputtered Indium Tin Oxide Film Characteristics. *Jpn. J. Appl. Phys.* **1994**, *33* (1R), 302.

(27) World Anti-Doping Agency. Prohibited List. January 1, 2018, pp 1–10.

(28) Cazzola, M. A Global Strategy for Prevention and Detection of Blood Doping with Erythropoietin and Related Drugs. *Haematologica* **2000**, *85* (6), 561.

(29) Beiter, T.; Zimmermann, M.; Fragasso, A.; Armeanu, S.; Lauer, U. M.; Bitzer, M.; Su, H.; Young, W. L.; Niess, A. M.; Simon, P. Establishing a Novel Single-Copy Primer-Internal Intron-Spanning PCR (spiPCR) Procedure for the Direct Detection of Gene Doping. *Exerc Immunol Rev* **2008**, *14*, 73–85.

(30) Breidbach, A. Detection of Recombinant Human Erythropoietin in Urine by Isoelectric Focusing. *Clinical Chemistry* **2003**, *49* (6), 901–907.

(31) Thomas, A.; Kohler, M.; Walpurgis, K.; Schänzer, W.; Thevis, M. Proteolysis and Autolysis of Proteases and the Detection of Degradation Products in Doping Control. *Drug Testing and Analysis* **2009**, *1* (2), 81–86.

(32) Beiter, T.; Zimmermann, M.; Fragasso, A.; Hudemann, J.; Niess, A. M.; Bitzer, M.; Lauer, U. M.; Simon, P. Direct and Long-Term Detection of

Gene Doping in Conventional Blood Samples. *Gene Ther* **2010**, *18* (3), 225–231.

(33) Giraud, S.; Robinson, N.; Mangin, P.; Saugy, M. Scientific and Forensic Standards for Homologous Blood Transfusion Anti-Doping Analyses. *Forensic Science International* **2008**, *179* (1), 23–33.

(34) Nelson, M.; Popp, H.; Sharpe, K.; Ashenden, M. Proof of Homologous Blood Transfusion Through Quantification of Blood Group Antigens. *Haematologica* **2003**, *88* (11), 1284.

(35) Sottas, P.-E.; Robinson, N.; Giraud, S.; Taroni, F.; Kamber, M.; Mangin, P.; Saugy, M. Statistical Classification of Abnormal Blood Profiles in Athletes. *The International Journal of Biostatistics* **2006**, *2* (1).

(36) Sottas, P. E.; Robinson, N.; Rabin, O.; Saugy, M. The Athlete Biological Passport. *Clinical Chemistry* **2011**, *57* (7), 969–976.

(37) Sanchis-Gomar, F.; Martinez-Bello, V. E.; Carmen Gomez-Cabrera, M.; Vina, J. Current Limitations of the Athlete's Biological Passport Use in Sports. *Clinical Chemistry and Laboratory Medicine* **2011**, *49* (9), 1413–1415.

(38) Berezina, T. L.; Zaets, S. B.; Morgan, C.; Spillert, C. R.; Kamiyama, M.; Spolarics, Z.; Deitch, E. A.; Machiedo, G. W. Influence of Storage on Red Blood Cell Rheological Properties. *Journal of Surgical Research* **2002**, *102* (1), 6–12.

(39) Huang, Y.-X.; Wu, Z.-J.; Mehrishi, J.; Huang, B.-T.; Chen, X.-Y.; Zheng, X.-J.; Liu, W.-J.; Luo, M. Human Red Blood Cell Aging: Correlative Changes in Surface Charge and Cell Properties. *Journal of Cellular and Molecular Medicine* **2011**, *15* (12), 2634–2642.

(40) Bruce, L. J. The Involvement of Cation Leaks in the Storage Lesion of Red Blood Cells. **2014**, 1–12.

(41) Waugh, R. E.; Narla, M.; Jackson, C. W.; Mueller, T. J.; Suzuki, T.; Dale, G. L. Rheologic Properties of Senescent Erythrocytes: Loss of Surface Area and Volume with Red Blood Cell Age. *Blood* **1992**, *79* (5), 1351–1358.

(42) Antonelou, M. H.; Kriebardis, A. G.; Stamoulis, K. E.; Economou-Petersen, E.; Margaritis, L. H.; Papassideri, I. S. Red Blood Cell Aging Markers During Storage in Citrate-Phosphate-Dextrose-Saline-Adenine-Glucose-Mannitol. *Transfusion* **2010**, *50* (2), 376–389.

(43) Blasi, B.; D'Alessandro, A.; Ramundo, N.; Zolla, L. Red Blood Cell Storage and Cell Morphology. *Transfusion Medicine* **2012**, *22* (2), 90–96.

(44) Segura, J.; Lundby, C. Blood Doping: Potential of Blood and Urine Sampling to Detect Autologous Transfusion. *Br J Sports Med* **2014**, *48* (10), 837–841.

(45) Harrison, C. R.; Fang, J. C.-Y.; Walthall, K. J.; Green, C. C.; Porobic, V. Towards the Identification of Autologous Blood Transfusions Through Capillary Electrophoresis. *Anal Bioanal Chem* **2013**, *406* (3), 679–686.

(46) Gagnon, Z.; Mazur, J.; Chang, H.-C. Glutaraldehyde Enhanced Dielectrophoretic Yeast Cell Separation. *Biomicrofluidics* **2009**, *3* (4), 044108–044112.

(47) Crivellari, F.; Mavrogiannis, N.; Gagnon, Z. Nanoparticle-Based Biosensing Using Interfacial Electrokinetic Transduction. *Sensors and Actuators B: Chemical* **2017**, *240*, 926–933.

(48) Ibsen, S. D.; Wright, J.; Lewis, J. M.; Kim, S.; Ko, S.-Y.; Ong, J.; Manouchehri, S.; Vyas, A.; Akers, J.; Chen, C. C.; et al. Rapid Isolation and Detection of Exosomes and Associated Biomarkers From Plasma. *ACS Nano* **2017**, *11* (7), 6641–6651.

(49) Prakash, R.; Kaler, K. V. I. S. Liquid Dielectrophoresis Dispensing of Vesicles for on-Chip Nucleic Acid Isolation and Detection. *Colloids and Surfaces a-Physicochemical and Engineering Aspects* **2013**, *432*, 42–49.

(50) D'Amico, L.; Ajami, N. J.; Adachi, J. A.; Gascoyne, P. R. C.; Petrosino, J. F. Isolation and Concentration of Bacteria From Blood Using Microfluidic Membraneless Dialysis and Dielectrophoresis. *Lab Chip* **2017**, *17* (7), 1340–1348.

(51) Chou, W.-P.; Wang, H.-M.; Chang, J.-H.; Chiu, T.-K.; Hsieh, C.-H.; Liao, C.-J.; Wu, M.-H. The Utilization of Optically-Induced-Dielectrophoresis (ODEP)-Based Virtual Cell Filters in a Microfluidic System for Continuous Isolation and Purification of Circulating Tumour Cells (CTCs) Based on Their Size Characteristics. *Sensors and Actuators B: Chemical* **2017**, *241*, 245–254.

(52) Gascoyne, P. R. C.; Shim, S. Isolation of Circulating Tumor Cells by Dielectrophoresis. *Cancers (Basel)* **2014**, *6* (1), 545–579.

(53) Park, S.; Capelin, D.; Piriatinskiy, G.; Lotan, T.; Yossifon, G. Dielectrophoretic Characterization and Isolation of Jellyfish Stinging Capsules. *ELECTROPHORESIS* **2017**, *38* (16), 1996–2003.

(54) Gascoyne, P. R. C.; Vykoukal, J. Particle Separation by Dielectrophoresis. *ELECTROPHORESIS* **2002**, *23* (13), 1973–1983.

(55) Morgan, N. G. G. A. H. Dielectrophoretic Separation of Nano-Particles. *J. Phys. D: Appl. Phys.* **1997**, *30* (11), L41.

(56) Morgan, H.; Green, N. G. Dielectrophoretic Manipulation of Rod-Shaped Viral Particles. *Journal of Electrostatics* **1997**, *42* (3), 279–293.

(57) Wang, X.-B.; Yang, J.; Huang, Y.; Vykoukal, J.; Becker, F. F.; Gascoyne, P. R. C. Cell Separation by Dielectrophoretic Field-Flow-Fractionation. *Anal. Chem.* **2000**, *72* (4), 832–839.

(58) Hess, J. R. Red Cell Changes During Storage. *Transfus. Apher. Sci.* **2010**, *43* (1), 51–59.

(59) Gordon, J. E.; Gagnon, Z.; Chang, H.-C. Dielectrophoretic Discrimination of Bovine Red Blood Cell Starvation Age by Buffer Selection and Membrane Cross-Linking. *Biomicrofluidics* **2007**, *1* (4), 044102–044105.

(60) Gagnon, Z.; Gordon, J.; Sengupta, S.; Chang, H.-C. Bovine Red Blood Cell Starvation Age Discrimination Through a Glutaraldehyde-Amplified Dielectrophoretic Approach with Buffer Selection and Membrane Cross-Linking. *ELECTROPHORESIS* **2008**, *29* (11), 2272–2279.

(61) Unger, M. A.; Chou, H. P.; Thorsen, T.; Scherer, A.; Quake, S. R. Monolithic Microfabricated Valves and Pumps by Multilayer Soft Lithography. *Science* **2000**, *288* (5463), 113–116.

(62) Arnold, W. M. Positioning and Levitation Media for the Separation of Biological Cells. *IEEE Trans. on Ind. Applicat.* **2001**, *37* (5), 1468–1475.

(63) Irimajiri, A.; Hanai, T.; Inouye, A. A Dielectric Theory of “Multi-Stratified Shell” Model with Its Application to a Lymphoma Cell. *J. Theor. Biol.* **1979**, *78* (2), 251–269.

(64) Oblak, J.; Krizaj, D.; Amon, S.; Macek-Lebar, A.; Miklavcic, D. Feasibility Study for Cell Electroporation Detection and Separation by Means of Dielectrophoresis. *Bioelectrochemistry* **2007**, *71* (2), 164–171.

(65) Castellarnau, M.; Errachid, A.; Madrid, C.; Juárez, A.; Samitier, J. Dielectrophoresis as a Tool to Characterize and Differentiate Isogenic Mutants of Escherichia Coli. *Biophysical Journal* **2006**, *91* (10), 3937–3945.

(66) Fatoyinbo, H. O.; Hoettges, K. F.; Hughes, M. P. Rapid-on-Chip Determination of Dielectric Properties of Biological Cells Using Imaging Techniques in a Dielectrophoresis Dot Microsystem. *ELECTROPHORESIS* **2008**, *29* (1), 3–10.

(67) Hoettges, K. F.; Hübner, Y.; Broche, L. M.; Ogin, S. L.; Kass, G. E. N.; Hughes, M. P. Dielectrophoresis-Activated Multiwell Plate for Label-Free High-Throughput Drug Assessment. *Anal. Chem.* **2008**, *80* (6), 2063–2068.

(68) Broche, L. M.; Hoettges, K. F.; Ogin, S. L.; Kass, G. E. N.; Hughes, M. P. Rapid, Automated Measurement of Dielectrophoretic Forces Using DEP-Activated Microwells. *ELECTROPHORESIS* **2011**, *32* (17), 2393–2399.
(69) U.S. Anti-Doping Agency. Athlete Guide to the 2018 Prohibited List. *Athlete Guide to the 2018 Prohibited List*.
(70) International Olympic Committee. Anti-Doping Rules. February 14, 2018.
(71) Harmening, D. M. *Modern Blood Banking and Transfusion Practices*; 2012.
(72) Cohen, M. A.; Pierskalla, W. P. Target Inventory Levels for a Hospital Blood Bank or a Decentralized Regional Blood Banking System. *Transfusion* **1979**, *19* (4), 444–454.
(73) Spinella, P. C. Warm Fresh Whole Blood Transfusion for Severe Hemorrhage: U.S. Military and Potential Civilian Applications. *Critical Care Medicine* **2008**, *36* (7).
(74) Kauvar, D. S.; Holcomb, J. B.; Norris, G. C.; Hess, J. R. Fresh Whole Blood Transfusion: a Controversial Military Practice. *Journal of Trauma and Acute Care Surgery KW -* **2006**, *61* (1).
(75) Camp, F. R. J.; Shields, C. E. Military Blood Banking--Identification of the Group O Universal Donor for Transfusion of a, B and AB Recipients--an Enigma of Two Decades. *Mil Med* **1967**, *132* (6), 426–429.
(76) American Association of Blood Banks. AABB Technical Manual. Bethesda 2005.
(77) Valeri, C. R.; Pivacek, L. E.; Gray, A. D.; Cassidy, G. P.; Leavy, M. E.; Dennis, R. C.; Melaragno, A. J.; Niehoff, J.; Yeston, N.; Emerson, C. P.; et al. The Safety and Therapeutic Effectiveness of Human Red Cells Stored at — 80°C for as Long as 21 Years. *Transfusion* **1989**, *29* (5), 429–437.
(78) Valeri, C. R.; Srey, R.; Tilahun, D.; Ragno, G. The in Vitro Quality of Red Blood Cells Frozen with 40 Percent (Wt/Vol) Glycerol at −80°C for 14 Years, Deglycerolized with the Haemonetics ACP 215, and Stored at 4°C in Additive Solution-1 or Additive Solution-3 for Up to 3 Weeks. *Transfusion* **2004**, *44* (7), 990–995.
(79) Pottgiesser, T.; Specker, W.; Umhau, M.; Dickhuth, H.-H.; Roecker, K.; Schumacher, Y. O. Recovery of Hemoglobin Mass After Blood Donation. *Transfusion* **2008**, *48* (7), 1390–1397.
(80) Offner, P. J. Increased Rate of Infection Associated with Transfusion of Old Blood After Severe Injury. *Arch Surg* **2002**, *137* (6), 711–717.

(81) Purdy, F. R.; Tweeddale, M. G.; Merrick, P. M. Association of Mortality with Age of Blood Transfused in Septic ICU Patients. *Canadian Journal of Anaesthesia* **1997**, *44* (12), 1256–1261.

(82) Cregan, P.; Donegan, E.; Gotelli, G. Hemolytic Transfusion Reaction Following Transfusion of Frozen and Washed Autologous Red Cells. *Transfusion* **1991**, *31* (2), 172–175.

(83) Qi, J.; Zeng, J.; Zhao, F.; Lin, S. H.; Raja, B.; Strych, U.; Willson, R. C.; Shih, W.-C. Label-Free, in Situ SERS Monitoring of Individual DNA Hybridization in Microfluidics. *Nanoscale* **2014**, *6* (15), 8521–8526.

(84) Henry, O. Y. F.; O'Sullivan, C. K. Rapid DNA Hybridization in Microfluidics. *On-site and In-Vivo Special Issue* **2012**, *33*, 9–22.

(85) Zhao, L.; Ma, C.; Shen, S.; Tian, C.; Xu, J.; Tu, Q.; Li, T.; Wang, Y.; Wang, J. Pneumatic Microfluidics-Based Multiplex Single-Cell Array. *Biosensors and Bioelectronic* **2016**, *78*, 423–430.

(86) Yuan, X.; Couto, J. M.; Glidle, A.; Song, Y.; Sloan, W.; Yin, H. Single-Cell Microfluidics to Study the Effects of Genome Deletion on Bacterial Growth Behavior. *ACS Synth Biol* **2017**, *6* (12), 2219–2227.

(87) Zhu, Z.; Yang, C. J. Hydrogel Droplet Microfluidics for High-Throughput Single Molecule/Cell Analysis. *Accounts of Chemical Research* **2017**, *50* (1), 22–31.

(88) Lincoln, B.; Erickson, H. M.; Schinkinger, S.; Wottawah, F.; Mitchell, D.; Ulvick, S.; Bilby, C.; Guck, J. Deformability-Based Flow Cytometry. *Cytometry* **2004**, *59A* (2), 203–209.

(89) Otto, O.; Rosendahl, P.; Mietke, A.; Golfier, S.; Jacobi, A.; Toepfner, N.; Herold, C.; Klaue, D.; Fischer-Friedrich, E.; Guck, J. Real-Time Deformability Cytometry: High-Throughput Mechanical Phenotyping for Changes in Cell Function. *Biophysical Journal* **2015**, *108* (2), 140A–140A.

(90) Gossett, D. R.; Tse, H. T. K.; Lee, S. A.; Ying, Y.; Lindgren, A. G.; Yang, O. O.; Rao, J.; Clark, A. T.; Di Carlo, D. Hydrodynamic Stretching of Single Cells for Large Population Mechanical Phenotyping. *Proc. Natl. Acad. Sci. U.S.A.* **2012**, *109* (20), 7630–7635.

(91) Mietke, A.; Otto, O.; Girardo, S.; Rosendahl, P.; Taubenberger, A.; Golfier, S.; Ulbricht, E.; Aland, S.; Guck, J.; Fischer-Friedrich, E. Extracting Cell Stiffness From Real-Time Deformability Cytometry: Theory and Experiment. *Biophysical Journal* **2015**, *109* (10), 2023–2036.

(92) Shah, Y. T.; Kelkar, B. G.; Godbole, S. P.; Deckwer, W. D. Design Parameters Estimations for Bubble Column Reactors. *AIChE Journal* **1982**, *28* (3), 353–379.

(93) Pattison, R. N.; Swamy, J.; Mendenhall, B.; Hwang, C.; Frohlich, B. T. Measurement and Control of Dissolved Carbon Dioxide in Mammalian Cell Culture Processes Using an in Situ Fiber Optic Chemical Sensor. *Biotechnology Progress* **2000**, *16* (5), 769–774.

(94) Finn, R. K. Agitation-Aeration in the Laboratory and in Industry. *Bacteriological Reviews* **1954**, *18* (4), 254–274.

(95) Lewis, W. K.; Whitman, W. G. Principles of Gas Absorption. *Ind. Eng. Chem.* **1924**, *16* (12), 1215–1220.

(96) Whitman, W. G. The Two Film Theory of Gas Absorption. *International Journal of Heat and Mass Transfer* **1962**, *5* (5), 429–433.

(97) Garstecki, P.; Fuerstman, M. J.; Stone, H. A.; Whitesides, G. M. Formation of Droplets and Bubbles in a Microfluidic T-Junction-Scaling and Mechanism of Break-Up. *Lab Chip* **2006**, *6*, 437–446.

(98) Martinez, C. J. Bubble Generation in Microfluidic Devices. *Bubble Science, Engineering & Technology* **2009**, *1* (1-2), 40–52.

(99) Pirt, S. J. *Principles of Microbe and Cell Cultivation.*; Blackwell Scientific Publications.: Oxford, 1975.

(100) BISCHOFF, H. W. Some Soil Algae From Enchanted Rock and Related Algal Species. *Phycological studies* **1963**, 95.

(101) Murhammer, D. W.; Goochee, C. F. Scaleup of Insect Cell Cultures: Protective Effects of Pluronic F-68. *Nature Biotechnology* **1988**, *6* (12), 1411–1418.

(102) Zhang, Z.; Al-Rubeai, M.; Thomas, C. R. Effect of Pluronic F-68 on the Mechanical Properties of Mammalian Cells. *Enzyme and Microbial Technology* **1992**, *14* (12), 980–983.

(103) Prasad, K. Y.; Ramanujam, T. K. Gas Holdup and Overall Volumetric Mass Transfer Coefficient in a Modified Reversed Flow Jet Loop Reactor. *The Canadian Journal of Chemical Engineering* **1995**, *73* (2), 190–195.

(104) Ying, K.; Al-Mashhadani, M. K. H.; Hanotu, J. O.; Gilmour, D. J.; Zimmerman, W. B. Enhanced Mass Transfer in Microbubble Driven Airlift Bioreactor for Microalgal Culture. *Engineering* **2013**, *Vol.05No.09*, 9.

(105) Badino, A. C.; Facciotti, M. C. R.; Schmidell, W. Volumetric Oxygen Transfer Coefficients (kLa) in Batch Cultivations Involving Non-Newtonian Broths. *Biochemical Engineering Journal* **2001**, *8* (2), 111–119.

(106) Al-Ahmady, K. K. Analysis of Oxygen Transfer Performance on Sub-Surface Aeration Systems. *International Journal of Environmental Research and Public Health* **2006**, *3* (3), 301–308.

(107) Wabeke, R. L. Air Contaminants and Industrial Hygiene Ventilation: a Handbook of Practical Calculations, Problems, and Solutions. **1998**.

(108) Talbot, P.; Gortares, M. P.; Lencki, R. W.; la Noüe, de, J. Absorption of CO2 in Algal Mass Culture Systems: a Different Characterization Approach. *Biotechnology and Bioengineering* **1991**, *37* (9), 834–842.

(109) Lee, C.-G.; Palsson, B. Ø. High-Density Algal Photobioreactors Using Light-Emitting Diodes. *Biotechnology and Bioengineering* **1994**, *44* (10), 1161–1167.

(110) Richardson, J. W.; Johnson, M. D.; Outlaw, J. L. Economic Comparison of Open Pond Raceways to Photo Bio-Reactors for Profitable Production of Algae for Transportation Fuels in the Southwest. *Algal Research* **2012**, *1* (1), 93–100.

(111) Rogers, J. N.; Rosenberg, J. N.; Guzman, B. J.; Oh, V. H.; Mimbela, L. E.; Ghassemi, A.; Betenbaugh, M. J.; Oyler, G. A.; Donohue, M. D. A Critical Analysis of Paddlewheel-Driven Raceway Ponds for Algal Biofuel Production at Commercial Scales. *Algal Research* **2014**, *4*, 76–88.

(112) Du, L.; Prokop, A.; Tanner, R. D. Effect of Bubble Size on Foam Fractionation of Ovalbumin. In *Biotechnology for Fuels and Chemicals*; Humana Press, Totowa, NJ: Totowa, NJ, 2002; pp 1075–1091.

(113) Sayyaadi, H.; Nematollahi, M. Determination of Optimum Injection Flow Rate to Achieve Maximum Micro Bubble Drag Reduction in Ships; an Experimental Approach. *Scientia Iranica* **2013**, *20* (3), 535–541.

(114) Haribabu, K.; Sivasubramanian, V. *Determination of Mass Transfer Coefficient in an Inverse Fluidized Bed Reactor Using Statistical and Dynamic Method for a Non-Newtonian Fluid*; NISCAIR-CSIR, India, 2013.

(115) Sivasubramanian, V. Gas–Liquid Mass Transfer in Three-Phase Inverse Fluidized Bed Reactor with Newtonian and Non-Newtonian Fluids. *Asia-Pacific Journal of Chemical Engineering* **2010**, *5* (2), 361–368.

(116) Li, Q. Y.; Cui, Z. F.; Pepper, D. S. Effect of Bubble Size and Frequency on the Permeate Flux of Gas Sparged Ultrafiltration with Tubular Membranes. *Chemical Engineering Journal* **1997**, *67* (1), 71–75.

(117) Olowson, P. A.; Almstedt, A. E. Influence of Pressure and Fluidization Velocity on the Bubble Behaviour and Gas Flow Distribution in a Fluidized Bed. *Chemical Engineering Science* **1990**, *45* (7), 1733–1741.

(118) Hanotu, J.; Bandulasena, H. C. H.; Zimmerman, W. B. Microflotation Performance for Algal Separation. *Biotechnology and Bioengineering* **2012**, *109* (7), 1663–1673.

(119) Baker, J. J.; Crivellari, F.; Gagnon, Z.; Betenbaugh, M. J. Microfluidic Bubbler Facilitates Near Complete Mass Transfer for Sustainable Multiphase and Microbial Processing. *Biotechnology and Bioengineering* **2016**, *113* (9), 1924–1933.
(120) Peruski, A. H.; Johnson, L. H.; Peruski, L. F. Rapid and Sensitive Detection of Biological Warfare Agents Using Time-Resolved Fluorescence Assays. *J. Immunol. Methods* **2002**, *263* (1), 35–41.
(121) Peruski, A. H.; Peruski, L. F. Immunological Methods for Detection and Identification of Infectious Disease and Biological Warfare Agents. *Clin. Diagn. Lab. Immunol.* **2003**, *10* (4), 506–513.
(122) Palchetti, I.; Mascini, M. Nucleic Acid Biosensors for Environmental Pollution Monitoring. *Analyst* **2008**, *133*, 846–854.
(123) Rebe Raz, S.; Haasnoot, W. Multiplex Bioanalytical Methods for Food and Environmental Monitoring. *On-site and In-Vivo Special Issue* **2011**, *30* (9), 1526–1537.
(124) Cooper, M. A. Optical Biosensors in Drug Discovery. *Nat Rev Drug Discov* **2002**, *1* (7), 515–528.
(125) Myszka, D. G.; Rich, R. L. Implementing Surface Plasmon Resonance Biosensors in Drug Discovery. *Pharmaceutical Science & Technology Today* **2000**, *3* (9), 310–317.
(126) Lee, H.; Sun, E.; Ham, D.; Weissleder, R. Chip–NMR Biosensor for Detection and Molecular Analysis of Cells. *Nat Med* **2008**, *14* (8), 869–874.
(127) Roelse, M.; de Ruijter, N. C. A.; Vrouwe, E. X.; Jongsma, M. A. A Generic Microfluidic Biosensor of G Protein-Coupled Receptor Activation—Monitoring Cytoplasmic [Ca2+] Changes in Human HEK293 Cells. *Biosensors and Bioelectronic* **2013**, *47*, 436–444.
(128) Voura, E. B.; Jaiswal, J. K.; Mattoussi, H.; Simon, S. M. Tracking Metastatic Tumor Cell Extravasation with Quantum Dot Nanocrystals and Fluorescence Emission-Scanning Microscopy. *Nat Med* **2004**, *10* (9), 993–998.
(129) Wang, J. Electrochemical Biosensors: Towards Point-of-Care Cancer Diagnostics. *Biosensors and Bioelectronic* **2006**, *21* (10), 1887–1892.
(130) Wan, Y.; Su, Y.; Zhu, X.; Liu, G.; Fan, C. Development of Electrochemical Immunosensors Towards Point of Care Diagnostics. *Biosensors and Bioelectronic* **2013**, *47*, 1–11.
(131) Watkins, N. N.; Hassan, U.; Damhorst, G.; Ni, H.; Vaid, A.; Rodriguez, W.; Bashir, R. Microfluidic CD4+ and CD8+ T Lymphocyte Counters for Point-of-Care HIV Diagnostics Using Whole Blood. *Science Translational Medicine* **2013**, *5* (214), 214ra170–214ra170.

(132) Yoo, J.-C.; La, G.-S.; Kang, C. J.; Kim, Y.-S. Microfabricated Polydimethylsiloxane Microfluidic System Including Micropump and Microvalve for Integrated Biosensor. *Nano Korea 2006 Symposium* **2008**, *8* (6), 692–695.

(133) Lin, M. X.; Hyun, K.-A.; Moon, H.-S.; Sim, T. S.; Lee, J.-G.; Park, J. C.; Lee, S. S.; Jung, H.-I. Continuous Labeling of Circulating Tumor Cells with Microbeads Using a Vortex Micromixer for Highly Selective Isolation. *Biosensors and Bioelectronic* **2013**, *40* (1), 63–67.

(134) Kamholz, A. E.; Weigl, B. H.; Finlayson, B. A.; Yager, P. Quantitative Analysis of Molecular Interaction in a Microfluidic Channel: the T-Sensor. *Anal. Chem.* **1999**, *71* (23), 5340–5347.

(135) Ismagilov, R. F.; Stroock, A. D.; Kenis, P. J. A.; Whitesides, G.; Stone, H. A. Experimental and Theoretical Scaling Laws for Transverse Diffusive Broadening in Two-Phase Laminar Flows in Microchannels. *Appl. Phys. Lett.* **2000**, *76* (17), 2376–2378.

(136) Hatch, A.; Garcia, E.; Yager, P. Diffusion-Based Analysis of Molecular Interactions in Microfluidic Devices. *Proceedings of the IEEE* **2004**, *92* (1), 126–139.

(137) Atencia, J.; Beebe, D. J. Controlled Microfluidic Interfaces. *Nature* **2005**, *437* (7059), 648–655.

(138) Hatch, A.; Kamholz, A. E.; Hawkins, K. R.; Munson, M. S.; Schilling, E. A.; Weigl, B. H.; Yager, P. A Rapid Diffusion Immunoassay in a T-Sensor. *Nature Biotechnology* **2001**, *19* (5), 461–465.

(139) Pollet, J.; Delport, F.; Janssen, K. P. F.; Jans, K.; Maes, G.; Pfeiffer, H.; Wevers, M.; Lammertyn, J. Fiber Optic SPR Biosensing of DNA Hybridization and DNA–Protein Interactions. *Biosensors and Bioelectronic* **2009**, *25* (4), 864–869.

(140) Rodriguez, M. C.; Kawde, A.-N.; Wang, J. Aptamer Biosensor for Label-Free Impedance Spectroscopy Detection of Proteins Based on Recognition-Induced Switching of the Surface Charge. *Chem. Commun.* **2005**, 4267–4269.

(141) Coltro, W. K. T.; Neves, R. de S.; Motheo, A. de J.; da Silva, J. A. F.; Carrilho, E. Microfluidic Devices with Integrated Dual-Capacitively Coupled Contactless Conductivity Detection to Monitor Binding Events in Real Time. *Sensors and Actuators B: Chemical* **2014**, *192*, 239–246.

(142) Ariyaratne, A.; Zocchi, G. Plasmon Resonance Enhanced Mechanical Detection of Ligand Binding. *Appl. Phys. Lett.* **2015**, *106* (1), 013702.

(143) Cao, L.; Cheng, L.; Zhang, Z.; Wang, Y.; Zhang, X.; Chen, H.; Liu, B.; Zhang, S.; Kong, J. Visual and High-Throughput Detection of Cancer Cells Using a Graphene Oxide-Based FRET Aptasensing Microfluidic Chip. *Lab Chip* **2012**, *12* (22), 4864–4869.

(144) Dong, C.; Ren, J. Coupling of Fluorescence Correlation Spectroscopy with Capillary and Microchannel Analytical Systems and Its Applications. *ELECTROPHORESIS* **2014**, *35* (16), 2267–2278.

(145) Yoo, J. H.; Woo, D. H.; Chang, M.-S.; Chun, M.-S. Microfluidic Based Biosensing for Escherichia Coli Detection by Embedding Antimicrobial Peptide-Labeled Beads. *Sensors and Actuators B: Chemical* **2014**, *191*, 211–218.

(146) Giraud, G.; Schulze, H.; Li, D.-U.; Bachmann, T. T.; Crain, J.; Tyndall, D.; Richardson, J.; Walker, R.; Stoppa, D.; Charbon, E.; et al. Fluorescence Lifetime Biosensing with DNA Microarrays and a CMOS-SPAD Imager. *Biomed. Opt. Express* **2010**, *1* (5), 1302–1308.

(147) Gagnon, Z.; Mazur, J.; Chang, H.-C. Integrated AC Electrokinetic Cell Separation in a Closed-Loop Device. *Lab Chip* **2010**, *10*, 718–726.

(148) Gagnon, Z.; Senapati, S.; Chang, H.-C. Optimized DNA Hybridization Detection on Nanocolloidal Particles by Dielectrophoresis. *ELECTROPHORESIS* **2010**, *31* (4), 666–671.

(149) Lee, Y.-K.; Deval, J.; Tabeling, P.; Ho, C.-M. Chaotic Mixing in Electrokinetically and Pressure Driven Micro Flows. In *Microreaction Technology*; Springer, Berlin, Heidelberg: Berlin, Heidelberg, 2001; pp 185–191.

(150) Fu, X.; Mavrogiannis, N.; Doria, S.; Gagnon, Z. Microfluidic Pumping, Routing and Metering by Contactless Metal-Based Electro-Osmosis. *Lab Chip* **2015**, *15*, 3600–3608.

(151) Desmond, M.; Mavrogiannis, N.; Gagnon, Z. Maxwell-Wagner Polarization and Frequency-Dependent Injection at Aqueous Electrical Interfaces. *Phys. Rev. Lett.* **2012**, *109* (18), 187602.

(152) Pohl, H. A. The Motion and Precipitation of Suspensoids in Divergent Electric Fields. *Journal of Applied Physics* **1951**, *22* (7), 869–871.

(153) Avrameas, S. Amplification Systems in Immunoenzymatic Techniques. *J. Immunol. Methods* **1992**, *150* (1), 23–32.

(154) Kausaite, A.; van Dijk, M.; Castrop, J.; Ramanaviciene, A.; Baltrus, J. P.; Acaite, J.; Ramanavicius, A. Surface Plasmon Resonance Label-Free Monitoring of Antibody Antigen Interactions in Real Time. *Biochemistry and Molecular Biology Education* **2007**, *35* (1), 57–63.

(155) Sinéad M Matthews; Alan D Elder; Kamran Yunus; Clemens F Kaminski; Colin M Brennan, A.; Adrian C Fisher. Quantitative Kinetic Analysis in a Microfluidic Device Using Frequency-Domain Fluorescence Lifetime Imaging. *Anal. Chem.* **2007**, *79* (11), 4101–4109.

(156) Yao, X.; Li, X.; Toledo, F.; Zurita-Lopez, C.; Gutova, M.; Momand, J.; Zhou, F. Sub-Attomole Oligonucleotide and P53 cDNA Determinations via a High-Resolution Surface Plasmon Resonance Combined with

Oligonucleotide-Capped Gold Nanoparticle Signal Amplification. *Analytical Biochemistry* **2006**, *354* (2), 220–228.

(157) Rissin, D. M.; Kan, C. W.; Campbell, T. G.; Howes, S. C.; Fournier, D. R.; Song, L.; Piech, T.; Patel, P. P.; Chang, L.; Rivnak, A. J.; et al. Single-Molecule Enzyme-Linked Immunosorbent Assay Detects Serum Proteins at Subfemtomolar Concentrations. *Nature Biotechnology* **2010**, *28* (6), 595–599.

(158) Arnold, W. M.; Zimmermann, U. Dielectric Properties of Zwitterion Solutions. *Biochemical Society Transactions* **1993**, *21* (4), 475S–475S.

(159) Weber, P. C.; Ohlendorf, D. H.; Wendoloski, J. J.; Salemme, F. R. Structural Origins of High-Affinity Biotin Binding to Streptavidin. *Science* **1989**, *243* (4887), 85–88.

(160) Belongia, B. M.; Baygents, J. C. Measurements on the Diffusion Coefficient of Colloidal Particles by Taylor–Aris Dispersion. *Journal of Colloid and Interface Science* **1997**, *195* (1), 19–31.

(161) Akerström, B.; Björck, L. A Physicochemical Study of Protein G, a Molecule with Unique Immunoglobulin G-Binding Properties. *J. Biol. Chem.* **1986**, *261* (22), 10240–10247.

(162) Moen, K.; Brun, J. G.; Madland, T. M.; Tynning, T.; Jonsson, R. Immunoglobulin G and a Antibody Responses to Bacteroides Forsythus and Prevotella Intermedia in Sera and Synovial Fluids of Arthritis Patients. *Clin. Diagn. Lab. Immunol.* **2003**, *10* (6), 1043–1050.

Curriculum Vitae

Francesca Crivellari

Address: 3811 Canterbury Rd, Apt 1001 Baltimore, MD 21218
Phone: (757)560-5759
Email: fcriv@jhu.edu

Education

Ph.D. Johns Hopkins University **August 2012 – March 2018**
Chemical & Biomolecular Engineering – awarded *Whiting School of Engineering Dean's Fellowship*

B.S. Virginia Polytechnic Institute & State University (Virginia Tech)
Chemical Engineering **2008 – 2012**
Minor: Chemistry

Research Experience

Doctoral Research **2012 – 2018, Lab Captain**

- Detection of Autologous Blood Doping – World Anti-Doping Agency (WADA) & Partnership for Clean Competition
    - Utilizing microfabrication and electrokinetics – developed experimental setup and protocol to directly determine the presence of blood doping in endurance athletes.
- Working at the interface of microfluidics and electrokinetics. Engineering micro-scale fluidic systems with integrated micro-electrodes with an interdisciplinary approach. Utilized analytical skills and creative problem solving to break down large research goals, design requisite experiments, and appropriately interpret results.

Undergraduate Research **2009 – 2012**

- Decontamination of Chemical Warfare Agents – Defense Threat Reduction Agency (DTRA) **2010 – 2012**
  - Designed and implemented an ultra high vacuum testing chamber for uptake and reactivity studies on Army vehicle surfaces.
  - Paint surface analysis using SEM, FTIR, and XRD. Funded by Defense Threat Reduction Agency (DTRA)
- 3M adhesive polymer blending for breathable adhesive bandages. Blended polymers and performed mechanical strength tests on fabricated block copolymer films. **2009**

Select Publications

1. Crivellari, F., Mavrogiannis, N., Gagnon, Z. "Nanoparticle-based biosensing using interfacial electrokinetic transduction." Sensors and Actuators B: Chemical (2017).
2. Mavrogiannis, N., Ibo, M., Fu, X., Crivellari, F., Gagnon, Z. "Microfluidics made easy: A robust low-cost constant pressure flow controller for engineers and cell biologists." Biomicrofluidics (2016).
3. Mavrogiannis, N., Crivellari, F., Gagnon, Z. "Label-free biomolecular detection at electrically displaced liquid interfaces using interfacial electrokinetic transduction (IET)" Biosensors and Bioelectronics (2016).
4. Baker, J., Crivellari, F., Gagnon, Z., Betenbaugh, M. "Microfluidic bubbler facilitates near complete mass transfer for sustainable multiphase and microbial processing" Biotechnology and Bioengineering (2016).

Presentations

1. American Institute of Chemical Engineers Annual Meeting. San Francisco, CA – "Detecting Autologous Blood Transfusions Using Dielectrophoretic Spectroscopy" **Oral** **Nov 2016**
2. Dielectrophoresis Meeting. MIT, Cambridge, MA – "Label-Free Biosensing at Polarizable Liquid Interfaces Using Fluidic Dielectrophoresis." **Oral** **July 2016**
3. International Conference on Nanotechnology and Biosensors. Prague, Czech Republic – "Colloid-Based Attomolar Detection by Fluidic Dielectrophoresis." **Oral** **July 2015**

4. SciX Conference. Reno, NV – “Colloid-based Biodetection by Fluidic Dielectrophoresis.” **Oral** **Oct 2014**

Activities & Outreach

1. Teaching Assistant – Johns Hopkins University. Transport Phenomena II. Wrote homework and exam solutions in addition to teaching recitations and class lectures during professor absences. **Fall semesters 2016/2014/2013**
2. Undergraduate Student Mentor – Johns Hopkins University. **2014 – 2017**
3. Women in Science and Engineering (WISE) Mentor – Johns Hopkins University. **2014 – 2016**
4. Social Chair, Graduate Student Liaison Committee – Johns Hopkins University. Hosted and organized social events for the graduate ChemBE students to facilitate camaraderie within the department. **2013 – 2015**
5. Annual Science and Technology Academy Program – Benjamin Stoddert Middle School, Marlow Heights, MD. Led students through fundamental lectures and hands-on experiments **July 2013**
6. Resident Advisor – Virginia Tech. Hypatia Engineering Residental Learning Community. **2009 – 2012**